THE SENSITIVITY OF TWO BEAM TRANSMISSION ELECTRON MICROSCOPE IMAGES TO THE STRUCTURE OF SMALL CRYSTAL DEFECTS

BY

LAWRENCE JOSEPH SYKES

A DISSERTATION PRESENTED TO THE GRADUATE COUNCIL OF THE UNIVERSITY OF FLORIDA IN PARTIAL FULFILLMENT FOR THE REQUIREMENTS OF THE DEGREE OF DOCTOR OF PHILOSOPHY

UNIVERSITY OF FLORIDA

1981

ACKNOWLEDGEMENTS

The author is indebted to innumerable persons who gave him aid and support during his graduate education. First among these is his advisor Dr. John J. Hren who provided an environment in which the author's abilities could flourish and grow. In particular Dr. Hren made contact possible with many other scientists and these acquaintances greatly broadened the author's outlook. Recognition is also due to Dr. Brent Adams for his aid and advice.

The author benefited from his work at Oak Ridge National Laboratories and wishes to thank the entire staff of the Metals and Ceramics REMAG group at ORNL. Particular acknowledgements are due to C. G. McKamey, J. T. Houston and F. Scarboro for the extensive time and labor they devoted to the author's work.

The Professors of the Department of Materials Science at the University of Florida provided invaluable encouragement by their expressed opinions and regard for the author's abilities. The patience and support of his parents and family are also greatly appreciated.

Finally, the financial support of the Department of Energy (D.O.E. contract #EY-76-S-05-4311), and the SHaRE program of ORNL (D.O.E. contract #EY-76-C-05-003) is gratefully acknowledged.

TABLE OF CONTENTS

TABLE OF CONTENTS - continued.

Abstract of Dissertation Presented to the
Graduate Council of the University of Florida in
Partial Fulfillment of the Requirements for the
Degree of Doctor of Philosophy

THE SENSITIVITY OF TWO BEAM TRANSMISSION ELECTRON MICROSCOPE IMAGES TO THE STRUCTURE OF SMALL CRYSTAL DEFECTS

By

Lawrence Joseph Sykes

December, 1981

Chairman: John J. Hren
Major Department: Materials Science and Engineering

A computer study of the transmission electron microscope images of small defects has dissected the theory of these images into a few components which determine the main features of the image. The above or below background nature of an image induced by displaced atoms is viewed in terms of the wave interference responsible for diffraction. The shape of the image is shown to arise from the resolved displacements of the defect and a simple and intuitively manageable method is presented for predicting the image. These results and trends, as well as several others, are displayed in pictorial formats by the use of computer simulated images to reinforce and augment this theory.

Application of the theory to a study of radiation damage in aluminum alloys led to an investigation of the origin and sensitivity of a particular kind of image (referred to as a $|\bar{g}\cdot\bar{b}| = 0$ image). These images detected strains largely ignored previously and can detect minor structural variations of a defect, such as the segregation of solute to a dislocation loop. In experimental application, this image was the primary evidence identifying as θ' precipitates observed in a neutron irradiated, dilute Al-Cu alloy. Microscopy of precipitates known to be θ' confirms this identification and establishes unambiguously that the lattice parameters a_o and b_o of θ' are greater than those of aluminum. The strain created by θ' is expected to contribute to the improved void swelling resistance of this alloy.

CHAPTER I
INTRODUCTION

A persistent objective of materials science research is to relate the microscopic structure of a material to its macroscopic properties. The use of transmission electron microscopes (TEM) in materials science has therefore increased continuously since the early 1940's when these instruments first became commonly available. The TEM's high resolution and ability to view samples in three dimensions make it obviously well suited to detailed microstructural characterization. More recent developments of the electron microscope's ability to do quantitative compositional analysis on a microstructural level ($\sim$100 nm, by the use of STEM-EDX and EELS) have extended this usefulness. But the full potential of the TEM is not yet achieved; its theory and use are still developing.

The present research grew from the desire to apply TEM to the study of heterogeneous nucleation and precipitation of a second phase. Such studies are important because precipitates can have large effects on the properties of materials. By the very meaning of the word nucleus, theories of nucleation deal with materials at the atomic level. Although nucleation and precipitation processes can sometimes be followed by various indirect means such as x-ray techniques or resistivity measurements, it is more

natural and direct that the high resolution of TEM be called upon in such studies. Aside from the compositional measurements (which may or may not be possible, depending on the material, or the size and the volume fraction of the precipitates), the atomic structure and geometry of the precipitate is desired. Structure here means not only the atomic arrangement within the precipitate, but also the relationship of the precipitate and the matrix, the habit plane of a plate-like precipitate, a precipitate's coherence, and the compressive or tensile nature of the precipitate misfit. Other structural information which would be desirable in a study of heterogeneous nucleation is the exact atomic arrangement of a precipitate upon its heterogeneous nucleation site. This type of information is derived not from diffraction patterns or compositional measurements, but from the image. Unfortunately, the TEM image of a defect will often bear little resemblance to the structure of the defect, as Fig. 1 shows. Here straight dislocations appear as highly curved lines, a grain boundary images as a set of fringes, and precipitates and dislocation loops appear similar, both being images consisting of a black and white lobe. Clearly an understanding of the image formation process must be available to correctly interpret the images and identify the defects. The more detailed the information to be extracted from a TEM image, the greater and more exact is the understanding needed.

The images presented below are called two beam dynamical strain contrast images. In such images, the

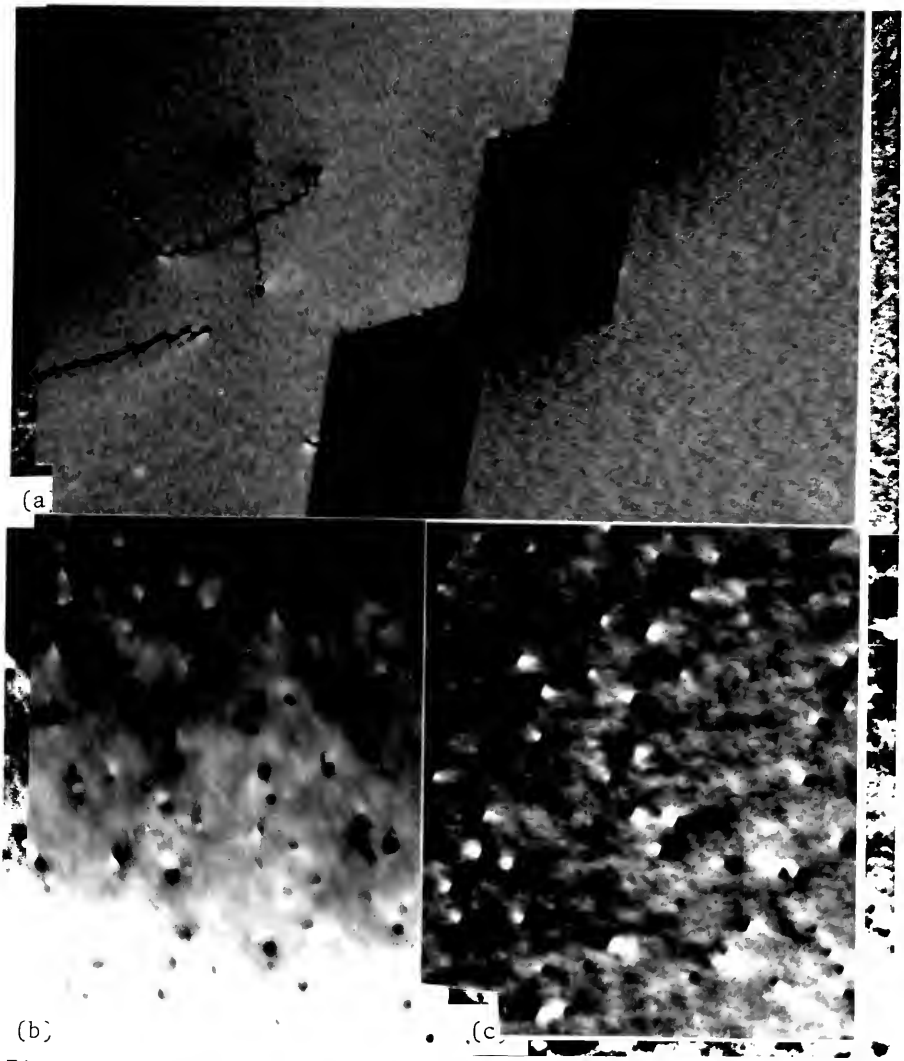

Fig. 1. Examples of TEM images: (a) dislocations and a grain boundary, (b) small dislocation loops, (c) small precipitates. Magnifications are (a) 40,000, (b) 200,000 and (c) 200,000.

electron beam is oriented so that it diffracts strongly off only one set of lattice planes and the contrast arises from the component of displacements perpendicular to these lattice planes. This imaging mode is the most common and is the easiest to achieve. The Howie-Whelan equations (1961) have proven to be an adequate description of two beam dynamical diffraction. These equations, along with relevant geometry and mathematical descriptions of defects, have been incorporated into a number of computer programs which produce simulated images of defects. Such simulated images accurately reproduce details of a real image. In principle then, the Howie-Whelan equations and the mathematical description of a defect are all that is necessary to understand defect images. The Howie-Whelan equations and the description of a defect are both sufficiently complex that an understanding of images is not easily derived from the equations, and so accurate computer calculations are needed. Use of these computer programs allows the various parameters to be studied, so that trends can be recognized and understood. In this way, the theory can be broken down into a number of effects depending on a few independent parameters. Combining these effects allows confident prediction of the major features of a defect image without recourse to computer calculations.

The objective of this research is to advance the understanding of small defect images and to prepare a method suitable to the practicing microscopist for identifying the most common small defect, the small dislocation loop. The

first point has had as its goal the study of precipitation phenomena. The second point has been derived from the desire to avoid the cumbersome methods of small loop identification presented in the literature. As can be appreciated from Fig. 1, the analysis of small defects is difficult because high magnification is needed to observe what little detail is available and because the images of distinctly different defects can be very similar. The method developed here uses direct image matching with simulated images and so involves minimum calculation and effort on the part of the microscopist.

Small dislocation loops occur in rapidly quenched materials where the supersaturated vacancies cluster and condense on a crystallographic plane. In irradiated materials, the collision of neutrons or other high energy particles with lattice atoms creates interstitial/vacancy pairs. This results in a supersaturation of both vacancies and interstitials which condense on lattice planes to form dislocation loops. A dislocation loop is characterized by the burgers vector of the dislocation, its habit plane and whether it consists of an extra plane of material (interstitial type) or a missing plane of material (vacancy type). Larger dislocation loops, resolvable as geometric loops, are fairly easy to characterize; the plane of the loop is determined by geometric reconstruction, the burgers vector is determined by the usual $|\bar{g}\cdot\bar{b}| = 0$ requirement for invisibility. As demonstrated in Fig. 1, the diameter of the loop is smaller than the extent of the image in the case

of a small loop and so the habit plane is obscured by the image. Nor are any of the other parameters describing a loop obvious in these images. The precipitates in Fig. 1 also look very much like the loops. Understanding these images allows identification of the various parameters of a loop and allows distinction between loops and precipitates.

A compromise is needed between using the computer to simulate every conceivable small defect and estimating the image from the known dependence of the image on relevant parameters. The solution chosen is the compilation of two image catalogs of the dislocation loop crystallographies expected of fcc and bcc materials. Catalogs were prepared only for cubic materials because of the great variety of defect types possible in other crystal systems. In these catalogs the images are calculated for a standard set of imaging parameters. These images produce the important topographical features of the image and the minor variations which would occur in the image for parameters, other than those used in the calculations, are easily visualized. By using several time-saving approximations it was possible to compute the large number of images in the catalogs (over 1,000). Some useful detail is lost from the image by the use of these approximations, but this shortcoming is compensated for by the capabilities of such a large data base. These can be summarized as follows:

1) Identification of an experimentally obtained image can be made by direct comparison with the catalogs.

2) The imaging conditions which are most useful and discriminating are also obvious, so the catalogs can be used to plan the experimental conditions to efficiently obtain useful data.

Furthermore, because of its pictorial form, the information in the catalogs can be understood and utilized by the practicing microscopist with a minimum of effort. The catalogs represent an essentially complete data base because the variations in imaging parameters can be accounted for easily.

Although the catalogs can be used without much understanding of the image formation, the importance of such knowledge should not be minimized. Details of the image can be crucial for the final identification of the image. Also, dislocation loops may serve as nucleation sites for precipitation. The segregation of solute atoms to loops and/or the transformation of the loop to a precipitate will make minor changes to the structure of the defect and subtly change the image. An understanding of the image allows deduction of the structure which causes the changes, and the computer can then be used to test this hypothesis. The computer studies which resulted from the compilation of the catalogs provided this understanding.

The use of the catalogs to study several neutron irradiated alloys led to the discovery of structure such as just indicated. Specifically, the addition of copper to aluminum is known to reduce the void swelling of aluminum in a nuclear reactor (Farrell and Houston, 1979). In the irradiated state an Al+100 ppma Cu alloy was observed to produce very small precipitates which had peculiar structure

in their images when imaged by the use of a diffracting vector perpendicular to the normal of these platelike precipitates (a condition referred as $|\bar{g}\cdot\bar{b}| = 0$). The nature of the structural difference between the precipitates and a small dislocation loop was quickly recognized and a number of models were hypothesized and tested. This testing produced a theoretical study of the sensitivity of these $|\bar{g}\cdot\bar{b}| = 0$ images to structural detail.

The results of this theoretical study are themselves significant, but in application to this alloy system two more results are obtained. First, by the good image match that the parameters of θ' give, considerable support is given to the hypothesis that the precipitates are θ'. This is very significant because there was not a sufficient volume fraction of precipitate to allow their detection or identification by other techniques, such as small angle x-ray scattering, electron diffraction or x-ray spectrographic techniques. The technique of analyzing the $|\bar{g}\cdot\bar{b}| = 0$ image finds application when the others have failed. Secondly, when considered in the light of work others have done on the diffusion of point defects and solute atoms in a stress field (e.g., Sines and Kikuchi, 1958), it appears that the same strain responsible for the $|\bar{g}\cdot\bar{b}| = 0$ images plays a role in the precipitates' interaction with point defects and the alloy's ability to resist void swelling.

CHAPTER II
REVIEW OF PREVIOUS WORK

Electron microscopes evolved from the components used to study the electron itself; Marton (1934) reported the use of the first electron microscope on biological specimens. The early intepretation of images of biological specimens was based on mass thickness scattering contrast (Marton and Schiff, 1941) but such interpretation yielded confusing results when applied to crystalline samples (Borries and Ruska, 1940). One of the electron microscope's greater contributions to materials science was the direct observation (and confirmation) of dislocations in metals (Bollmann, 1956; Hirsch et al., 1956). This application required correct and confident interpretation of the image contrast and catalysed the development of electron diffraction theories applied to image contrast.

Although Bethe (1928) first presented a dynamical theory of electron diffraction, a dynamical diffraction theory for image contrast was developed much later by Whelan and Hirsch (1957), who applied the theory to explain stacking fault images in fcc crystals. Theories for the images of dislocations soon followed as Hirsch et al. (1960) applied the kinematical theory. Later Howie and Whelan (1961) used the dynamical theory to explain these images. From this work came the so-called Howie-Whelan two beam

dynamical diffraction equations which describe the interaction of an electron wave with a crystal sample when only one set of lattice planes is strongly diffracting. They also developed the concept of the "column approximation" by which the intensity at a point on the electron exit surface of the sample is determined from the Howie-Whelan equations. The assumption is made that the electrons diffracting down a column of material do not interact with electrons in a neighboring column. The limitations of the Howie-Whelan two beam equations and the column approximation have been addressed (Howie and Basinski, 1968; Heidenreich, 1964; Head et al., 1973); in spite of the many simplifications the theory makes on reality, the Howie-Whelan equations have been successfully used in applications too numerous to list here.

The initial use of the Howie-Whelan equations to produce intensity traces for comparison to experimental densitometer traces of micrographs proved to be a laborious and unsatisfactory technique. A significant improvement was achieved by Head and co-workers (Head, 1967; Humble, 1968; Head et al., 1973), who incorporated the Howie-Whelan equations into a computer program which simulated micrographs of the entire image by converting calculated intensities to image points by the use of gray scale symbols. This program, however, lacked flexibility and generality because of its integration methods and geometric algorithms. Many computer programs have been developed to simulate the images of various small defects. The programs

of Rühle et al. (1965) and Bullough et al. (1971) simulated the images of small dislocations loops in isotropic materials. Programs for small loop images in anisotropic materials were developed by Ohr (1979) and Saldin et al. (1977). Saldin et al. (1977) also considered the images of small stacking fault tetrahedra. Sass et al. (1972) simulated cuboidal particles in a Ni-Ti alloy assuming isotropy. Degischer (1972) developed a computer program for the simulation of coherent particles in an anisotropic material.

All of these programs were specific and inflexible in purpose. Thölen (1970) developed a more general routine using the scattering matrix techique first suggested by Howie and Whelan (1961). This technique made the integration of the Howie-Whelan equations independent of the defect geometry and was therefore very flexible. It is well suited to high speed computations and is easily adapted to many beam images. Cooper (1977) incorporated this technique in a computer program capable of producing two beam images of isotropic dislocations, stacking faults and infinitesimal, isotropic, small defects. Various modifications of this program were used in the present work.

For the images of small defects, other approximations besides the Howie-Whelan equations can be used to estimate the image. Katerbau (1976) has used the Bloch wave approach to derive equations describing image contrast as a function of defect type, defect depth and foil thickness. He also implemented these equations in a simulation program. In

later work using the equations derived in the previous paper, Katerbau (1981) investigated the black-white direction of small defect images as a function of deviation from the Bragg condition. His goal was to determine experimental parameters which would discriminate between interstitial and vacancy type defects, but he concluded no such experimental conditions exist. Yoffe (1970) developed a method which extracted from the displacement field of a small defect the components which contribute to the image, and from this was able to construct isointensity contours of the image. This method employed the infinitesimal approximation and was applicable to anisotropic materials. This method was found to be in good agreement with the more accurate calculations of Ohr (1979). A similar approach was taken by Wilkens and Kirchner (1981), who estimated small defect images using the Fourier transform of the anisotropic elastic Greens function. They determined that the image of small dislocation loops became increasingly insensitive to the burgers vector and loop normal as the anisotropy of the crystal increased.

Two beam images are used in the greatest fraction of TEM applications but do not represent the total power of transmission electron microscopes. The many other abilities, techniques and theories of TEM are reviewed and described in several texts. Heidenreich (1964) covers the theory of electron diffraction and TEM image formation from the point of view of fundamental physics. Hirsch et al. (1977) discuss the theory and techniques of TEM as applied

to materials science. Edington (1975) has prepared an excellent and concise review of the many important applications and experimental results of TEM. Hren et al. (1979) have described and reviewed the recent advances of various analytical techniques such as compositional analysis by the use of x-ray and energy loss spectroscopy.

Interest in dislocation loops stemmed from their role in quenching experiments and radiation damage processes. The study of dislocation loops by TEM was impeded by the need for the proper interpretation of their images. Dislocation loops were first observed by Hirsch et al. (1958). Large loops can be identified by the so-called formal analysis used by Mazey et al. (1962) and Maher and Eyre (1968). A dislocation loop is described by two vectors, the burgers vector and the loop (habit plane) normal. In the case of large loops the normal can be determined by reconstructing the geometry from the data taken at various beam directions. The direction, but not the sign, of the burgers vector can be determined by imaging the loop with various diffraction vectors. If the burgers vector is perpendicular to the diffraction vectors ($|\bar{g}\cdot\bar{b}| = 0$) the defect will not appreciably distort the diffracting planes, and the image will be weak or invisible. Obtaining this condition for two diffracting vectors, $\bar{g}_1$ and $\bar{g}_2$, defines the burgers vector as $(\bar{g}_1)\times(\bar{g}_2)$. Knowledge of the loop normal and other crystallographic constraints can allow the burgers vector to be determined from one $|\bar{g}\cdot\bar{b}| = 0$ condition. The sign of the burgers vector depends on the

convention used and indicates whether the dislocation loop consists of an extra plane of atoms (interstitial loop) or a missing plane of atoms (vacancy loop). The determination of the interstitial or vacancy nature of a loop is achieved by exploiting the fact that for diffracting conditions deviating from the Bragg condition (i.e., $s \neq 0$), the position of the image does not coincide with the position of the dislocation core (Hirsch et al., 1960). The image will be either inside or outside a loop's true position, depending on the sign of $\bar{g}$, s and $\bar{b}$ as described by Edmondson and Williamson (1964). The magnitude of the burgers vector is usually determined a priori from crystallographic considerations.

The characterization of intermediate sized loops (10 nm to 100 nm) was considered by Maher and Eyre (1971) who extend the formal analysis described above. They also demonstrated the possibility of obtaining erroneous results from the method of Edmondson and Williamson (1964) for loops whose burgers vector is not parallel to their normal (sheared loops). For the case of prismatic loops in fcc materials ($\bar{n} = (111)$, $\bar{b} = a_o/2[110]$), Bell and Thomas (1966) have presented a method whereby the direction of the burgers vector can be determined without the use of the $|\bar{g}\cdot\bar{b}| = 0$ images. The method depends on the fact that the dislocation line changes character around the loop from pure edge to mixed screw and edge. The segments of mixed character give weaker contrast, resulting in a double arc image. The line of no contrast of these images is perpendicular to $\bar{b}$.

The early considerations of small defects were experimental TEM studies. Nicholson and Nutting (1958) studied a number of alloy systems containing small precipitates and GP zones. They first observed the black-white strain contrast images, typical of all small strain centers, for θ' in Al+4%Cu. Small defects appeared as black spots under most imaging conditions. The black-white contrast occurs near the exact Bragg condition when only one diffracting vector is operating (two beam case). Ashby and Brown (1963a) applied the dynamical theory to the images of spherical strain centers in Cu+2%Co. This work was extended to other small defects, including small loops (Ashby and Brown, 1963b). Their primary prediction concerned the direction from the black lobe of an image to the white lobe (the ℓ-vector). This vector was predicted to be parallel to the diffracting vector $\bar{g}$ (i.e., bright on the side of $+\bar{g}$) for the dark field image of vacancy type defects near the top or bottom surface of a foil. In their view, bright field images would be similar to dark field images for defects near the upper surface. The ℓ-vector for an interstitial type defect would be opposite that of a vacancy defect in all cases above.

The predictions of Ashby and Brown (1963b) were not consistent with the experimental work of Essmann and Wilkens (1964) who obtained inconsistent answers for the nature of small Frank loops in neutron irradiated copper. They also observed that the ℓ-vector was not parallel to $\bar{g}$ as in the case of spherical strain centers but was always parallel to

one of the [111] directions of the crystal. This led Rühle et al. (1965) to study the contrast of small loops as a function of loop size, foil thickness and depth of the loop within the foil. They showed that the contrast would reverse periodically as the defect moved away from either foil surface, and semi-quantitatively described this dependence. This divided the foil into a number of contrast layers, called L-layers, having a periodicity of one extinction distance (ξ_g). Their results were consistent with that of Ashby and Brown (1963b) for defects located in the contrast layers immediately adjacent to either foil surface. McIntyre and Brown (1966) demonstrated that the apparent inconsistency between these two results was due to the large defect misfit used in the work of Ashby and Brown (1963b). The existence of contrast oscillations complicated the determination of the interstitial or vacancy nature of a defect, because both ξ_g and the depth of the defect had to be known for such a determination. Diepers and Diehl (1967) and Diepers (1966) showed that stereomicroscopy could be successfully used for determining the defect depth.

Wilkens (1970) has published a review article on the electron microscopy of small defects. This article considered several types of defects, including both large and small dislocation loops, voids and stacking fault tetrahedra. The state of knowledge of small defect images was reviewed, concentrating on the oscillatory behavior of the ℓ-vector with depth. Determination of the size and shape of a defect was also covered. Wilkens included a

discussion of much of the experimental work done on irradiated materials.

Up to this time most work on the images of small dislocation loops had focused on pure edge loops. In irradiated copper the ℓ-vector proved to be always parallel or antiparallel to the projection of one of the [111] directions onto the image. It was therefore assumed that the ℓ-vector would always be parallel to the projection of the loop's burgers vector, and a method of defect analysis based on this trend was proposed (called ℓ-vector analysis, Rühle et al., 1965; Rühle, 1967). The topographic features of the image were not considered in great detail. In considering small sheared loops, minor changes in the image were expected and attention had to be paid to detail. Wilkens (1970) qualitatively predicted that the image of a sheared loop would be very little changed from that of a pure edge loop if the shear component of the burgers vector was the smaller component. Yoffe (1972) applied her approximate method to a pure shear loop to predict its image. She suggested that a shear component of the burgers vector would skew the images of loops viewed on edge. Wilkens and Rühle (1972) used a first order approximation to consider the images of small loops, including sheared loops. They demonstrated the skewing of images and from their equations predicted that an interchange of the loop normal $\bar{n}$ and the normalized burgers vector $\bar{b}$ would produce no change in the image. This latter result is not crystallographically meaningful, but does show that for

small loops, the loop normal is as important a parameter as the burgers vector. They concluded that &-analysis was not a sufficiently complete method for the identification of sheared loops and suggested such identification be done by comparison with calculated images.

Most of the preceding work used an approximate displacement field for the loops (the infinitesimal approximation, so-called because the solution is obtained by ignoring the spatial extent of the defect and considering it to exist at a point). Also, approximations were often used for intensity calculations and the results were displayed by means of isointensity contours rather than gray scale pictures. Bullough et al. (1971) developed a computer program incorporating the Howie-Whelan equations, an exact finite displacement calculation for pure edge loops presented by Bullough and Newman (1960) and gray scale display. They first applied this program to a study of intermediate sized loops in Mo. The effect of the deviation from the Bragg condition, the loop and foil orientation, the order and sign of $\bar{g}$, and the loop radius and depth in the foil were considered. They also demonstrated the program's ability to accurately reproduce the image of a small dislocation loop. Later work by Eyre et al. (1977a,b) considered the images of small edge loops in detail. They examined the details of the image with regard to the modulus $|\bar{g}\cdot\bar{b}|$ and proposed analysis based on this modulus. The two most important conditions are $|\bar{g}\cdot\bar{b}| > 1$, for which the black-white image of the loop displays an "interface

structure" (a reversal in contrast near the interface between the black and white lobe of the image), and $|\bar{g}\cdot\bar{b}| = 0$, for which a weak "butterfly" image occurs. They showed that the image was not invisible for defects located between contrast layers, but that the contrast would transition in a complex way as the defect's depth was varied from one L-layer to another. Using the finite displacement field for a shear loop presented by Ohr (1972), Holmes et al. (1979) and English et al. (1980) extend this work to include sheared loops. They found that the shear component of the burgers vector would not affect the interface structure in the case of $|\bar{g}\cdot\bar{b}| > 1$ but that considerable skewness could occur to the butterfly images in the case $|\bar{g}\cdot\bar{b}| = 0$. Distinction between these skewed images and some cases where $|\bar{g}\cdot\bar{b}| < 1$ was difficult. They also considered the possibility of extracting data about the loop normal from the interface between the black and white lobes. The paper of Holmes et al. (1979) presents many simulations (about 200) of bcc dislocation loops images with the beam directions [011] and [001], and so provides a very valuable data base to the literature.

Most of these investigators assumed an isotropic material because of the computing time required to calculate anisotropic displacements. Ohr (1976) evaluated displacements about an $a_o/2[111]$ Frank loop in copper and later used these results to simulate images (Ohr, 1979). As a result of anisotropy the black-white image streaked out along the projection of the [111] directions. Ohr therefore

favored the use of ℓ-analysis. Saldin et al. (1977) modeled dislocation loops and stacking fault tetrahedra by the superimposed displacement fields of angular dislocations in an anisotropic material. The approximate method of Yoffe (1970) is also applicable to ansiotropic materials.

The literature of small dislocation loop images presents three quantifications of image behavior. The first is the dependence of the black-white vector on foil thickness and defect depth. The others, ℓ-analysis and $|\bar{g}\cdot\bar{b}|$ analysis, predict the image topography. Both the later methods have extracted geometric trends from the image and expressed them in a mathematical form. Complications occur in both methods. For ℓ-analysis, skewing and deviations of the ℓ-vector arise due to anisotropy, shearing of the burgers vector and inclination of the foil. These same effects produce skewing in the $|\bar{g}\cdot\bar{b}| = 0$ butterfly images. The $|\bar{g}\cdot\bar{b}| > 1$ interface structure can be approached in the case of $|\bar{g}\cdot\bar{b}| < 1$ if the defect is between L-layers. Even with these complications aside, both methods require the microscopist to extract from his experimental images a quantity to be compared with rules originally derived from theoretical images.

The direct comparison of experimental and theoretical images is the easiest and least error-prone method of analysis. The ideal form of this approach, the comparison of theoretical images calculated for the exact experimental conditions, is not practical because of the difficulty of determining the experimental parameters. However,

comparison can be made to theoretical images calculated for a standard set of conditions chosen so that account can easily be made for deviations from these conditions. This philosophy led Cooper (1977) to compile a catalog of images for the loop crystallographies expected in fcc materials. The more exact calculations of Ohr (1979) and Eyre et al. (1977a,b) involved too much computing time and expense to allow the simulation of many images, and so Cooper employed an isotropic infinitesimal approximation for the displacement field. Studies were made of the effect of various parameters, such as deviation from the Bragg condition, the absorption parameters, defect depth, and the inclination of the foil, to allow logical selection of the standard conditions for image calculations. He then compiled a catalog of the unique permutations of loops of the type $a_o/3[111](111)$, $a_o/2[110](111)$, $a_o/2[110](110)$ and $a_o/2[110](120)$ for six major beam directions and using the low order diffracting vectors of those poles.

This catalog was made available to other microscopists by the work of Sykes et al. (1981) who extended the catalog to include bcc loops of the type $a_o/2[111](111)$, $a_o/2[110](110)$, $a_o/2[111](110)$ and $a_o[100](110)$. Cooper's format, which displayed on several pages the images of one beam direction, diffracting vector and defect type, was changed to a format of greater theoretical and experimental convenience. Coordinate transforms were supplied to extend the applicability of the catalogs. The theory of these images was laid out in simplified and largely pictorial

form. The theoretical and experimental uses of the catalogs were discussed and demonstrated. A highly modified version of Cooper's original program was listed with documentation to make it available to others.

It is seen that with time, simulation programs have improved and computing costs have decreased. As a result, methods of small defect analysis have moved away from quantified rules to direct comparison with images. The work of Holmes et al. (1979) proposes quantitative rules but nevertheless presents a great many images. The rules are given both to illustrate trends and to aid in the extrapolation of their limited data base. The infinitesimal approximation employed by Sykes et al. (1981) resulted in slightly less detail in the images of their catalogs, but this minor shortcoming is offset by the improved format and the completeness of the data base. These provided methods and abilities for experimental design and post-experimental defect identification not easily available from the results of Holmes et al. (1979). The works of Sykes et al. (1981) and of Holmes et al. (1979) developed concurrently along separate paths and are complementary rather than competing efforts.

CHAPTER III
THEORY OF TEM IMAGES OF SMALL DEFECTS

Because this work depends heavily on computer simulated images, this chapter begins with a brief explanation of how an image is simulated. Rather than consider a complex transmission electron image, the more intuitive case of light passing through a smoked glass sample will be presented as an analogy. Ignoring reflection and refraction and assuming perfectly collimated light, the image is essentially the shadow cast by the sample. To be calculated is the intensity of light at each position in the image. The calculation starts by defining a matrix of points in the image plane. From each point a ray is constructed antiparallel to the direction of travel of the light rays. The rays pierce the sample. The intensity of each ray is assigned the value of 1.0 before reaching the sample and, working toward the image point, the intensity is calculated as it attenuates through the sample. For light, the attenuation is assumed to be of the form

$$dI/dx = -\rho I$$

which leads to

$$I = I_o \exp(-\rho x)$$

For a sample in which the attenuation coefficient varies, the process

$$I_{n+1} = I_n \exp(-\rho(x)dx)$$

is repeated for each dx along the ray. The appropriate value of $\rho(x)$ is determined from the geometric description of the sample. A number of geometric algorithms and methods can be used. The sample may be defined, for example, as a slab of glass containing bubbles of various sizes as well as regions of darker (more absorbing) glass. In practice, defining the geometry is the most involved part of the program, but no complex theory is involved, so it will not be considered further here. Completing the above numerical integration for each image point produces the matrix of intensities desired. This matrix is converted to an image by having the computer print a corresponding matrix of symbols: a dark symbol such as "X" is used for low intensities, while a light symbol, such as ".", is used for high intensities.

Ignoring the crystallographic complications which occur in TEM image calculations, the simulation of an electron image is done as above. Instead of the simple absorption equation, the Howie-Whelan equations must be used to integrate intensities. In the Howie-Whelan equations the absorption term is usually assumed constant and the variable of position which affects the intensities is the displacement of atoms from their perfect crystal positions caused by a defect. The components necessary for electron image calculations are therefore the Howie-Whelan equations, the effect of displaced atoms on intensities and the calculation of displacements due to a defect.

For the purposes of imaging in the electron microscope, the particle nature of electrons can be largely ignored. Electron waves, like all waves, are capable of diffraction; that is, waves scattered by an array of scattering centers may constructively interfere in certain directions. The simplest theory of diffraction is the kinematic theory which assumes that the scattering of waves from each atom is so weak that the incident wave is negligibly attenuated by the diffraction process (so each atom receives the same incident intensity), and the diffracted wave is so weak that diffraction of it back into the incident beam can be ignored. The assumptions of the kinematic theory apply well to x-rays. Electrons, however, are so strongly scattered by atoms that after penetrating merely 10 to 20 nm into a crystal, the diffracted beam will be of an intensity equal to the incident beam. An accurate theory of electron diffraction must account for the attenuation of the incident wave, as well as diffraction of the scattered wave back into the incident wave.

Because diffraction is a phenomenon involving constructive and destructive interference of waves, account must be made of not merely the amplitude of a wave but also its phase. Upon entering a crystal, the incident electron wave scatters from each atom encountered. If the orientation of the crystal is appropriate for two beam diffraction, the scattered waves will constructively interfere in only one direction, and so begin to form the diffracted wave. A fact derived from more formal equations

presented later is that scattering occurs with a 90^{o} phase shift, and thus the diffracted wave is 90^{o} out of phase with the incident wave. This is represented in Fig. 2a. A convenient mathematical expression for waves is complex notation, and so Fig. 2 represents a wave as a vector in the complex plane. Electrons in the diffracted wave scatter with a probability equal to that of electrons in the incident wave, so a fraction of the electrons in the diffracted wave will scatter back in the direction of the incident wave. This scattering will also occur with a 90^{o} phase shift, so these electrons are $90^{o}+90^{o}$ out of phase with the incident wave and destructively interfere with it, Fig. 2b. It is easy to see that initially the incident wave will diffract (losing a small fraction of its amplitude in the process), and in so doing continually reinforces the diffracted wave. The contributions of the diffracted wave back into the incident wave will, on the other hand, continuously decrease the incident wave's amplitude until (in the ideal case) the situation in Fig. 2c occurs. At this point, the situation is similar to that at the entrant surface of the crystal, except that all the energy is in the diffracted wave. As the electrons proceed further into the crystal, the diffracted portion of the diffracted wave will constructively interfere with the incident wave, producing an incident wave $90^{o}+90^{o}$ out of phase with the original (but now lost) incident wave, Fig. 2d. Diffraction of this resurrected incident wave into the diffracted wave will destructively interfere with the diffracted wave, and so now

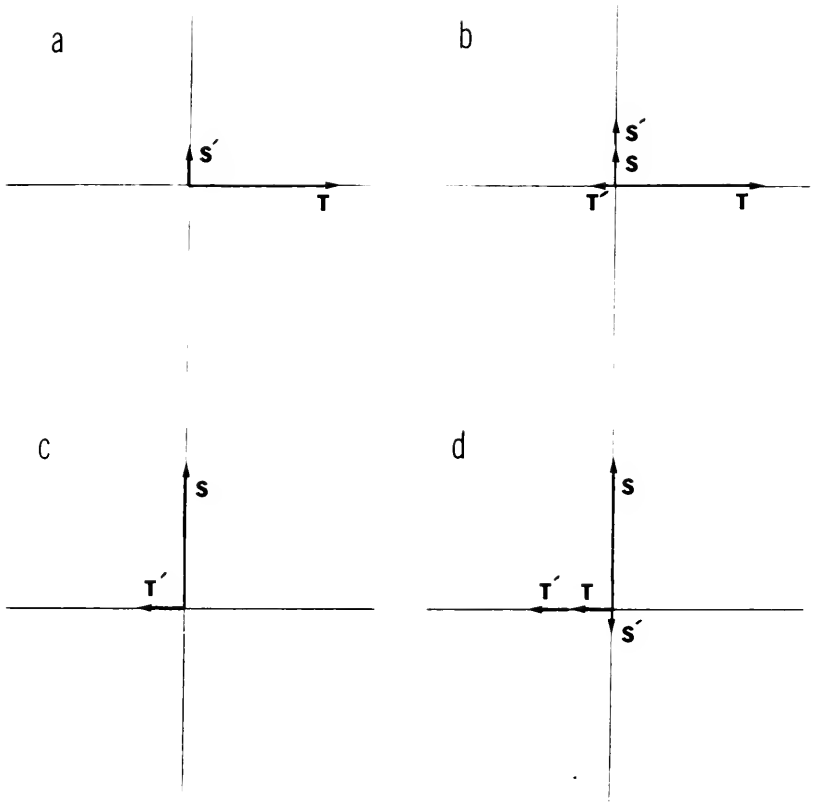

Fig. 2. Dynamical diffraction represented as vectors in the complex plane: (a) the beam just entering the sample, (b) the diffracted wave scattering back into the transmitted wave, (c) all intensity in the diffracted wave, (d) transmitted wave is resurrected, diffracted wave is decreasing. The primes indicate scattering from one wave into the complementary wave.

decrease, rather than increase, its amplitude. This process can continue ad infinitum to produce the seesaw exchange of energy shown in Fig. 3. The distance through which the incident beam must pass in order to go from maximum intensity, through minimum and back to maximum intensity is called an extinction distance and is referred to by the symbol ξ_g.

The above description assumes an ideal value of zero for three parameters which appear in the complete theory: normal absorption (η), anomalous absorption (A), and the deviation from the Bragg condition (s). Normal absorption accounts for the attenuation of the waves. The electrons are rarely physically absorbed by the crystal, but are often scattered out of either the incident or diffracted wave by an inelastic scattering event. The normal absorption reduces the waves in each ΔZ of crystal by the factor $\exp(-\pi\eta\Delta Z)$. If A and s are zero, a positive value of η will change the curves in Fig. 3 by simple dampening with depth. Anomalous absorption accounts for the possibility that an electron inelastically scattered out of one of the waves may be scattered back into either the incident or diffracted wave. These electrons are reintroduced with a random phase relationship, which on the average can be taken to be 90°. The effect is to counteract normal absorption and set a minimum intensity toward which the two waves will tend. Anomalous absorption is entered into the Howie-Whelan equations in an ad hoc manner. Its effects are the most

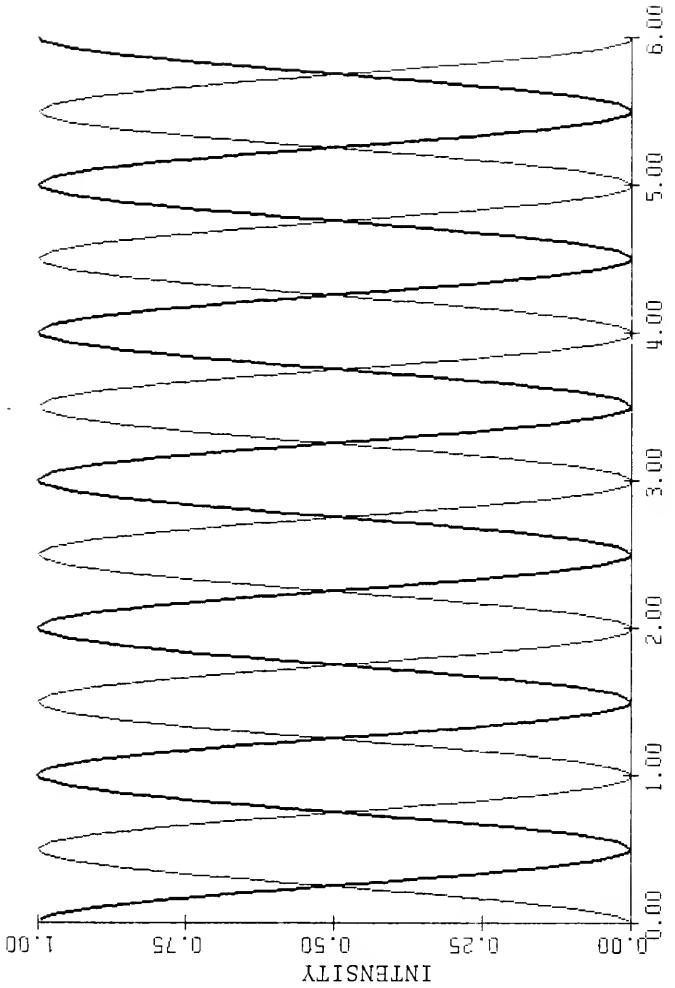

Fig. 3. Transmitted (heavy curve) and diffracted intensities for dynamical diffraction without normal or anomalous absorption.

difficult to understand. This is unfortunate because it can greatly influence image behavior.

In order to define the deviation parameter, s, the reciprocal space construction for two beam diffraction is shown in Fig. 4. The vector $\bar{s}$ joins the diffracting node $\bar{g}$ with the diffracting wave vector $\bar{K}'$. At the exact Bragg condition, the Ewald sphere touches the node $\bar{g}$ and $|\bar{s}|$ is zero. When the Ewald sphere does not touch the node the deviation parameter s has magnitude $|\bar{s}|$ and is considered positive if the node lies outside the Ewald sphere. The result of being off the Bragg condition is that constructive interference of the waves scattered in the direction $\bar{K}'$ is not complete. In the kinematic theory, this causes the intensity of the diffracted wave to vary as a $\sin^2$ function of depth. As seen, this already happens even at the Bragg condition for dynamical diffraction. The effect of $s \neq 0$ for dynamical diffraction is to increase this tendency and so lessen the distance required for the energy to be exchanged from one wave to the other; that is, it lessens the effective extinction distance.

The most exact and formal treatment of electron diffraction is the Bloch wave approach, in which the solution to Schroedinger's equation is found assuming the periodic potential of the crystal lattice (Kestenbech, 1971). The formalism of this approach allows account to be taken of diffraction into any number of directions. If the Bloch wave approach is carried out assuming that only one diffracted beam results, equations are obtained which give

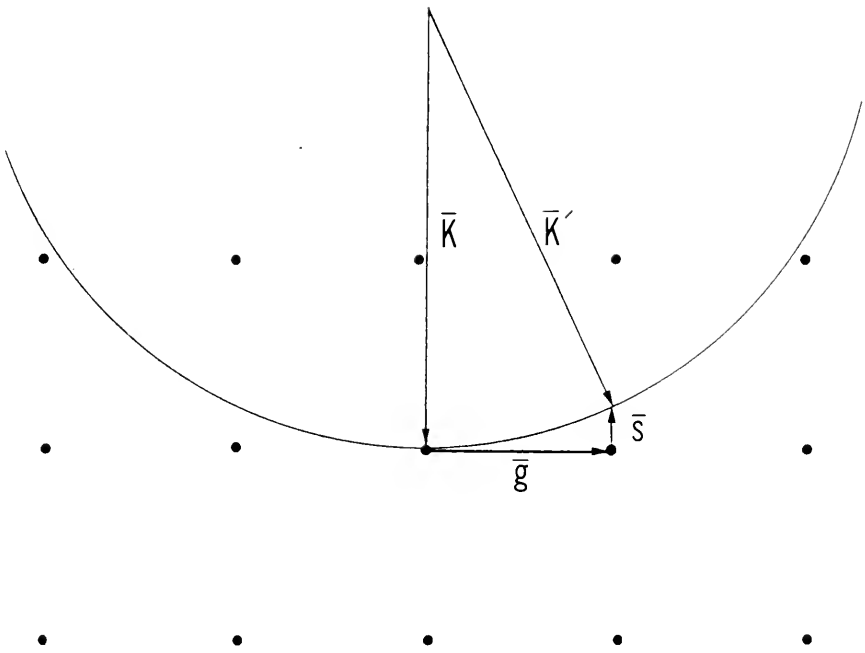

Fig. 4. The reciprocal space definition of $\bar{s}$, the deviation from Bragg.

the amplitude and phase of both the incident and one diffracted wave as a function of penetration into a crystal. These equations are equivalent to the Howie-Whelan equations, which were first presented in a phenomenological way to describe the two beam diffraction. The Howie-Whelan equations are

$$\frac{d\Phi_o}{dz} = i\pi\left[\frac{1}{\xi_o} + \frac{i}{\xi'_o}\right]\Phi_o + i\pi\left[\frac{1}{\xi_g} + \frac{i}{\xi'_g}\right]\Phi_g \exp(2\pi isz + 2\pi i\bar{g}\cdot\bar{u})$$

$$\frac{d\Phi_g}{dz} = i\pi\left[\frac{1}{\xi_o} + \frac{i}{\xi'_o}\right]\Phi_g + i\pi\left[\frac{1}{\xi_g} + \frac{i}{\xi'_g}\right]\Phi_o \exp(-2\pi isz - 2\pi i\bar{g}\cdot\bar{u})$$

Integration of these equations with respect to Z yields Φ_o and Φ_g at any depth Z. The intensity of the beams are $\Phi_o\Phi_o^*$ and $\Phi_g\Phi_g^*$, respectively. Both the Howie-Whelan equations above and the Bloch wave equations can be written in the matrix formulation

$$T' = (T + \Delta T) = A_{11}T + A_{12}S$$

$$S' = (S + \Delta S) = A_{21}T + A_{22}S$$

where T and T' are the incident waves at the top and bottom of a ΔZ of crystal, and S and S' are the diffracted waves at the top and bottom of a ΔZ of crystal. In the above

$$A_{11} = \frac{\exp(-\pi\eta\Delta Z)}{2Q}[(iw + Q)\exp[\pi(iw-Q)\Delta Z] - (iw-Q)\exp[\pi(iw + Q)\Delta Z]]$$

$$A_{12} = A_{21} = \exp(-\pi\eta\Delta Z)\frac{(i-A)}{2Q}[\exp[\pi(iw+Q)\Delta Z] - \exp[\pi(iw-Q)\Delta Z]]$$

$$A_{22} = \frac{\exp(-\pi\eta\Delta Z)}{2Q}[(iw+Q)\exp[\pi(iw+Q)\Delta Z] - (iw-Q)\exp[\pi(iw-Q)\Delta Z]]$$

where $w = s\xi_g$ and $Q^2 = 1 - w^2$.

This mathematical expression of the diffraction process is entirely compatible with the conceptual picture presented before, which ignored absorption terms and assumed the exact Bragg condition. Putting n, $\mathcal{A}$ and w equal to zero in the above equations results in

$$A_{11} = A_{22} = \cos(\pi \Delta z)$$

$$A_{12} = A_{21} = i \sin(\pi \Delta z)$$

Consider a small ΔZ. The matrix elements A_{11} and A_{22} (in the ideal case) simply reduce the amplitude of the T and S, respectively, to account for the intensity which has been scattered into the other wave. The elements A_{12} and A_{21} take a portion of each wave and add it to the other, after applying the 90^{o} phase shift discussed before (multiplying by i rotates any complex vector by 90^{o}). The intensity versus depth curve resulting from these equations, when expected values of normal and anomalous absorption are used, appears in Fig. 5. Normal absorption has damped the intensities, and anomalous absorption has set a minimum intensity.

Strictly, the Howie-Whelan equations apply only to a large, flat, perfect crystal. A number of assumptions are required to extend their use to a crystal containing a defect. The material along a ray leading to an image point is considered to be a column of material independent of the other columns. That is, electrons in one column do not diffract into a neighboring column. Because the Bragg angle is so small, this approximation is valid in general if the columns are further apart than 2 nm.

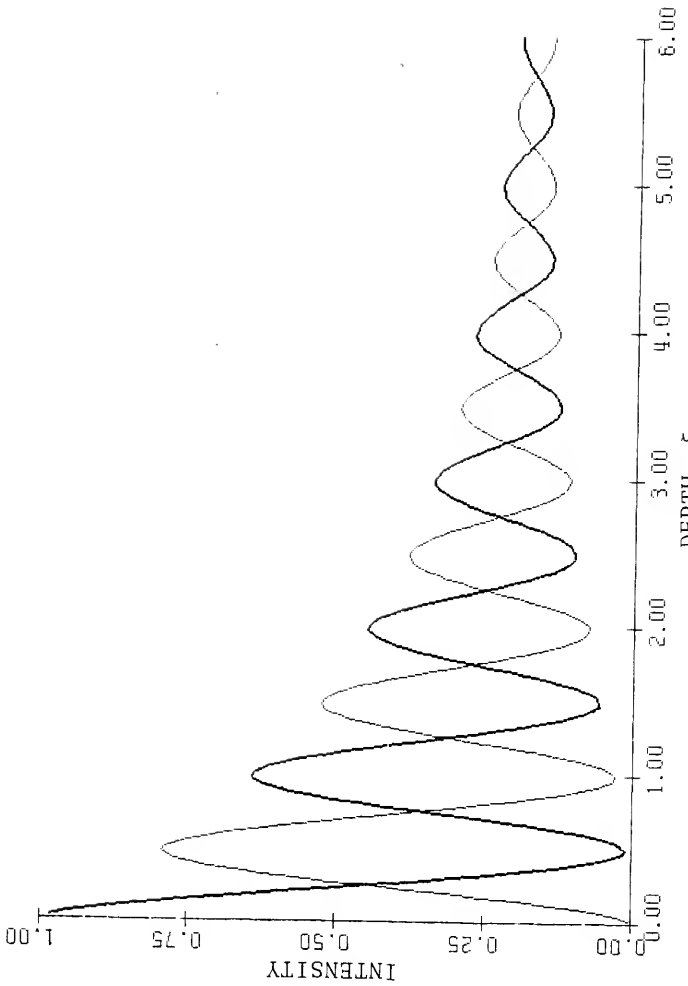

Fig. 5. Transmitted (heavy curve) and diffracted intensities for dynamical diffraction including normal (η = 0.08) and anomalous (A = 0.07) absorption.

In the calculation of intensities, the defect makes its presence felt as outlined in Fig. 6. Each increment ΔZ of a column is assumed to be an element of perfect crystal deviating from the Bragg condition by s. The operation

$$T' = A_{11}T + A_{12}S$$
$$S' = A_{21}T + A_{22}S$$

is carried out for each ΔZ, using values for the scatterng matrix appropriate for the local value of s. For perfect crystals, each ΔZ of column has the same value of $s = s_o$. With a defect present, the lattice planes nearby are distorted, giving rise to variations in the local value of s given by $s = s_o + [d(\bar{u}\cdot\bar{g})/(dz)]$, where s_o = mean value of s for the crystal, $\bar{u}$ = displacement due to the defect, and $\bar{g}$ = the diffracting vector. The term $[d(\bar{u}\cdot\bar{g})/(dz)]$ can be thought of as the local inclination of the lattice planes. The term $\bar{u}\cdot\bar{g}$ itself however is of prime importance; the derivative is used because of the differential form of the equations used.

The simplest explanation of the origin of image contrast is given by kinematic theory. The assumptions of this theory--that every atom receives the same incident energy and that the intensity of the diffracted beam is always negligible compared to the incident beam--are rarely met in electron diffraction, but the same mechanism producing contrast in the kinematical theory produces contrast in the dynamical theory. At the Bragg condition, the waves scattered by every atom constructively interfere in the direction of the diffracted beam. Atoms near a

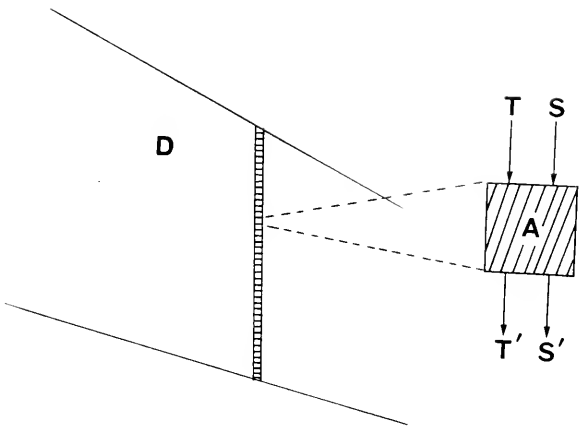

Fig. 6. Calculating the intensity of an image point. The wave passing through the columns above and image point are integrated by the scattering matrix algorithm (schematically represented by the block A). The value of A depends on the displacements from the defect D.

defect are displaced from their perfect crystal positions, and these scatter waves whose phase is shifted by the amount $2\pi(\bar{u}\cdot\bar{g})$ relative to the waves scattered by atoms in perfect crystal positions. The regions of the dark field image coming from displaced atoms will be dark, because of the incomplete constructive interference.

As seen above, the incident and diffracted waves are generally of comparable intensity in dynamical diffraction and account must be made of the contribution each scatters into the other. As the dynamically diffracting waves pass through a region of deformed material, the phase shifts from displaced atoms result in constructive interference to a greater or lesser extent than in perfect material. The change in phase and amplitude generally causes the transmitted and diffracted waves to be different from the perfect crystal case, creating contrast; the image may be brighter or darker than the normal intensity. Figure 5 shows that at alternating depths, first the incident beam and then the diffracted beam dominate in intensity. These regions are referred to as L-layers. The alterations in phase and amplitude which occur if the waves encounter displaced material when the incident beam dominates are opposite to those occurring when the diffracted beam dominates. Images of straight dislocations reveal this by their alternating contrast. The images of small defects have similar reversals in contrast, depending on their depth in the foil. Katerbau (1976) has used the Bloch wave approach to derive equations which give the incident and

diffracted intensities as a function of defect type, defect depth, and foil thickness. The systematic dependence of contrast on these parameters was expressed by Rühle et al. (1965) and is paraphrased as follows:

> 1) High-contrast bright field images are expected for foils of thickness $t_1 = (2n + 1)\xi_g/2$ ($n = 0,1,2,3...$); high-contrast dark field images are expected for foils of thickness $t_2 = n\xi_g$ ($n = 1,2,3...$).
>
> 2) For images in good contrast, the contrast of interstitial defect images will be opposite that of vacancy defects.
>
> 3) For a vacancy type defect located at a distance $d = n\xi_g/2$ ($n = 0,1,2,3...$) in from the nearest foil surface will, for bright field images, have the white lobe of its image on the $+\bar{g}$ side of the image if n is even, and on the $-\bar{g}$ side if n is odd. For dark field images of vacancy type defects, the above is true if the defect is nearer the electron entrant surface, but the contrast is reversed for defects near the exit surface.

The contrast reversals with defect position are illustrated in Fig. 7. Note that the dark field images are not suppressed at the center of the foil. With the exception of rule 2, the need for these rules are set aside by computer calculations of the actual images in the next chapter, which shows the contrast of an interstitial dislocation loop positioned at various depths in a foil of variable thickness.

An experimental complication must be pointed out. It is preferable electron-optically to obtain dark field images by tilting the beam so that $-\bar{g}$ is operating rather than to simply move the objective aperture to $+\bar{g}$. The contrast of a defect near the top of a foil will thereby be reversed,

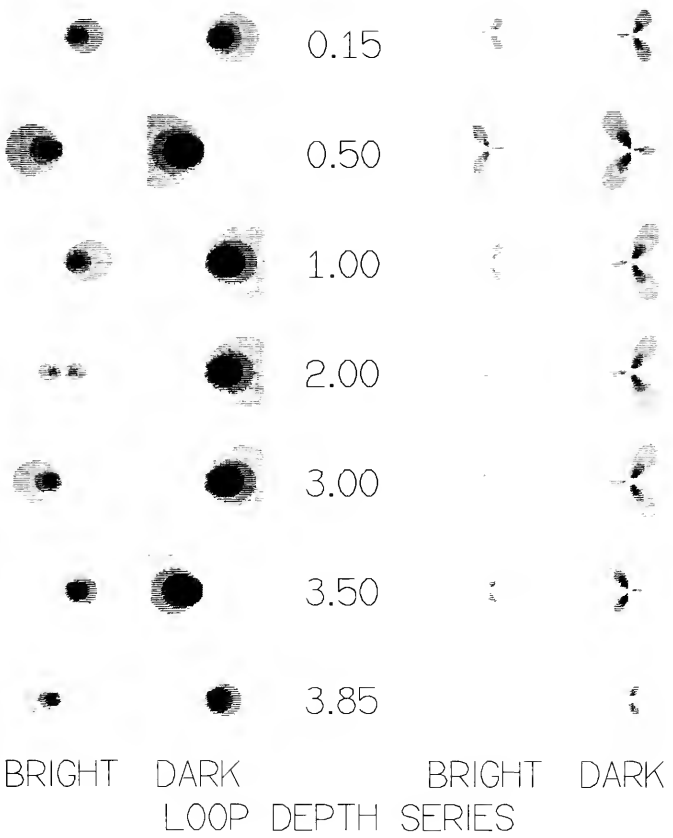

Fig. 7. Black-white behavior for bright and dark field. Interstitial loops in a 4.0 ξ_g thick foil.

whereas defect images near the bottom of the foil will remain unchanged.

A more quantitative (but still approximate) description of diffraction around a defect will aid the intuitive understanding of this contrast behavior. Figure 8a schematically shows the transmitted and diffracted waves at 1.0 ξ_g into a perfect crystal. At this depth the incident beam dominates in intensity as seen in Fig. 5. Due to anomalous absorption, the waves are 180^o out of phase. The incident beam is diffracting electrons into the diffracted wave 90^o out of phase with itself, a process represented by the dotted wave (for simplicity, diffraction of the diffracted wave into the incident wave is considered negligible at this point). If at this point displaced atoms are encountered, the contribution of the incident wave into the diffracted wave will have its phase shifted by $2\pi(\bar{u}\cdot\bar{g})$. For the beam passing the interstitial defect in Fig. 9, $2\pi(\bar{u}\cdot\bar{g})$ will be positive, advancing the phase of the diffracted part of the incident beam (dotted wave). Advancing the phase causes the curve to lag. This results in less complete constructive interference for the diffracted wave, decreasing its intensity. The intensities of the incident and diffracted wave for this case are shown in Fig. 10, and are compared to the values which occur in perfect crystals. If the defect were vacancy type, the displacements would be towards the defect. The term $2\pi(\bar{u}\cdot\bar{g})$ will be negative, retarding the phase and so enhancing the constructive interference. The diffracted beam will

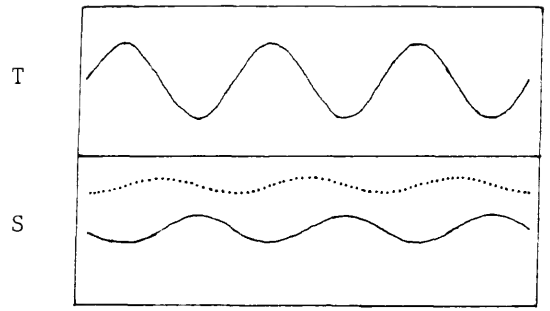

(a)

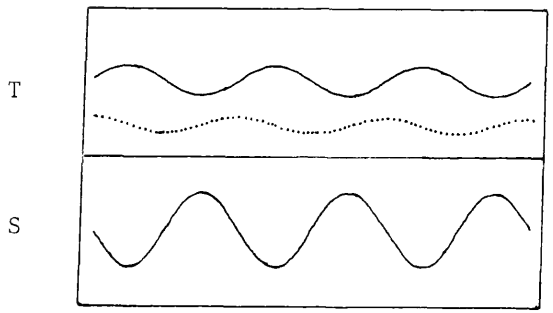

(b)

Fig. 8. Amplitude and phase relationships of the transmitted and diffracted waves at (a) 1.0 ξ_g and (b) 1.5 ξ_g deep into the foil. In (a) the dotted curve represents electrons being diffracted from the incident beam into the diffracted beam. In (b) the dotted curve is diffraction of intensity from S into T.

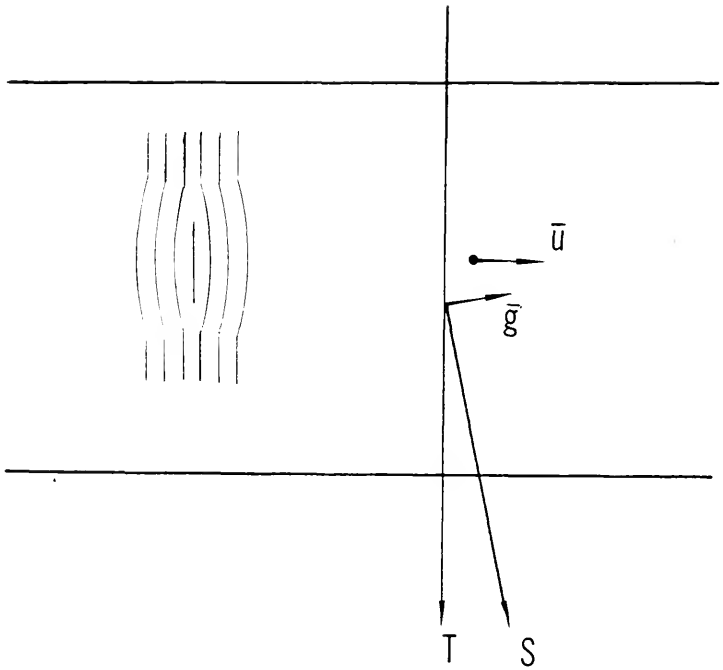

Fig. 9. The beam, $\bar{g}$ and displacements for the example given in the text.

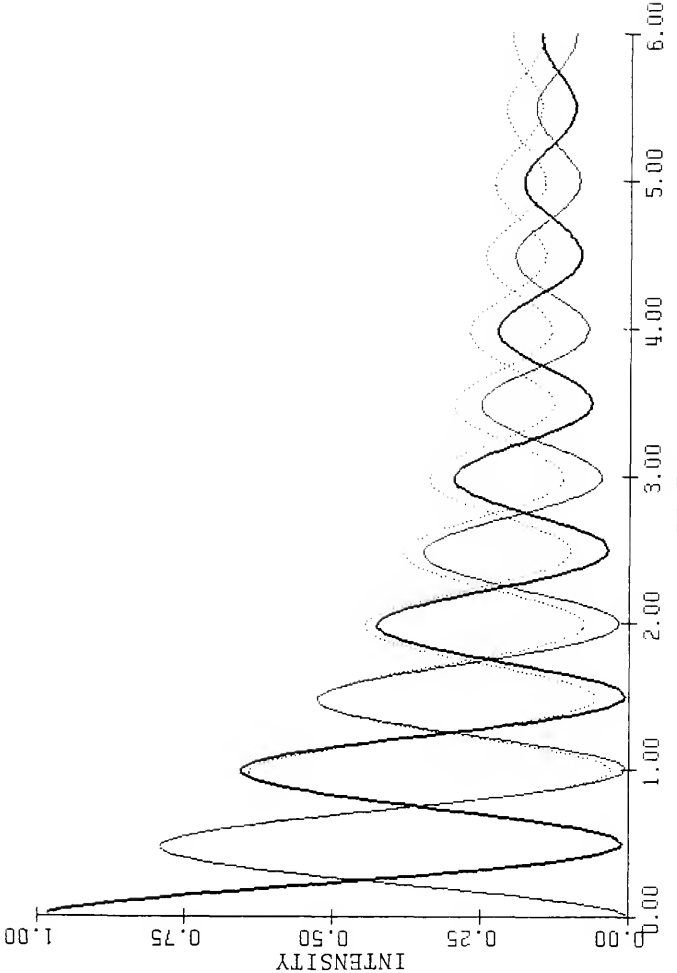

Fig. 10. Intensities of the transmitted and diffracted beams passing on the $+\vec{R}$ side of an interstitial defect 1.0 ξ_g deep into the foil. Dotted curves are the perfect crystal case for comparison.

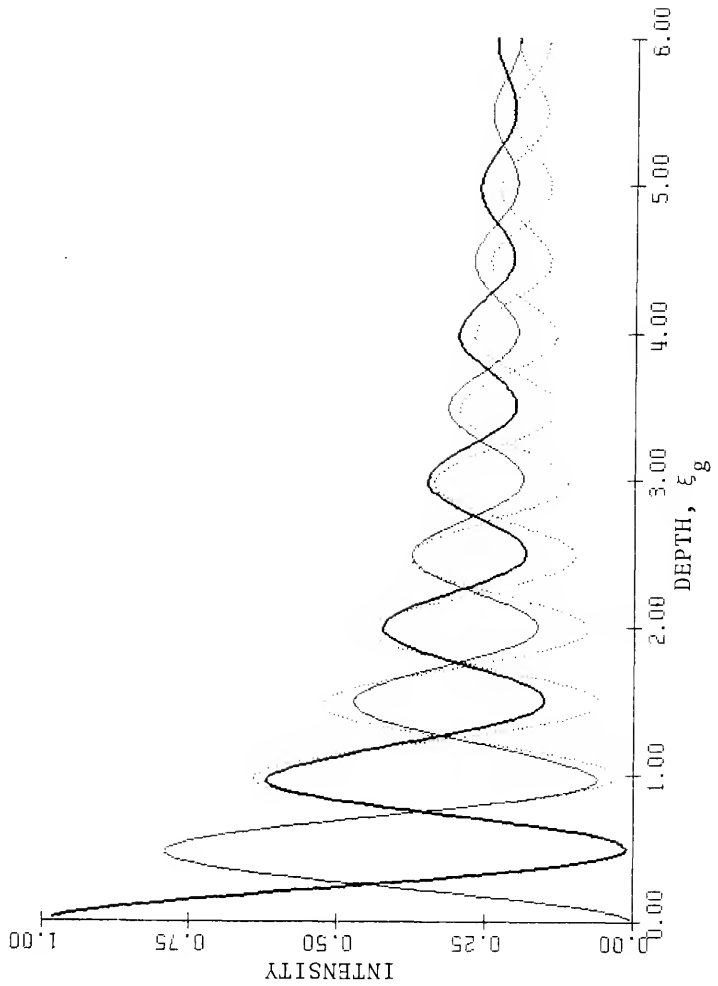

Fig. 11. Intensities of the transmitted and diffracted beams passing on the $+\vec{g}$ side of an vacancy defect 1.0 ξ_g deep into the foil. Dotted curves are the perfect crystal case for comparison.

increase in intensity (Fig. 11). It is easy to see that the contrast of a vacancy loop will usually be opposite that of an interstitial loop.

At half an extinction distance above or below the location just considered, the diffracted beam dominates in intensity (Fig. 8b). Again the incident and diffracted waves are 180^{o} out of phase. The important process occurring here is the diffraction of electrons from the dominant diffracted wave into the incident wave. For the moment, consider the diffracted beam to be the primary beam. Its diffraction is occurring by the opposite diffracting vector as the incident beam. Therefore, the phase shift of its contribution into the incident beam depends on $2\pi(\bar{u}\cdot(-\bar{g})) = -2\pi(\bar{u}\cdot\bar{g})$. For the interstitial defect in Fig. 9, $-2\pi(\bar{u}\cdot\bar{g})$ is negative, retarding the phase. As a result, the intensity of the incident wave increases over the values of the perfect crystal case, opposite the case above where the diffracted wave intensity decreased. This results in the reverse contrast behavior shown in Fig. 12 and Fig. 13.

Because integration of the Howie-Whelan equations is needed to obtain the intensity of the two waves as the beam proceeds beyond the displaced material around a defect, it is not easy to obtain an intuitive understanding of the process, but it is useful to note the trends which occur. If, when encountering displaced material, the lesser of the waves increases in intensity, the greater wave decreases in intensity (Fig. 12). This is a result of the tendency for

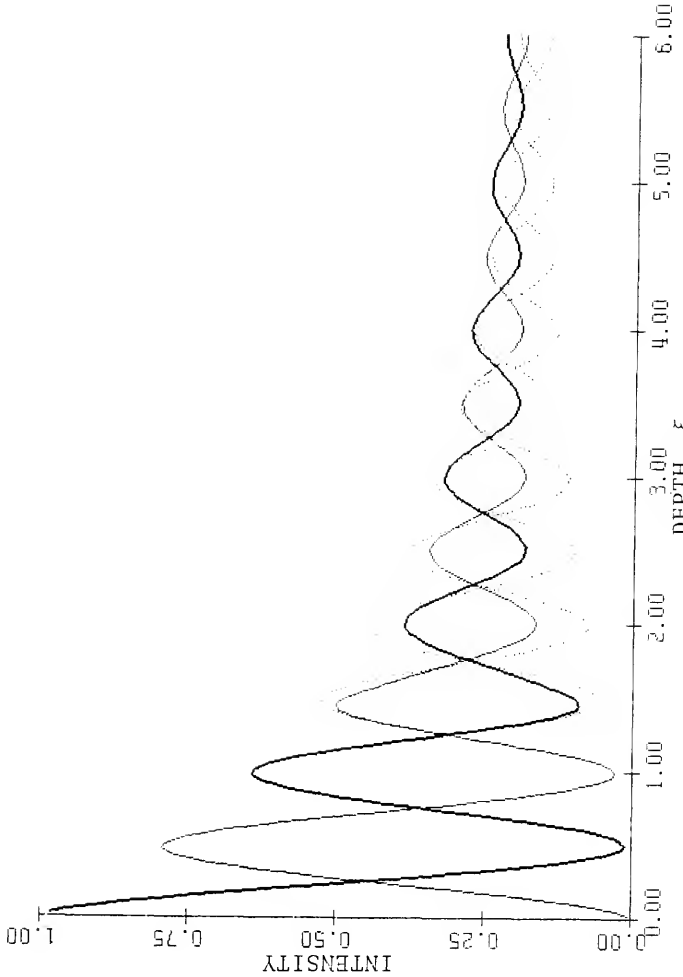

Fig. 12. Intensities of the transmitted and diffracted beams passing on the $+\vec{g}$ side of an interstitial defect $1.5\,\xi_g$ deep into the foil. Dotted curves are the perfect crystal case for comparison.

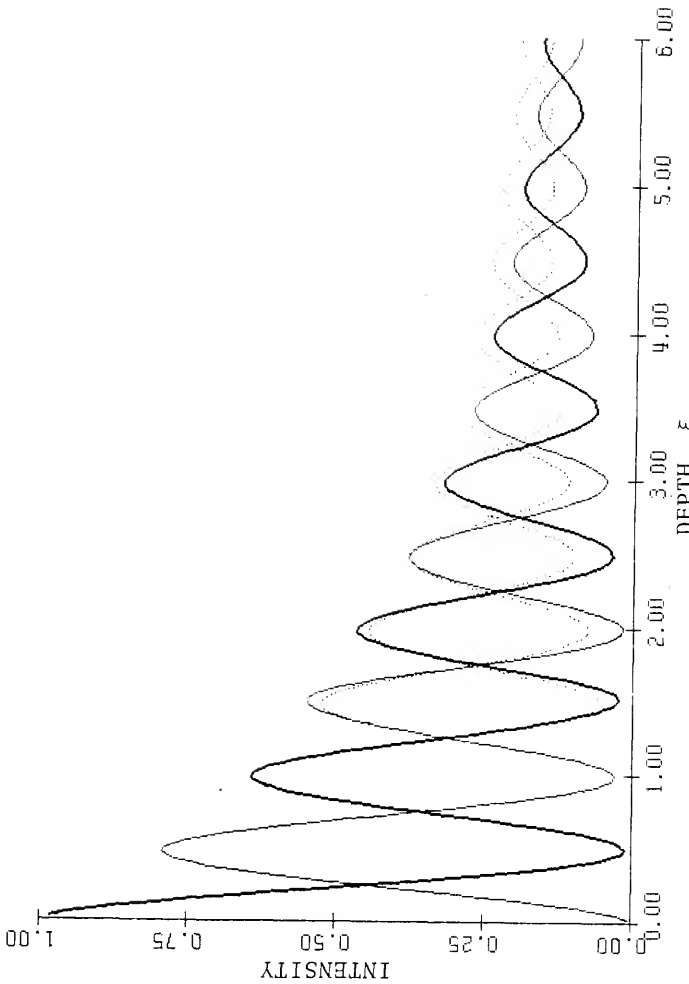

Fig. 13. Intensities of the transmitted and diffracted beams passing on the $+\vec{g}$ side of an vacancy defect 1.5 ξ_g deep into the foil. Dotted curves are the perfect crystal case for comparison.

energy to be conserved (if not for inelastic scattering events, energy would be conserved). In this case, after passing through sufficient material, both waves eventually have intensities above the perfect crystal case. Similarly, if the lesser wave decreases in intensity, the greater wave increases (Fig. 13). In this case, after passing through sufficient material for the absorption terms to have their effect, both waves decrease in intensity relative to perfect crystals.

The above observations allow explaination of the qualitative behavior of image contrast described by Rühle et al. (1965). The origin of the oscillation in contrast of defects encountered at different depths is seen above, as well as the reversal in contrast expected in changing from an interstitial type defect to vacancy type. Of interest now is the relation between bright and dark field images near the top and bottom surfaces. If the defect is near the upper surface, the beam passes through sufficient material before exiting the crystal that the absorption effects are important, and the incident and diffracted waves both have their intensities similarly altered above or below the perfect crystal background level. Thus, the contrast of defects near the upper surface does not reverse in going from bright to dark field. For the waves immediately after encountering a defect, the tendency to conserve energy results in the fact that if one wave has greater than normal intensity, the other has less than normal intensity. For a defect near the bottom surface, this trend prevails when the

exit surface is reached; bright and dark field images of defects near the bottom surface have opposite contrast.

The image relates back to the strain field of the defect, so the evaluation of the strain field of a dislocation loop is now considered. To evaluate the displacement $\bar{u}$ at a position $\bar{r}$ from the loop, the computer program used an infinitesimal approximation for the strain field. The approximation has the advantages of reducing computing time, is easily modified to model the strain field of other defects such as voids or particles, yields a displacement field simple enough to be intuitively manipulated, and most importantly, yields images which compare well with the experimental images of small dislocation loops.

Although they are relatively involved, the expressions for the displacements are arrived at by straightforward mathematical techniques. The major tool is the Green's function whose physical meaning is found in its definition,

$$u_m(\bar{r}) = U_{km}(\bar{r} - \bar{r}')\, f_k(\bar{r}')$$

where $u_m(\bar{r})$ is the displacement at $\bar{r}$, $f_k(\bar{r}')$ is the force applied at $\bar{r}'$, and $U_{km}(\bar{r} - \bar{r}')$ is the Green's function for the relative $(\bar{r} - \bar{r}')$. The Green's function gives the displacement $\bar{u}$ found at $\bar{r}$ which results from the force $\bar{f}$ applied at the point $\bar{r}'$. Using Hooke's law and the differential equations expressing the equilibrium of forces in a continuous medium, the Green's function for an infinite isotropic elastic continuum can be obtained (see DeWit, 1960):

$$U_{km}(\bar{r}) = \frac{1}{8\pi G}\left[\delta_{km}\bar{r}_{,pp} - \frac{\lambda + G}{\lambda + 2G}\,\bar{r}_{,km}\right]$$

If a defect can be described as a number of forces distributed in some spatial array, the displacement at any point is obtained by summing the displacements resulting from each force in the array

$$u_m(\bar{r}) = \int_S U_{km}(\bar{r} - \bar{r}')\, f_k(\bar{r}')\, dr$$

In a typical application, the forces tend to occur in equal and opposite pairs separated by a small distance. Consider the formation of pure edge vacancy loop in a continuum. Cuts are made, and a disk of material of radius a and thickness b is removed. To one surface of the disk an array of forces is applied which is equal and opposite a similar array of forces applied to the other surface. The forces are of magnitude such that the surfaces come together, forming a dislocation loop with burgers vector $\bar{b}$. It can be shown that the displacement due to a pair of closely spaced equal and opposite forces (called a force dipole) is

$$u_m(\bar{r}) = U_{km,\ell}(\bar{r} - \bar{r}')\, P_{k\ell}(\bar{r}')$$

$P_{k\ell}(\bar{r}')$ is a tensor describing the force dipole at $\bar{r}'$. For an element of surface ds with normal $\bar{n}$ across which a displacement $\bar{b}$ has been made, the assumption of linear elasticity (that stresses are proportional to strains) leads to

$$P_{k\ell} = C_{ijk\ell}\, b_i n_j\, ds$$

The above definition of $U_{km,\ell}$ is such that if $\bar{b}\cdot\bar{n} > 0$, the surfaces on which the force dipole acts are pushed apart (such as for an interstitial loop), and similarly $\bar{b}\cdot\bar{n} < 0$

means the surfaces are pushed together (vacancy loop). Using the force dipole definition, the displacements from a dislocation loop are

$$u_m(\bar{r}) = \int_S C_{ijk\ell}\ b_i n_j\ U_{km,\ell}(\bar{r} - \bar{r}')\ ds,$$

where $(\bar{r} - \bar{r}')$ is the vector from each element of the surface of the loop to the point of interest $\bar{r}$.

The expressions just described gives the displacement of a finite loop. The integration is difficult and the resulting numerical calculations are time-consuming. If displacements are being evaluated at a point distant from the loop, the vector $(\bar{r} - \bar{r}')$ will not vary significantly and can be assumed constant. This approximation $[(\bar{r} - \bar{r}') = \bar{r}]$ results in

$$\begin{aligned} u_m(\bar{r}) &= \int_S C_{ijk\ell}\ b_i n_j\ U_{km,\ell}(\bar{r})\ ds \\ &= C_{ijk\ell}\ b_i n_j\ U_{km,\ell}(\bar{r}) \int_S ds \\ &= C_{ijk\ell}\ b_i n_j\ (\pi a^2)\ U_{km,\ell}(\bar{r}) \end{aligned}$$

This approximation (the infinitesimal approximation) holds well for points distant from the loop but will become increasingly poor as the defect is approached (i.e., where $(\bar{r} - \bar{r}')$ varies significantly).

To obtain the displacement field of any defect, steps parallel to the above need to be taken. The defect must be described as an array of forces on some surface, the appropriate Green's function defined and the results integrated. In general, it is possible to employ the infinitesimal approximation to simplify the result, or to obtain a less accurate result when integration is not possible.

The displacements of points equidistant from a pure edge loop of both interstitial and vacancy type are shown in Fig. 14. They are cylindrically symmetric about the loop axis so that Fig. 14 represents any plane containing the axis. For the infinitesimal approximation, the magnitudes of the displacements are proportional to $1/|\bar{r}|^2$. The displacements of an interstitial loop with a shear term are shown in Fig. 15. These are not cylindrically symmetric, and so Fig. 15 refers only to the plane containing $\bar{b}$ and $\bar{n}$. However, the displacements appear quite similar to those for an unsheared loop. In fact, Fig. 14a overlaps Fig. 15 closely if it is rotated approximately 9° toward the burgers vector of the loop in Fig. 15. It can be expected, then, that a sheared loop could be modeled by a Frank loop whose habit plane normal is appropriately rotated from the normal towards its burgers vector. The appropriate rotation is between 1/4 and 1/3 of the way from the normal to the burgers vector. Thus, the sheared loop described by $\bar{n}$ and $\bar{b}$ can be approximated by the Frank loop with $\bar{n}' = \bar{b}' = (\bar{b}/3 + 2\bar{n}/3)$. This approximation is empirically valid for most images and is useful because the images of a Frank loop are easy to predict. Because of this result, the parameter $\bar{n}$ will be the chief parameter for describing a loop in this work; $\bar{b}$ will be used only as a secondary description needed to define small sheared loops. Of course, for those dislocation loops large enough to be resolved, the character of the image depends on the local line direction and burgers vector.

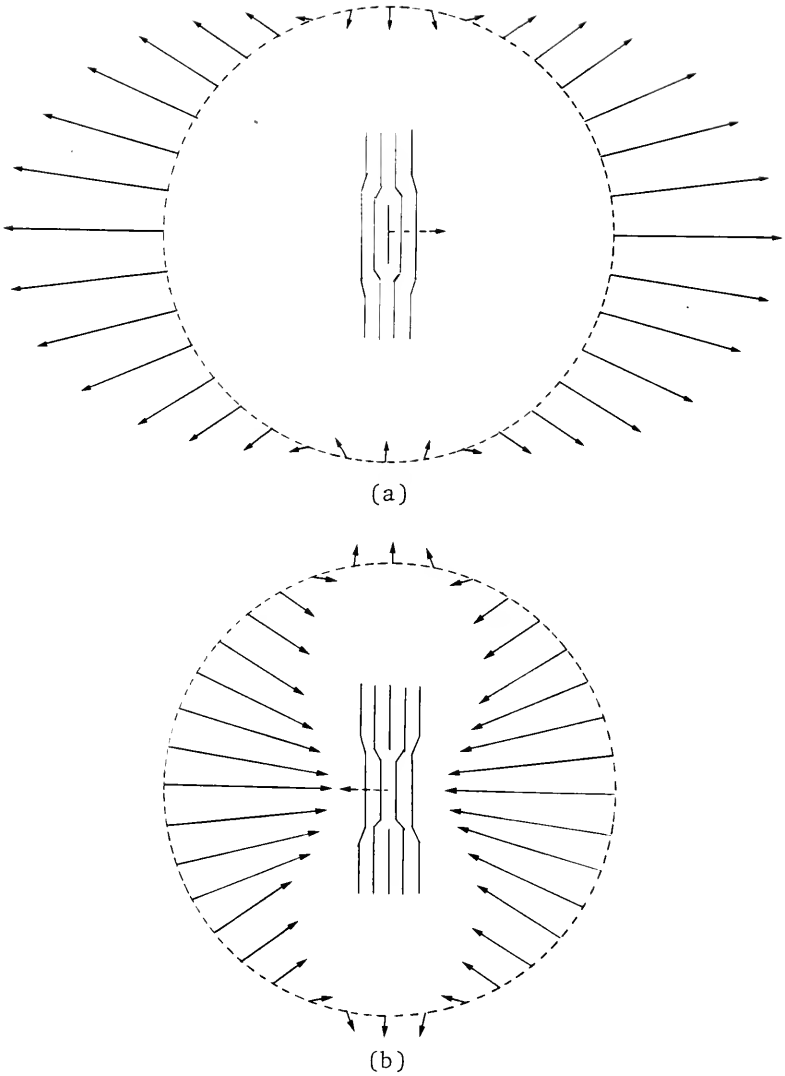

Fig. 14. The displacements about a pure edge (a) interstitial and (b) vacancy loop. The displacements are for points equidistant from the defect and are grossly exaggerated.

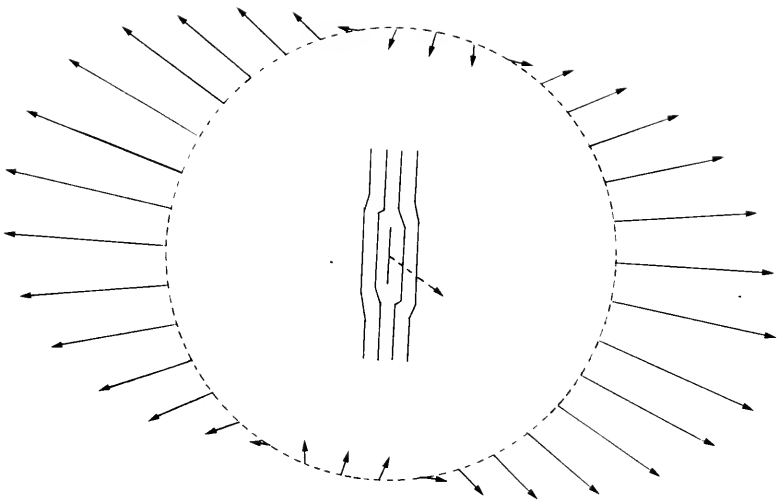

Fig. 15. The displacements about an interstitial loop with a shear component in its burgers vector.

In calculating an image, the displacement field of a defect appears as the quantity $d(\bar{u}\cdot\bar{g})/dz$. That is, the image is sensitive only to the displacements in the direction $\bar{g}$. The importance of $\bar{u}\cdot\bar{g}$ is better illustrated using the following graphical representation. Consider the displacments at a constant distance from the loop, in a plane normal to the incident beam and intersecting the loop. These displacements are resolved into a direction $\bar{g}$, producing $\bar{u}\cdot\bar{g}$. This function is plotted in Fig. 16 for three different directions $\bar{g}$ as $r(\theta) = \bar{g}\cdot\bar{u}(\theta)$, where $\bar{u}(\theta)$ is the displacement at a unit distance from the loop and at an angle θ from $\bar{g}$. If $\bar{g}\cdot\bar{u}(\theta)$ is negative, the line is plotted with a dotted line rather than a negative value of r. The method becomes less valid as the habit plane normal deviates from the image plane. Although this graphical method is presented only to develop an intuitive relationship between the displacement field and the image, the comparison with accurately calculated images is striking. The development and meaning of this construction is most easily seen for the case in Fig. 16 where $\bar{g}$ aligns with the loop normal. The greatest displacement is in the direction of the loop normal. This displacement is fully resolved into $\bar{g}$, producing a large value of $\bar{u}\cdot\bar{g}$. The polar displacement plot extends quite far in that direction. The small inward displacements resulting from the collapse of material around the edge of the loop are not at all resolved into $\bar{g}$, so $\bar{u}\cdot\bar{g} = 0$. The polar displacement plot (and the image) extends zero distance in the plane of the loop.

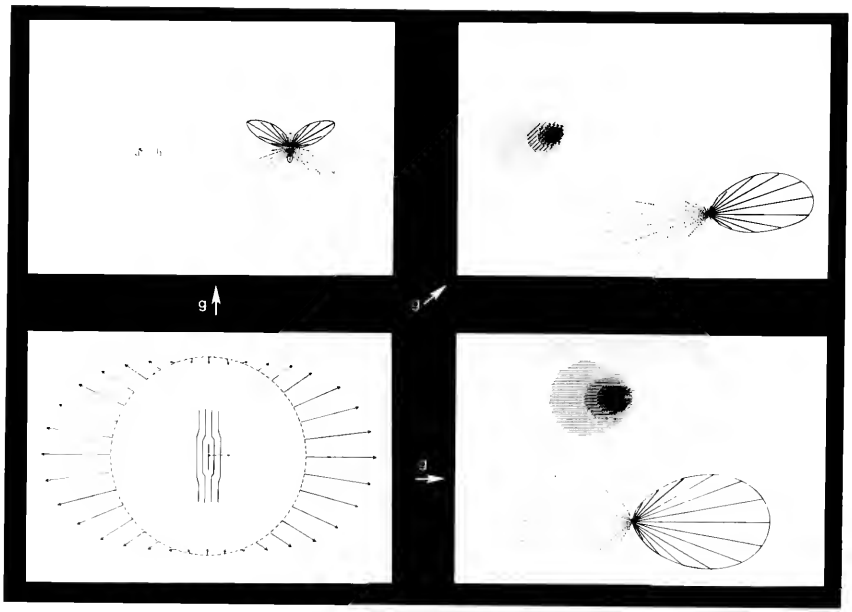

Fig. 16. The vector u as a function of θ around the loop resolved into several directions. The magnitude of the scaler product $(\bar{u}\cdot\bar{g})$ is plotted in a polar manner.

Displacements of material 45^{o} from the loop normal produce a small value of $\bar{u}\cdot\bar{g}$, and the polar displacement plot extends a short distance in this direction. The origin of the butterfly image is made clear from this construction. The small lobes aligned with $\bar{g}$ of these images are seen to arise from the inward collapse of material around the circumference of an interstitial loop.

As has just been presented, the main elements of the electron image formation process can be separated and understood in a qualitative manner. It is possible, then, to predict the major features of a dislocation loop image if the various relevant parameters are known. Its orientation relative to the beam direction and diffracting vector determine the major topographic features of the image. The above or below background nature of regions of the image can be deduced from the defect's interstitial or vacancy nature, and its position in the foil. Ignoring the effort required to make such an estimation of an image, it is less preferred than a computer calculation, because sufficient confidence cannot be placed on the estimate. Nevertheless, this understanding provides a base from which the more accurate computer simulated images can be interpreted, and from which any trends in image behavior can be recognized and extrapolated.

CHAPTER IV
COMPUTER EXPERIMENTS AND THE CATALOGS

The theory presented in the last chapter can explain much of the image behavior of small defects, but it does not quantitatively provide the response of an image to all imaginable sets of parameters. For example, exactly how does the image depend on the orientation of a loop? What is the effect of the deviation from the Bragg condition? The theory presented can allow these and similar questions to be tentatively answered, but the use of computer calculated images is easier, and produces more confident results. Computer studies will show which parameters have the greatest effect on the image. These effects decide what parameters must be included in a catalog of images intended for use in defect identification. Some parameters will prove to have little effect, and the computer studies decide the best representative values for these. These studies also extend and reinforce the understanding presented in the last chapter. The structure, philosophy and use of these catalogs will also be briefly outlined and illustrated.

The contrast vector, $\bar{\ell}$, drawn from the black lobe of an image to the white lobe, is known to vary with the defect's depth in a foil. Rühle et al. (1965) have given rules describing this behavior. Rather than working out these

rules, it is preferable to merely look up an image for a defect at a particular depth in a foil of a given thickness. Figures 17 and 18 provide this ability. The bright field and dark field images of a pure edge interstitial dislcoation loop are shown in these figures as a function of foil thickness and defect depth. The layout mimics the contrast expected from a wedge-shaped foil with a thickness increasing from one-quarter to five extinction distances. The depth of the defect is represented by the position of the image in each column, the topmost image corresponding to a depth one-eighth extinction distance down from the top surface and the bottom image one-eighth extinction distance up from the bottom surface. The gray levels were obtained by normalizing the intensities for a particular image by those obtained for a perfect crystal of the same thickness. Thus, the thickness contours normally associated with a wedge-shaped crystal do not appear.

The image contrast rules for a small dislocation loop described by Rühle et al. (1965) can be easily deduced from these composites. Note that thicknesses giving good contrast in bright field images give poor contrast in dark field and vice versa. Note, too, that the black-white direction of an image oscillates with depth for both bright and dark field images, and that the bright and dark field images have the same black-white direction near the top of the foil but have opposite directions near the bottom. The illustrations of Rühle, and his reference to defect distance from the nearest foil surface, tend to pass over the

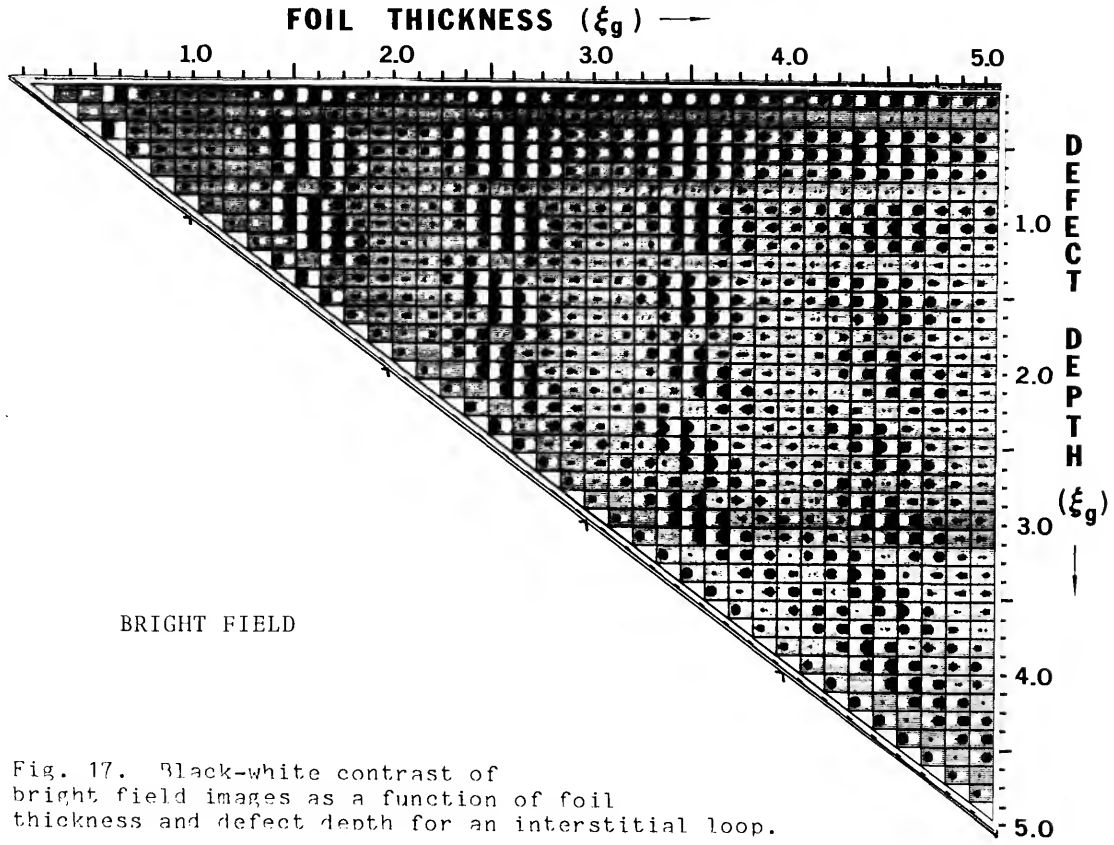

Fig. 17. Black-white contrast of bright field images as a function of foil thickness and defect depth for an interstitial loop.

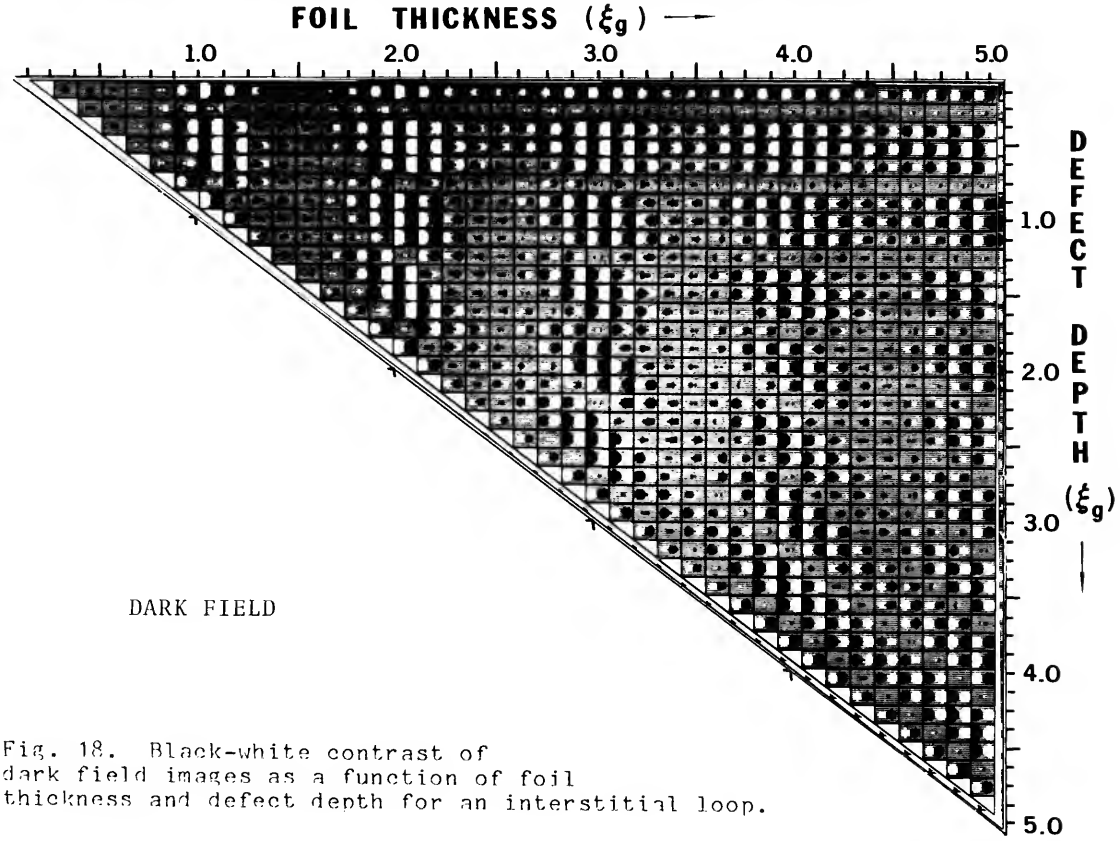

Fig. 18. Black-white contrast of dark field images as a function of foil thickness and defect depth for an interstitial loop.

contrast of defects near the center of the foil. As seen here, good contrast can occur in bright field images for defects near the center and in dark field images for defects at the center.

The images for vacancy type defects are obtained by reversing the contrast seen here. This rule does not apply to images in poor contrast which normally appear as small black dots independent of the interstitial or vacancy nature of the defect. Due to surface relaxations, experimental images of defects very near either surface are expected to be slightly different from those seen here.

To augment the relationship between the displacement field and the image, as presented in the last chapter, the change of the image with loop orientation can be visualized with the help of the following simulation experiment. Holding the foil geometry, diffracting conditions, and defect depth constant, the inclination of the habit plane of a Frank loop is varied through the wide angular range indicated in Fig. 19a. This is not a physically realizable experiment, of course, but it gives useful results nonetheless. Figure 20a is an expansion of the lower right quadrant, showing the dependence of the image on orientation in a more continuous manner. Figures 19b and 20b are stereographic projections giving the loop normal direction for the images. As for all images presented in this work, the direction of $\bar{g}$ projected onto the image is to the right. Because the image shifts so dramatically from one direction of skewness to the other in making the transition through

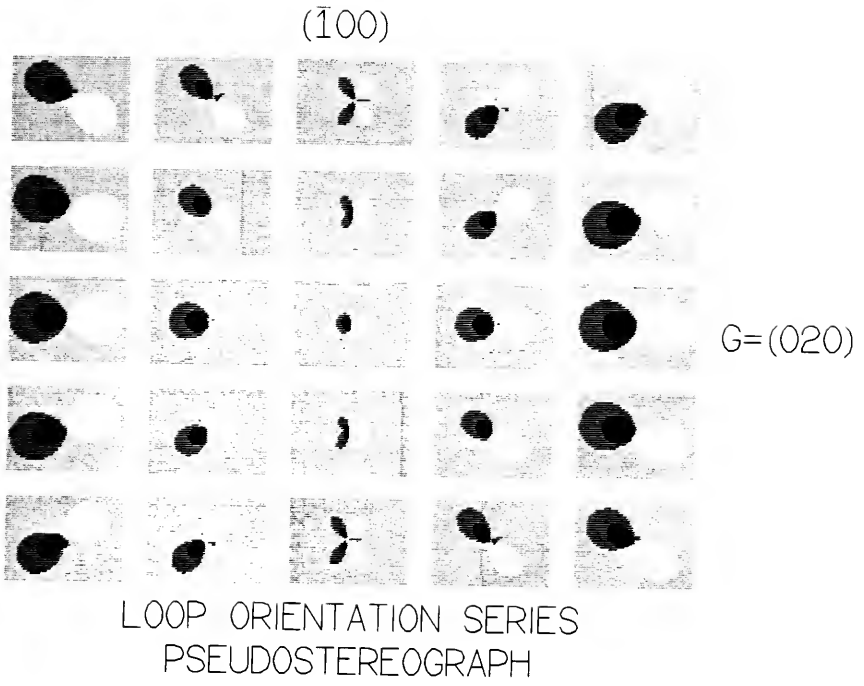

Fig. 19. (a) Interstitial loops having varying orientations in the upper hemisphere. (b) Poles of the loop normals corresponding to Fig. 19(a).

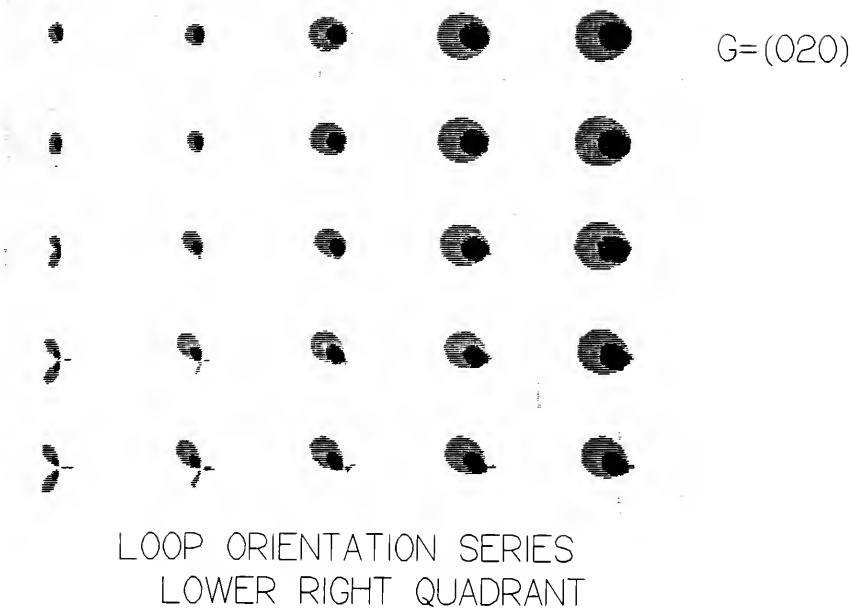

Fig. 20. (a) The lower right quadrant of Fig. 19(a) expanded. (b) Poles of the loop normals corresponding to Fig. 20(a).

the butterfly image, this image type gives the greatest sensitivity to the orientation of the loop. For example, a Frank loop oriented so that a strong butterfly image is obtained can be easily distinguished from a sheared loop, because the latter will show considerable skewness.

One pattern apparent from Fig. 20a is that the black-white direction , $\bar{\ell}$, deviates from $\bar{g}$ by about 2/3 of the angle from $\bar{g}$ to the projection of $\bar{n}$. The ℓ-vector hypothesis and the approximation $\bar{n}' = (\bar{b}/3 + 2\bar{n}/3)$ was tested for all of the images in the fcc and bcc catalogs. The ℓ-vector was determined (when possible) by constructing a vector from the centroid of below-background intensities to the centroid of above-background intensities. The angle from $\bar{g}$ to $\bar{\ell}$ is plotted in Fig. 21 versus the angle from $\bar{g}$ to the projection of $\bar{n}$ (or $\bar{n}'$) onto the image. In experimental loop images it is difficult to determine the black-white direction with enough confidence to make this trend quantitatively reliable, but these results do confirm the qualitative validity of the rule.

The full range presented in Fig. 19a and Fig. 20a demonstrates that there are few image types expected. At this point, the adequacy of the infinitesimal approximation can be evaluated by comparing images calculated using a finite strain field with images calculated using the infinitesimal approximation. Figure 22 compares some infinitesimal loop images from the bcc catalog with finite loop images calculated by Eyre et al. (1977a). The format mimics that of Fig. 20a. The finite loop calculations

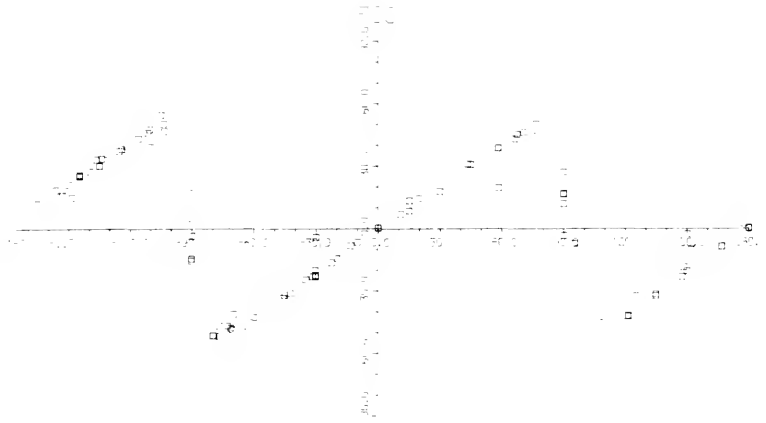

(a)

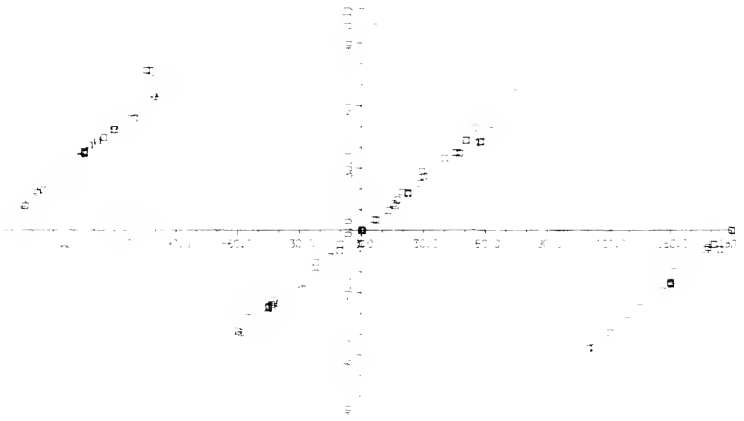

(b)

Fig. 21. The angle of the black-white directions deviating from $\bar{a}$ plotted as a function of the angle of the deviation of the projection of $\bar{n}' = 2\bar{n}/3 + \bar{b}/3$ onto the image plane. (a) Data are from all the images in the fcc Catalog; (b) data are from all the images in the bcc Catalog.

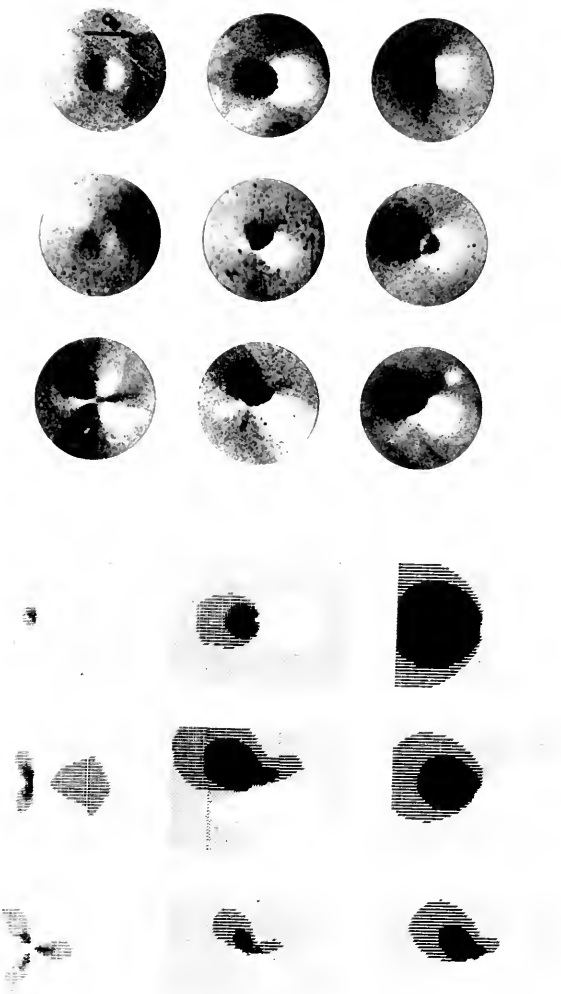

Fig. 22. Comparison of the finite loop images of Eyre et al. (1977) (oriented so the operating diffracting vector is to the right) to the corresponding infinitesimal loop images of the bcc Catalog.
$\bar{n}=(011)$, $\bar{g}=(011)$; $\bar{n}=(111)$, $\bar{g}=(200)$; $\bar{n}=(01\bar{1})$, $\bar{g}=(01\bar{1})$;
$\bar{n}=(111)$, $\bar{g}=(01\bar{1})$; $\bar{n}=(110)$, $\bar{g}=(01\bar{1})$; $\bar{n}=(1\bar{1}1)$, $\bar{g}=(2\bar{1}1)$;
$\bar{n}=(01\bar{1})$, $\bar{g}=(200)$; $\bar{n}=(101)$, $\bar{g}=(21\bar{1})$; $\bar{n}=(01\bar{1})$, $\bar{g}=(2\bar{1}1)$.

produce fine detail in the images near the loop not obtainable by the infinitesimal approximation, particularly between the black and white lobes for the case $|\bar{g}\cdot\bar{b}| > 1$. Such a structure is hinted at in some of the infinitesimal images, but because the only non-zero term in the dipole tensor used in simulating an edge loop depends on the size of the loop as well as its burgers vector, this reversal can result from using a large value for the loop radius. Discussions of the details of such finite loop calculations are found in the works of Eyre et al. (1977a,b). Figure 22 is presented here only to indicate when and how the infinitesimal approximation may be insufficiently precise.

The value of $w = s\xi_g$ has a very pronounced effect on the images of straight dislocations and other extended defects (Head et al., 1973). As Fig. 23 shows, however, the images of small loops suffer only minor variation in contrast intensity over a wide variation in w. The reversal of contrast occurring at large values of w results from the decrease in effective extinction distance. The general shape and symmetry of the images is unaffected. This is quite a fortunate result, since it relaxes the need to accurately know the value of w for an experimental image. The ratio of anomalous absorption to normal absorption also has great influence on the images of straight dislocations (Head et al., 1973). Variations of this parameter from 0.05 to 0.10 (the usual range expected) cause little qualitative change in images of small defects for a given value of w (Cooper, 1977).

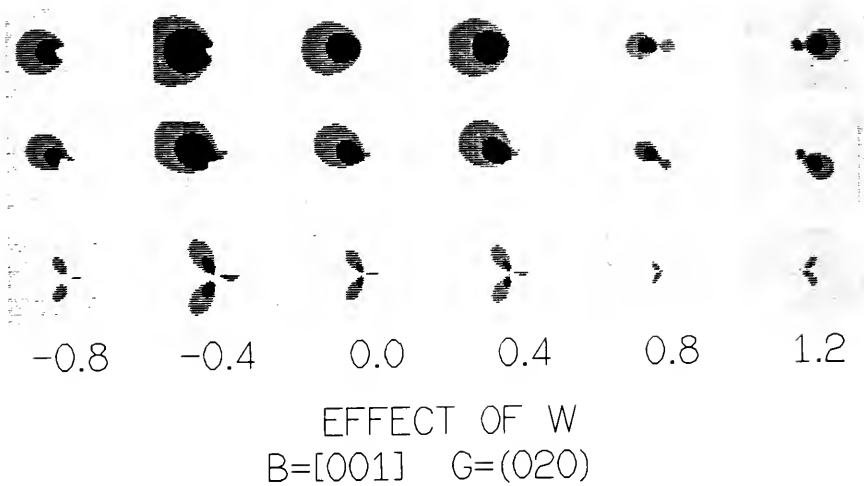

Fig. 23. Effect of the deviation parameter $w = s\xi_g$ on three image types. Loops are interstitial types, $0.5\,\xi_g$ deep in a $4.0\,\xi_g$ thick foil. Diffracting vector is (200) in aluminum.

All the images in the catalogs were calculated for the foil normal set parallel to the beam direction. This condition cannot always be met experimentally. Figure 24 shows the purely geometric effects of tilting the foil. The thickness and mean depth of the defect are both increased by the factor ($1/\cos\theta$). The effective depth of the defect in a particular column is a function of the column's position in the image. Complications which can arise due to large foil tilts will probably require additional image simulations. Figure 24b shows a defect in a tilted foil near the top of an L-layer. The effective depth of the defect on the side towards which the foil normal has been tilted (i.e., on the right) will be near the boundary between L-layers, and thus give a weak image. The image on the other side will be strong because the effective depth of the defect is nearly centered in the L-layer. For the defect in Fig. 24d near the bottom of an L-layer, the same factors create the opposite effect. For a defect centered in the L-layer, the image will be weaker on both side (Fig. 24c).

The best experimental images are those in good contrast, corresponding to a defect near the center of an L-layer and viewed on edge. The effect of foil tilt in this case is shown in Fig. 25a, b and c for several image types. In each array, the center image has its foil normal parallel to the beam; the others have their foil normals tilted 30° toward the location of the picture (see Fig. 25d). The change in effective foil thickness has increased the overall

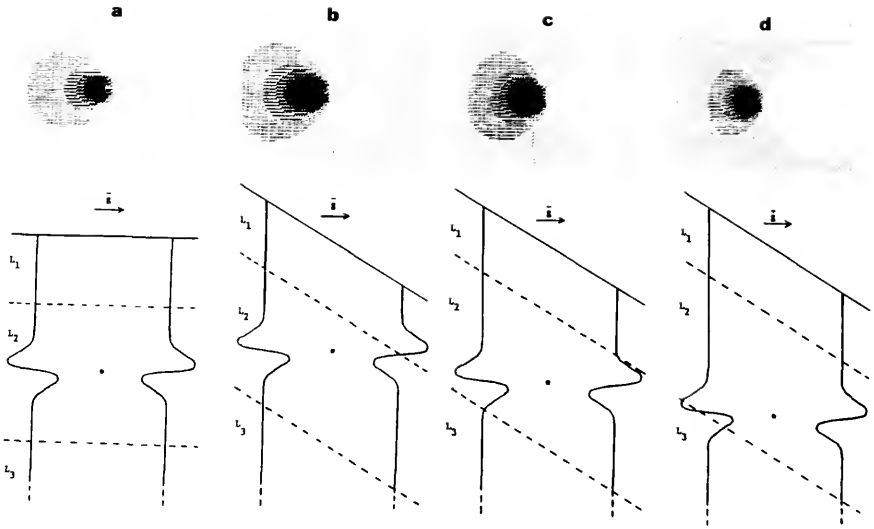

Fig. 24. Geometric changes produced for foil tilt and the resulting images.

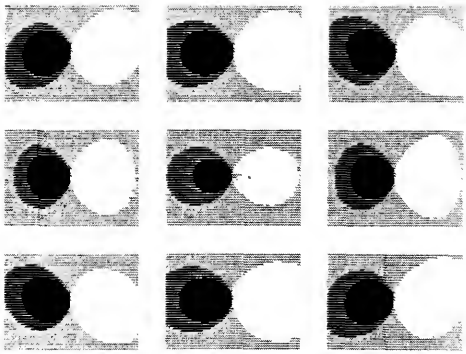

(a)

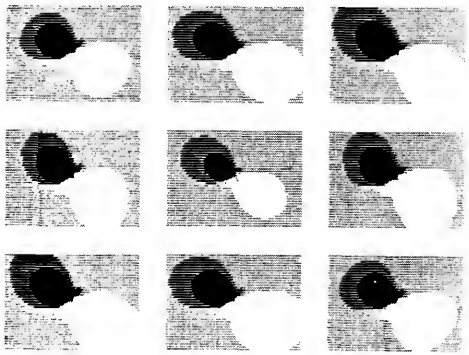

(b)

Fig. 25. Effect of 30° of foil tilt on three images: (a) $\bar{n}$ aligned with $\bar{g}$, (b) $\bar{n}$ 45 from $\bar{g}$, $\bar{n}$ in the image plane, (c) $\bar{n}$ perpendicular to $\bar{g}$, ($\bar{g}\cdot\bar{n} = 0$, $\bar{n}\cdot\bar{Z} = 0$), (d) stereogram showing the tilt of the foil normal relative to the beam direction for fig. 25(a, b, and c).

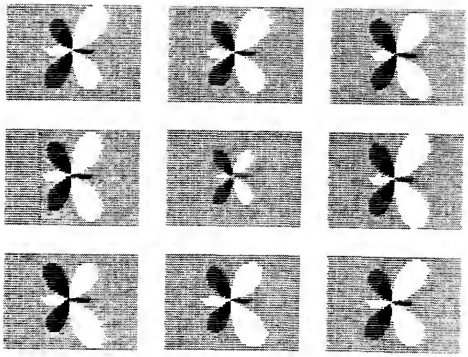

(c)

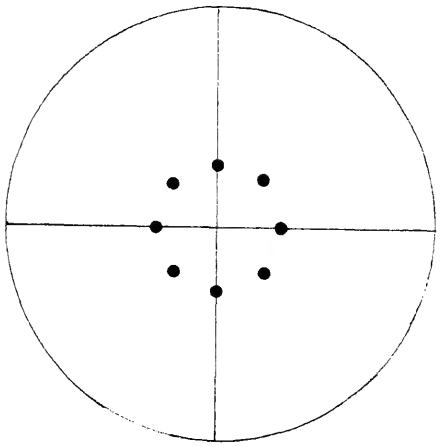

(d)

Fig. 25--continued.

contrast of the images. The most striking effect of foil tilt in this case is to compress the image in the direction toward which the foil has been tilted. This compression can effectively cause a rotation of the black-white direction. Post-experimental calculations are advised for conclusive identifications when large tilts ($> 25^{o}$) are required, but the overall effect is not so great that it interferes with the general usefulness of the images in the catalogs.

The information just presented was used to determine the structure and parameters of the catalogs for small dislocation loop identification. The complete fcc and bcc catalogs are given in the work of Sykes et al. (1981), which also includes a description of all parameters used in calculations and gives several examples of the usefulness of the catalogs. The catalogs are too extensive for inclusion here, but they are the focal point of all the preceding developments and the following summary is appropriate. The purpose of the catalogs is to allow the determination of the loop normal and burgers vector of a small loop without requiring the microscopist to work out the geometry from the various published rules. Identification of an experimental image is accomplished by direct comparison with computed images. With the images of all defect types and permutations logically ordered with respect to experimentally controllable parameters, it is possible to determine at a glance which experimental conditions provide the greatest distinction between the images of various defects. In this way, the microscopist can minimize the

number of micrographs needed to make a conclusive identification.

The microscopist can control only a few imaging parameters. Use of a double tilt goniometer stage gives him simultaneous control of the beam direction, the diffracting vector and the deviation from the Bragg condition. Control of the beam direction allows the microscopist to view the defect from any orientation; e.g, looking down on the face of the loop or viewing it on edge. At any beam direction it will be possible to use various diffracting vectors and so sample different portions of the displacement field (that is, different functions of $\bar{u}\cdot\bar{g}$). Thus, if the goniometer stage had sufficient range and if the tilting of the foil did not obscure the image, it would be possible to obtain any of the image types in Fig. 19a from any loop. This last statement is not entirely true, because at any beam direction only a few diffracting vectors are available and not all of these are experimentally useful. Table 1 lists the six beam directions, along with the diffracting vectors at those directions, use in the fcc catalog. Table 2 lists similar data for the bcc catalog.

Each page of the catalogs contains the images of all defects calculated for one diffracting vector and one beam direction. This was done because a single micrograph could conceivably contain an image of all the possible defect types and permutations, but is imaged by only one beam direction and diffracting vector. If a loop type is contained in the catalog, all permutations of that type are

Table 1. fcc Catalog data - Aluminum (a_o = 0.404 nm)

Elastic Constants	Loop Normal	Burgers vector
$C_{11} = 11.83 \times 10^{10}$ Pa	(111)	$a_o/3[111]$
$C_{12} = 6.12 \times 10^{10}$ Pa	(111)	$a_o/2[110]$
$C_{44} = 2.85 \times 10^{10}$ Pa	(110)	$a_o/2[110]$

Beam Direction	Diffracting Vector	ξ_g(nm)	η	A
001	200	67.3	0.10	0.07
	020			
	220	105.7	0.10	0.09
	2$\bar{2}$0			
011	1$\bar{1}$1	55.6	0.10	0.06
	11$\bar{1}$			
	200			
	02$\bar{2}$			
111	20$\bar{2}$			
	0$\bar{2}$2			
	2$\bar{2}$0			
013	200			
	1$\bar{3}$1	130.0	0.10	0.11
	13$\bar{1}$			
112	$\bar{1}\bar{1}$1			
	2$\bar{2}$0			
	3$\bar{1}\bar{1}$			
	$\bar{1}$3$\bar{1}$			
123	$\bar{1}\bar{1}$1			
	3$\bar{3}$1	187.7	0.10	0.10
	4$\bar{2}$0	194.3	0.10	0.10

Table 2. bcc Catalog data - Tungsten (a_o = 0.315 nm)

Elastic Constants	Loop Normal	Burgers vector
C_{11} = 52.10 × 10^{10} Pa	(011)	$a_o/2[011]$
C_{12} = 20.10 × 10^{10} Pa	(011)	$a_o/2[111]$
C_{44} = 16.00 × 10^{10} Pa	(011)	$a_o[001]$
	(111)	$a_o/2[111]$

Beam Direction	Diffracting Vector	ξ_g (nm)	n	$\mathcal{A}$
001	$1\bar{1}0$	37.7	0.10	0.06
	$\bar{1}10$			
	200	52.0	0.10	0.09
	020			
011	$01\bar{1}$			
	200			
	$2\bar{1}1$	63.7	0.10	0.10
	$21\bar{1}$			
111	$10\bar{1}$			
	$01\bar{1}$			
	$\bar{1}10$			
013	200			
	$03\bar{1}$	85.4	0.10	0.14
	$23\bar{1}$	107.2	0.10	0.17
	$2\bar{3}1$			
112	$1\bar{1}0$			
	$22\bar{2}$	96.3	0.10	0.16
	$31\bar{2}$			
	$13\bar{2}$			
123	$1\bar{2}1$			
	301			
	$22\bar{2}$			

contained. So, for fcc loops with habits of (111) and burgers vectors of $a_o/2[110]$, the 12 unique permutations are presented. The arrangement of the defect images is identical on all pages. Figure 26 is a page from the fcc catalog given as an example. Table 3 gives the loop normals and burgers vectors to label the images. Because of the predominance of the habit plane in determining the characteristics of these infinitesimal loop images, images for loops possessing the same habit plane are arranged in rows, the first image of each row being an unsheared loop and those which follow possessing one of the expected shear burgers vectors. Displaced to the right is an array of images whose habits are of a different type than the main array. Tables 1 and 2 also give the defect types contained in the fcc and bcc catalogs.

Given below are the values of other parameters used in calculating the catalog images. The value of w, having only a small effect, was set to zero. Whether the black-white direction is acute or obtuse with the diffracting vector depends on the interstitial or vacancy nature of the defect, the defect depth, the foil's thickness and whether the image is bright or dark field. The catalogs contain bright field images of interstitial type defects so variations in depth can be accounted for by comparing to the defect depth series (Fig. 17). The contrast of vacancy type defects can be surmised by simply inverting the contrast. The defect depth is placed at 0.5 (centered in L-layer 2). The thickness was chosen to be 4.0 ξ_g for the fcc catalog and 3.5 ξ_g for the

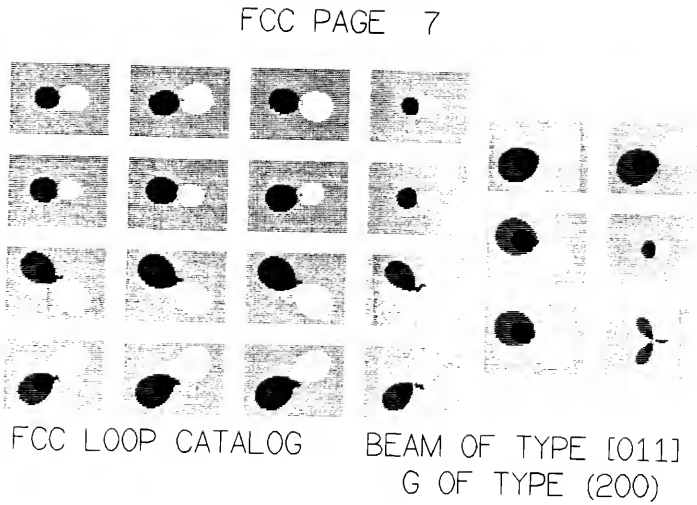

Fig. 26. Page 7 of the fcc Catalog.

Table 3. Loop normals and burgers vectors for the images on fcc catalog pages.

(loop normal)	(burgers vector)
111 111	111 110
111 101	111 011
	110 110
$\bar{1}01$ $\bar{1}01$	$\bar{1}11$ $\bar{1}11$
$\bar{1}11$ $\bar{1}10$	$\bar{1}11$ $\bar{1}01$
$\bar{1}11$ 011	$\bar{1}10$ $\bar{1}10$
011 011	$1\bar{1}1$ $1\bar{1}1$
$1\bar{1}1$ $1\bar{1}0$	$1\bar{1}1$ 101
$1\bar{1}1$ $0\bar{1}1$	101 101
$0\bar{1}1$ $0\bar{1}1$	$\bar{1}\bar{1}1$ $\bar{1}\bar{1}1$
$\bar{1}\bar{1}1$ $\bar{1}\bar{1}0$	$\bar{1}\bar{1}1$ $\bar{1}01$
$\bar{1}\bar{1}1$ $0\bar{1}1$	

bcc catalog. The foil normal was always set parallel to the beam direction so foil tilt would not be convoluted with other effects. Other parameters, such as the elastic constants, were chosen to be consistent with the materials assumed: aluminum is the fcc material and tungsten is the bcc material. These parameters are listed in Tables 1 and 2.

The uses of the catalogs for defect identification are now illustrated. Consider the image of the dislocation loop in aluminum circled in Fig. 27a. The diffracting conditions for this micrograph have been assigned $\bar{Z}$ = [011], $\bar{g}$ = (200). The appropriate fcc catalog page for $\bar{Z}$ = [011] and $\bar{g}$ = (200) is page 7 (presented as Fig. 26). Aligning the diffracting vector drawn on the micrograph so that the orientation corresponds to the diffracting vector of the calculated images in the catalog (i.e., to the right), the circled image in Fig. 27 matches the third row and also two other images at the lower left in the smaller array of images. The corresponding indices for the loop normals and the burgers vectors are found in Table 3:

$\bar{n}$	$1\bar{1}1$	$1\bar{1}1$	$1\bar{1}1$	$1\bar{1}1$	$\bar{1}10$	101
$\bar{b}$	$1\bar{1}1$	$1\bar{1}0$	101	$0\bar{1}1$	$\bar{1}10$	101

This example of the catalog's use for defect identification a posteriori does not yield a conclusive identification and leads to another use of the catalog: selecting a priori the diffracting conditions which will yield the most useful and discriminating images. The conclusion of such an exercise (carried out in the work of

Fig. 27. Dislocation loops observed in electron irradiated (200 keV) pure aluminum (99.9999%). (a) $\bar{z}$ = [011], $\bar{g}$ = (200) and magnification is 250,000. (b) $\bar{z}$ = [112], $\bar{g}$ = (2$\bar{2}$0) and magnification is 2,000,000.

Sykes et al., 1981, but not repeated here for lack of the complete catalogs) is that conclusive identification of an image is possible only for a defect viewed on edge. Two important imaging conditions are possible for this particular geometry. First, the diffracting vector may align with the major components of the defect's displacement field (i.e., with the burgers vector). In this case, the magnitude of the burgers vector can be estimated since, as pointed out by Eyre et al. (1977a,b) and Katerbau (1976), a reversal in contrast will occur near the center of the image for $|\bar{g}\cdot\bar{b}| > 1$. Holmes et al. (1979) point out that for loops viewed on edge, the interface between the black and white lobe is along the loop habit plane.

The butterfly image can be obtained from defects viewed on edge by using a diffracting vector perpendicular to the loop habit plane; i.e., $|\bar{g}\cdot\bar{b}| = 0$. This image gives the greatest sensitivity to the orientation of the loop as already noted. The insert of Fig. 27 is such an image and Fig. 28 is the fcc catalog page calculated for the corresponding beam and $\bar{g}$. The labels in Table 3 are also applicable to these images and from these it is apparent that the defect in Fig. 27b lies on $(\bar{1}\bar{1}1)$. Note in Fig. 28 that this image is the only image that discriminates between a Frank loop and its sheared counterpart. The catalog provides at a glance the imaging conditions which will yield this discriminating image. For example, if a bcc sample with an (001) foil normal is to be examined, a brief study of the bcc catalog (page 1, row 4; presented here as Fig.

29) demonstrates the ability of the (110) diffracting vector to distinguish between the burgers vector $a_o/2[111]$ and $a_o[001]$ for loops with a (011) habit.

The preferred method of identification is presented in Fig. 30. The same defect is imaged at the beam direction [001], $\bar{g}$ = (220), (200) and ($\bar{2}$20). Comparison with the fcc catalog shows this to be a loop with $\bar{n}$ = (110), $\bar{b}$ = $a_o/2[110]$. This defect is thus being viewed on edge at this beam direction. Note the structure between the black and white lobes in Fig. 30a, for which $|\bar{g}\cdot\bar{b}| = 2$. These data use a beam direction near the sample's foil normal. Although post-experimental use of the computer program can make use of the data taken from large tilts, the effort required to simulate a significant number of defects can be more profitably applied to collecting data from other areas of the sample. The catalogs will quickly indicate which diffracting vectors are most useful for the beam direction nearest the foil normal. From such data a number of images will be obtained which allow a confident identification as in Fig. 27b. The catalogs are not intended to be the final word on small defect identification, and further calculations using a finite strain field solution may be needed for conclusive identification of a defect. The catalogs do not resolve the problem of determining the interstitial or vacancy nature of a defect without precise data from stereomicroscopy.

Computer simulations were used to examine the effect of various imaging parameters. These studies extend the

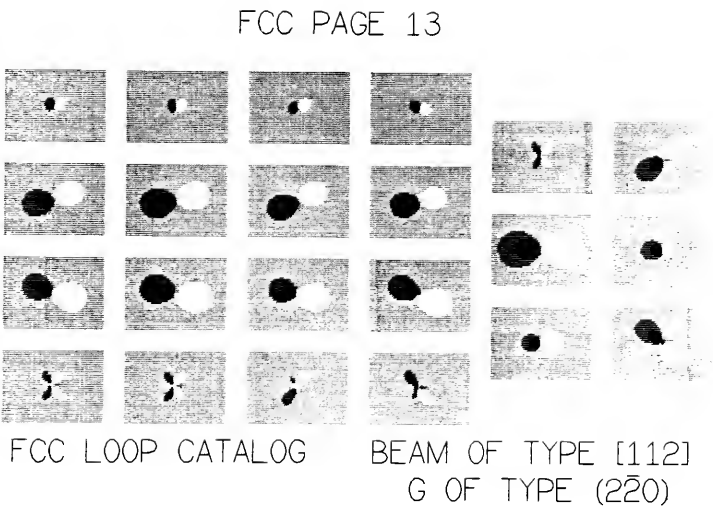

Fig. 23. Page 13 of the fcc Catalog.

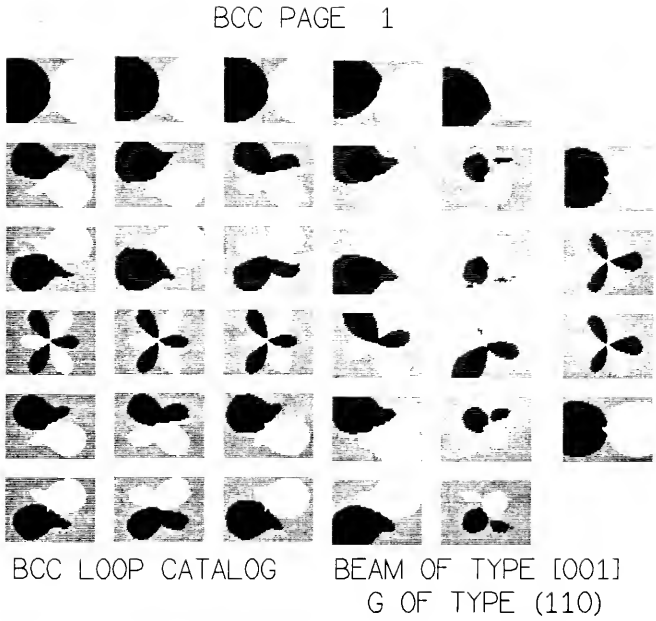

Fig. 29. Page 1 of the bcc Catalog.

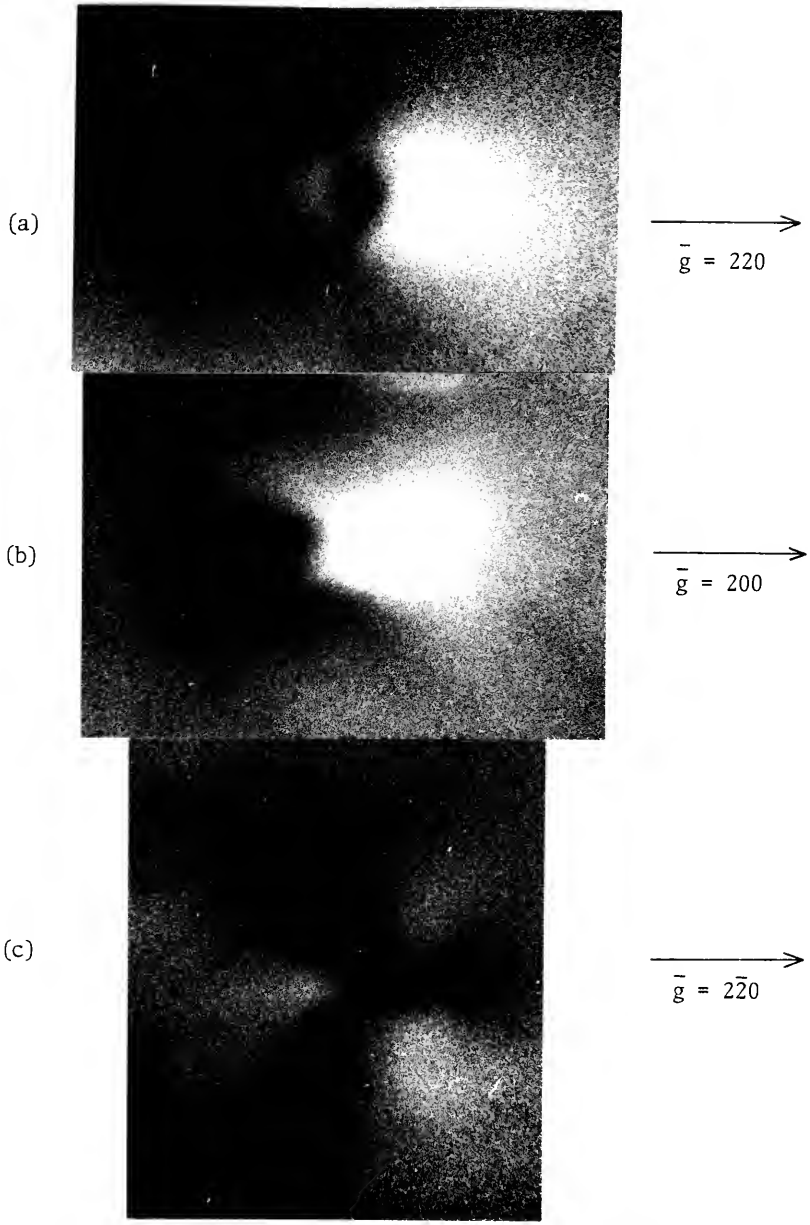

Fig. 30. Three images of a dislocation loop in neutron irradiated aluminum containing 200 ppma Si. All magnifications are 1,500,000.

understanding of small defect images, and determine the structure and parameters of the fcc and bcc catalogs. These catalogs provide an easy means of post-experiment identification of small loop images, but more importantly, they allow a priori determination of the best experimental conditions and procedures.

CHAPTER V
APPLICATION OF THE CATALOGS TO RADIATION DAMAGE IN ALUMINUM
BACKGROUND AND REVIEW

The theory and results in the previous chapters were applied in an investigation of several irradiated aluminum alloys. Such a study would not only produce information and data about the material itself but also demonstrate in what ways the catalogs are useful. It may also allow determination of the limits of the technique. For example, is there any evidence in the image of solute atoms clustering to a defect? Finally, knowledge gained in attempting an experiment establishes the limitations and difficulties which must be considered or addressed in any subsequent theoretical work.

Small defects can occur in rapidly quenched materials and materials exposed to radiation. Defects occuring from the latter mechanism are more technologically important. The behavior of materials in a reactor environment must at the very least be characterized. Preferably they should be well understood so their properties and performance can be optimized. The radiation induced damage in metals includes not only dislocation loops but also voids and often precipitates. Alloy additions can greatly change the radiation damage behavior of metals so, the interaction

of solute atoms with defects is expected. The study of such a system is well suited to the goals of this research.

The effect of radiation on metals has been of scientific interest for some time but this field gained great technological importance when Cawthorne and Fulton (1967) reported the phenomenon of void swelling in neutron irradiated stainless steel. Void swelling greatly affects the design of fast reactors and fusion reactors. Huebotter and Bump (1972) have reviewed some of the implications of void swelling on reactor design. The basic processes and theories of the radiation damage of metals will be briefly reviewed here to provide a perspective from which previous and present work can be appreciated. Mansur (1978) has reviewed the theories of radiation damage and void swelling and the following pages summarize the main points from his work.

The collision of an energetic particle with a metal sample creates damage in the form of an array of vacancies and interstitials. Diffusion of the vacancies and interstitials is required if they are to recombine and annihilate each other. At low temperatures vacancies are essentially immobile and are annihilated by interstitials, still migrating due to their low binding energy. At higher temperatures ($> 0.3T_m$), the vacancies are mobile and can cluster together. These clusters become voids while the interstitials migrate to dislocations. The point defects can also migrate to be absorbed into various defects such as voids, plates, dislocation loops, etc. If interstitials are

preferentially absorbed to dislocations and are repelled by voids, there will be a net flux of vacancies to the voids resulting in their growth and macroscopic swelling.

The amount of immediate damage created by a colliding particle depends on the material of the target and the energy and mass of the particle. An incident particle of mass M_1 and energy E can have a maximum transfered energy E_m to the target of (Wilkens,1970):

$$E_m = 4EM_1M_2/(M_1 + M_2)$$

where M_2 is the mass of the target atoms. For $E_m > 20$ eV a Frenkel pair is created. For $E_m > 1$ to 10 keV, a cascade of damage is created. In the array of damage resulting from the collision of a massive energetic particle (the cascade), the vacancies are found nearer the collision site while the interstitials are found further out. Another immediate effect of a collision is a possible nuclear reaction resulting in the transmutation of a target atom. Although alloys can be made more resistant to the results of displacement damage, nothing can be done about this latter effect. Most metals, however, have small cross sections for transmutation.

Many of the point defect pairs created in a collison event are unstable and immediately recombine and annihilate eachother. Of the stable point defects many will recombine after diffusing a short distance. Those which survive to diffuse away from the cascade produce the effective point defect generation rates, G_i and G_v, where i and v refer to interstitials and vacancies respectively. Within the bulk,

the point defects can be lost by recombination with an opposite point defect, by absorption into various crystal defects or by loss to a free surface. By accounting for the production and the loss of point defects, the change in their concentrations can be expressed

$$dC_p/dt = G_p - RC_vC_i - K_pC_p + \nabla(D_p\nabla C_p + D_pC_p\nabla U_p/kT)$$

where C is the point defect concentration, G is the point defect production rate, R is the recombination constant, K is the reaction rate constant for losses to sinks, U is the interaction energy with a discrete sink, and D is the diffusion coefficient. The subscripts i and v refer to interstitials and vacancies, respectively. The subscript p is replaced by i or v, depending on whether the equation is to apply to interstitial or vacancy concentrations. The last term on the right represents losses to a surface and will be ignored. This equation and those which follow model the material as a homogeneous continuum whose properties are the same on the average as the real material. In the material there are sinks of type j and of strength S_p^j. After the initial build up time at the start of the irradiation, the point defect concentrations reach a quasi steady state and so the time derivative can be considered zero. This allows the above equations to be solved for the point defect concentrations as a function of the sink microstructure:

$$C_i = \frac{[K_iK_v + R(G_i + G_v)]}{2RK_v}\{[1 + \frac{4RG_vK_iK_v}{[K_iK_v + R(G_i + G_v)]^2}]^{-1/2} -]\}$$

By using this equation iteratively to determine the point defect concentrations and using other equations which give the defect growth rates as a function of the point defect concentration, the evolution of the radiation damage microstructure can be predicted. The generally observed course of microstructural evolution is the nucleation of small loops, the growth of the interstitial loops into a dislocation structure (tangles) and the nucleation and growth of voids. Depending on the alloy system, precipitation of a second phase may also occur.

This approach has been applied to the growth of voids (Mansur, 1978). The growth of a void of size r^v will depend on the arrival rates of interstitials and vacancies to the void:

$$dr^v/dt = \Omega\{Z_v^v(r^v)D_v(C_v - C_v^e(r^v)) - Z_i^v(r^v)C_i D_i\}/r^v$$

where Ω is the atomic volume, C_v^e is the thermal vacancy concentration at a void of radius r^v, and Z_p^v is the sink (void) capture efficiency. Inserting the equation for the point defect concentrations and replacing the populations of defects of various sizes with populations of defects of an appropriate average size ($\bar{r}^v$ in the case of voids), leads to:

$$\frac{d\bar{r}^v}{dt} = \frac{D_i D_v \Omega}{2R\bar{r}^v}\left[\left(1 + \frac{4GR}{K_i K_v}\right)^{1/2} - 1\right]\times\{\Sigma_j \phi^j (Z_i^j Z_v^v - Z_v^j Z_i^v)\}$$

where ϕ^j is a weighting factor accounting for the average size and number of sinks of type j. The terms of the type $(Z_i^j Z_v^v - Z_v^j Z_i^v)$ are defined as the bias of the sink type j with respect to voids. This is the basic quantity

determining the potential of the material to swell. It is interesting to note that the existence of at least one other sink type is a prerequisite to the growth of voids. If the interstitials have no other place to go, they must ultimately be migrating to the voids in a one to one ratio with the vacancies. If only one other sink type is present, say dislocations, then if voids are to grow, this sink must have a greater tendency to absorb interstitials versus vacancies than voids do; that is $Z_i^d/Z_v^d > Z_i^v/Z_v^v$. Besides influencing the important bias term, the other sinks can effect void growth by the term $K_i K_v$ in the denominator of the above equation. If the total sink reaction rate constants are high the point defect concentrations will be kept low, slowing the growth of the voids.

Because of their importance in determining the void growth rate, the efficiencies Z_p^j deserve more consideration. These terms are obviously related to the structure of the sink and it is not surprising that it is difficult to estimate their values. The definition of the efficiency of a void is given to clarify its meaning. The concentration profile around a void is:

$$C(\rho) = C^\infty - (C^\infty - C')(r^\infty/\rho - 1)/(r^\infty - r^v)$$

where r^v is the void radius, ρ is the distance to the void center, r^∞ is the distance at which $C = C^\infty$, and C' is the concentration at the void surface. The loss of point defects to the void, k^v, is the flux at the surface times the void area

$$k^v = 4\pi r^2 D(dC/d\rho)\Big|_{\rho=r^v} = 4\pi r^v D(C^\infty - C')(1 - r^v/r^\infty)^{-1}$$

If we let $Z^V(C^\infty - C^e(r^V)) = (C^\infty - C')$, then this becomes

$$k^V = 4\pi r^2 D(C^\infty - C^e(r^V))Z^V(1 - r^V/r^\infty)^{-1}$$

If the void is a good absorber, $C' = C^e(r^V)$ and $Z^V \cong 1$. If the void is a poor absorber, $C^\infty < C' < C^e(r^V)$ and $0 < Z^V < 1$. The sink capture efficiency Z expresses the relative ability of the real sink to absorb point defects to that of a perfect absorber (i.e., a sink which freely absorbs all defects which drift to it and so maintains the local concentration at the equilibrium value). Of course, for any defect of type j, Z_p^j is as poorly known as the C around the defect. Of greatest importance, however, is the comparative values of the sink efficiencies, which are expressed as the bias terms, $(Z_i^j Z_v^V - Z_v^j Z_i^V)$. Small changes in efficiencies can produce relatively large changes in the bias. Although quantitative predictions are difficult, it is only necessary to estimate whether a give structural change increases or decreases the efficiency of a defect to estimate the change in the swelling behavior.

Estimates and calculations of sink strengths and bias factors have been carried out for some defects. Wolfer and Mansur (1976) derived the interaction of a point defect with a spherical cavity and later used this result in numerical calculations of void capture efficiencies (Mansur and Wolfer, 1978). They showed that the presense of an impurity coating at the surface of a void could reverse the bias of a void from preferentially absorbing interstitials to preferentially absorbing vacancies. Coghlan and Yoo (1977) have calculated Z for a finite dislocation loop. Wolfer and

Ashkin (1975) have derived expressions for the bias of a general spherical strain center and calculated its effect on point defect fluxes.

Control of alloy composition is one of the most important methods by which a metallugist influences the properties of a metal. Impurity atoms can affect all the processes described above. The effective yield of point defects per collision can be changed. The impurity atoms disrupt the perfection of the lattice and this will lessen the ability of the interstitials to be transported as far away from the center of the cascade as in the pure material. More point defects will recombine immediately and reduce the effective yield. The impurity atoms are usually of a different size than the matrix atoms. Vacancies are more stable if configured next to a larger atom; interstitials are more stable next to a smaller atom. The point defects can thus be coupled or bound to an impurity atom. The point defect/impurity atom complex may migrate together or the point defect may simply be held up at the impurity. Both these mechanisms result in a decrease in the effective diffusion coefficient of the total point defect population. Not only will this slow the rate at which vacancies arrive at voids but by being held in the matrix longer, there is a greater probability of annihilation by meeting an opposite point defect. It can be shown (Mansur, 1978) that these processes can be handled in the above theory and equations by changing the point defect diffusion coefficients to lower effective values. The magnitude of this mechanism will be

different for vacancies than for interstitials since the energy binding vacancies to a particular solute species will be different than the energy binding interstitials. Numerical calculations for nickel (Mansur, 1978) show that a vacancy binding energy of 0.1 eV reduces swelling but for interstitial trapping to be effective the binding energy must be greater than the difference between the vacancy and interstitial migration energies, that is, about 1.2 eV.

Radiation affects the stability of second phase particles in an alloy. Depending on the conditions and the alloy system, radiation can enhance precipitation, induce precipitation in undersaturated alloys or induce solution of precipitates in supersaturated alloys. Martin (1978) has reviewed the systems displaying precipitation in undersaturated alloys. Several models have been proposed to explain this. Bocquet and Martin (1979) have taken a thermodynamic approach and considered a ternary phase diagram (a, b, point defect). Precipitation in undersaturated alloys is predicted under restrictive conditions not met by experimental systems displaying this phenomenon. Maydet and Russell (1977) formulate the precipitation or solution of a precipitate in terms of an irradiation modified free energy $\Delta\phi$ which depends on kinetic and thermodynamic factors such as solute and vacancy supersaturations, precipitate/matrix misfit and the degree of point defect biasing. They predict the possibility of the growth of oversized precipitates in an undersaturated

alloy and the dissolution of undersized precipitates in an oversaturated alloy.

The most favored model is that of Johnson and Lam (1976) which proposes the drag of solute to sinks. The coupling of solute atoms to point defects can result in the solute being dragged to the various sinks at which the supersaturated point defects condense. This raises the local solute concentration which, if exceeding the solubility limit, induces precipitation. If irradiation stops, ending the flux of solute to the sinks, the precipitates dissolve (provided the temperature is high enough to make this kinetically feasible). Even if the local concentrations do not reach the level required for precipitation, the solute atoms will alter the structure of the sink, thus altering the sink efficiency and so influencing the swelling behavior of this alloy. Mansur (1979) states that a solute atom can produce a greater effect by this mechanism than by trapping point defects in the matrix. This conceptually simple model is applicable to many but not all observed cases of radiation induced precipitation. Cauvin and Martin (1979) have observed homogeneous precipitation of GP zones and β precipitates in Al+2%Zn. The mechanism proposed to account for this is the coupling of point defect fluxes to solute concentration heterogeneities, a mechanism somewhat analogous to spinodal decomposition.

The alloy system chosen for study in the present work was included in a survey of the void swelling behavior of

aluminum alloys conducted by Farrell and Houston (1979). They prepared many dilute alloys (nominally 100 atomic parts per million of solute addition) and neutron irradiated them to four dose levels. The irradiated samples were then observed by TEM and the microstructures compared to that of irradiated pure aluminum, which swelled about 1% at the highest dose used. The elements Ag, Ca, Fe, In, Mg, Ni, Si, Sn and Zn had little affect on the damage behavior. The elements Cr, Cu, Mn, Ti, V and Zr retarded the formation of voids and dislocations. These latter elements reduced the number of voids rather than their average size, indicating an effect on their nucleation rather than their growth. Effective elements slowed the evolution of dislocation loops into a dislocation structure, simultaneously inhibiting void formation, but had little effect on void growth after the dislocation structure developed. Of these elements, Mn was the most effective and Cu reduced swelling if present in amounts as low as 25 ppma.

Precipitates were observed in many of the microstructures. Due to the high cross section aluminum has for neutrons, significant transmutation occurs by the reactions

$$^{27}Al(n,\gamma)\,^{28}Al$$

$$^{28}Al \rightarrow {}^{28}Si + \beta$$

and silicon precipitation occurs in neutron irradiated Al (Farrell et al., 1970). Silicon precipitates are therefore a feature common to all alloys at the highest dose. Extrapolation of solubility data indicates that most alloys

were supersaturated at the irradiation temperature (55C). Radiation assisted precipitation of the alloying element is expected and the presence of transmuted Si precipitates complicates interpretation of the microstrutures. Farrell states the precipitation is heterogeneous, remarking in addition that the precipitates in the highly irradiated Si and Cu alloys had the same concentration, size and spatial distribution as did the small dislocation loops seen at lower doses. In analyzing these results, Farrell and Houston noted that the best damage resistance was imparted by solute atoms with strong negative misfits (defined by the solutes effect on the lattice parameter of Al). Based on this they concluded that the primary damage suppression mechanism is solute/interstitial trapping by negative misfitting solute atoms.

As an extension of the above work, it was decided to use the catalogs to carry out a more detailed investigation of an alloy which proved important in Farrell and Houston's survey. The Al+100 ppma Cu alloy was chosen for further study both because low amounts of copper suppressed swelling and because the Al-Cu system is well known and characterized. Pure aluminum was also studied to provide a standard for comparison. It was likewise necessary to study an Al+100 ppma Si alloy to provide a standard of control for the transmutation phenomenon.

Clustering and precipitation phenomenon in the Al-Cu system have been examined in the famous work of Guinier (1938) and Preston (1938). Precipitation proceeds in the

stages

$$GP(1) \rightarrow \theta'' \rightarrow \theta' \rightarrow \theta$$

Several investigators have studied this system by the use of TEM. Nicholson and Nutting (1958) first observed black-white stain contrast around coherent precipitates in an Al+4%Cu alloy. Thomas and Whelan (1961) have used a heating stage to observe the precipitation sequence in situ. Philips (1973,1975) has used the technique of lattice fringe imaging to study the precipitation process from GP(1) zones to θ'.

The irradiation damage behavior of Al-Cu alloys has also been investigated. Katz et al. (1968) observed an enhancement of the rate of θ' nucleation for alloys neutron irradiated and subsequently aged below 235C. Sklad and Mitchell (1975) have done in situ electron irradiations of an Al+3.5%Cu alloy in a high voltage electron microscope. Enhanced θ' growth was observed in the temperature range 20-200C, but the intermediate θ'' stage appeared to be suppressed by the irradiation. Weaver et al. (1978) again noted the enhanced growth of θ' in an in situ HVEM study. They proposed an irradiation induced effective change in the metastable phase diagram. Voids were not reported in the above three studies. Carpenter and Ogle (1975) conducted neutron irradiations on two alloys, Al+1.7%Cu and Al+3.8%Cu, using various pre-irradiation heat treatments to produce starting structures composed of GP(1) zones and θ'', θ'', or θ'. They found minimum void swelling in the microstructure containing GP(1) zones and θ''. In later work, Carpenter and

Yoo (1978) studied the neutron irradiation behavior of an Al+4%Cu alloy aged to contain large semicoherent Θ' plates. A ten fold reduction in void swelling relative to pure aluminum was quantitatively accounted for by assuming traps for vacancies and interstitials in the Θ'/matrix interface. They also used EDX to detect the segregation of transmuted Si to this interface.

All of this previous work, both on irradiated and unirradiated alloys, has been done on fairly concentrated alloys (> 1%Cu). The work of Farrell and Houston and, of course, the present work was done on a very dilute alloy. At the temperature of irradiation, however, the solubility of Cu is extrapolated to be near 100 ppma (Farrell and Houston, 1979) and so radiation enhanced or induced precipitation may be expected.

CHAPTER VI
EXPERIMENTS AND RESULTS

The samples used in this research were irradiated, by Farrell and Houston (1979) in their work and were kindly made available by them. Their alloys contained nominally 100 ppma (parts per million, atomic fraction) of one of the following elements: Ag, Ca, Cr, Cu, Fe, In, Mn, Ni, Si, Sn, Ti, V, Zn and Zr. Farrell and Houston's description of the experimental proceedure is reproduced below:

> The cast ingots were homogenized for 1 week at 823K (0.88 T_m). They were cold rolled to 0.5 mm thickness and 3 mm diameter disks were punched. These disks were annealed for 1 hour at 673K (0.72 T_m) in air and were slowly cooled. They were then packed randomly in aluminum powder in sealed aluminum cans and were irradiated at an estimated temperature of 338-358K (0.37 T_m) in the High Flux Isotope Reactor (HFIR) at Oak Ridge. Four fluence levels were attained, 2×10^{22}, 2×10^{23}, 2×10^{24} and 2×10^{25} n/m^2 (> 0.1 MeV), corresponding to 2.6×10^{-3}, 2.6×10^{-2}, 0.26 and 2.6 dpa [displacements per atom]. The thermal-to-fast fluence ratio was 2.3, the thermal neutrons resulting in the formation of 10^{-6} to 10^{-3} atomic fraction Si, the major transmutation product.

The copper and silicon alloys used in the present research contained 100 ppma; Farrell and Houston actually used several different compositions of these alloys. It is also noted that the observations made in this research were made two years after the irradiation of the samples. Metastable damage and/or phases might no longer be present.

Previously thinned samples were no longer suitable for microscopy and samples were newly thinned for observation. Thinning proceeded in two stages. First the 0.50 mm thick disks (3 mm diam.) were dimpled on both sides by electropolishing to a thickness of 0.075 mm. The solution was 120 ml water, 100 ml ethylene glycol monobutyl ether, 78 ml perchloric acid (70%) and 700 ml ethanol. Polishing was driven by 125 mA of current at room temperature. The dimpled disks were then electropolished in a solution of 10 ml perchloric acid in 180 ml of ethanol at 0 to 10C using a current of 88 mA. The glassware for the polishing solution contained flat view ports to allow observation of the samples during polishing. The current was stopped and the sample quickly removed when a small hole first appeared in the sample.

The samples were observed in either a JEOL 100CX electron microscope or a Philips 400 electron microscope equipped with a field emission gun. The imaging conditions were chosen to be consistent with the fcc catalog. The deviation from the Bragg condition was set at or close to zero for most micrographs, although larger values also proved useful. Samples irradiated to the two lowest doses displayed no particular damage microstructure. They contained some dislocations as are usually found in an annealed sample. In some areas a few small defects could be seen. A great number of small defects were found in the Al-Cu and the Al-Si samples irradiated to the highest dose. At this dose 1000 ppma of transmuted Si is expected.

Diffraction spots from elemental Si were found in diffraction patterns taken from these samples and it was concluded that the defects were precipitates of elemental silicon. Figure 31 displays microstructures from these alloys. They appear quite similar in terms of precipitate and void density.

The samples irradiated to the third dose (0.26 dpa) proved to be the most interesting and these were studied in greater detail. At this dose, all samples will have about 100 ppma Si added to their composition by the tranmsmutation of Al. To avoid confusion, this fact will not be explicitly mentioned in describing the alloys and they will be refered to simply as the pure aluminum alloy, the Al+100 ppma Si alloy and the Al+100 ppma Cu alloy. The pure aluminum sample (Fig. 32) displayed a low density of defects. Figure 32 clearly shows the presence of voids. Precipitates are observed in three morphologies: roughly spherical (or disklike), a right triangular plate, and a rod-like plate. Also occasionally observed were small plates exhibiting a moiré fringe spacing of $\sim$4.5 nm. For g = (200) in aluminum, this means the plate has a lattice spacing of 0.1933 nm or 0.2094 nm parallel to the aluminum (100) planes. This defect type also appears in the other alloys.

The microstructure of the Al+100 ppma Si alloy exposed to the third dose is shown in Fig. 33. The precipitate morphologies are similar to the pure aluminum sample but the density is much greater. Only a few of the defects exhibit significant strain contrast. Voids were not observed in

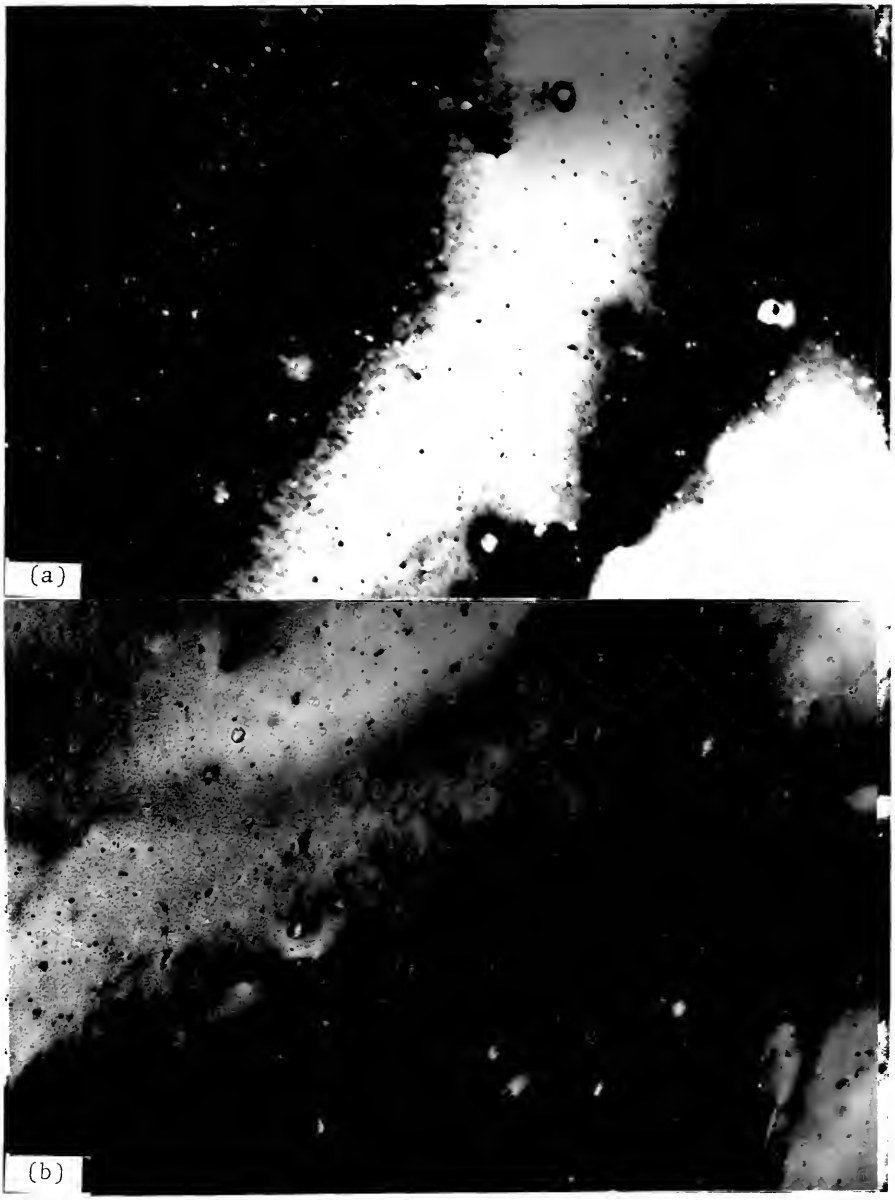

Fig. 31. Microstructures of (a) the Al+100 ppma Si and (b) the Al+100 ppma Cu alloys irradiated to the fourth neutron dose of 2×10^{25} n/m^2 (2.6 dpa). Magnifications are both 70,000.

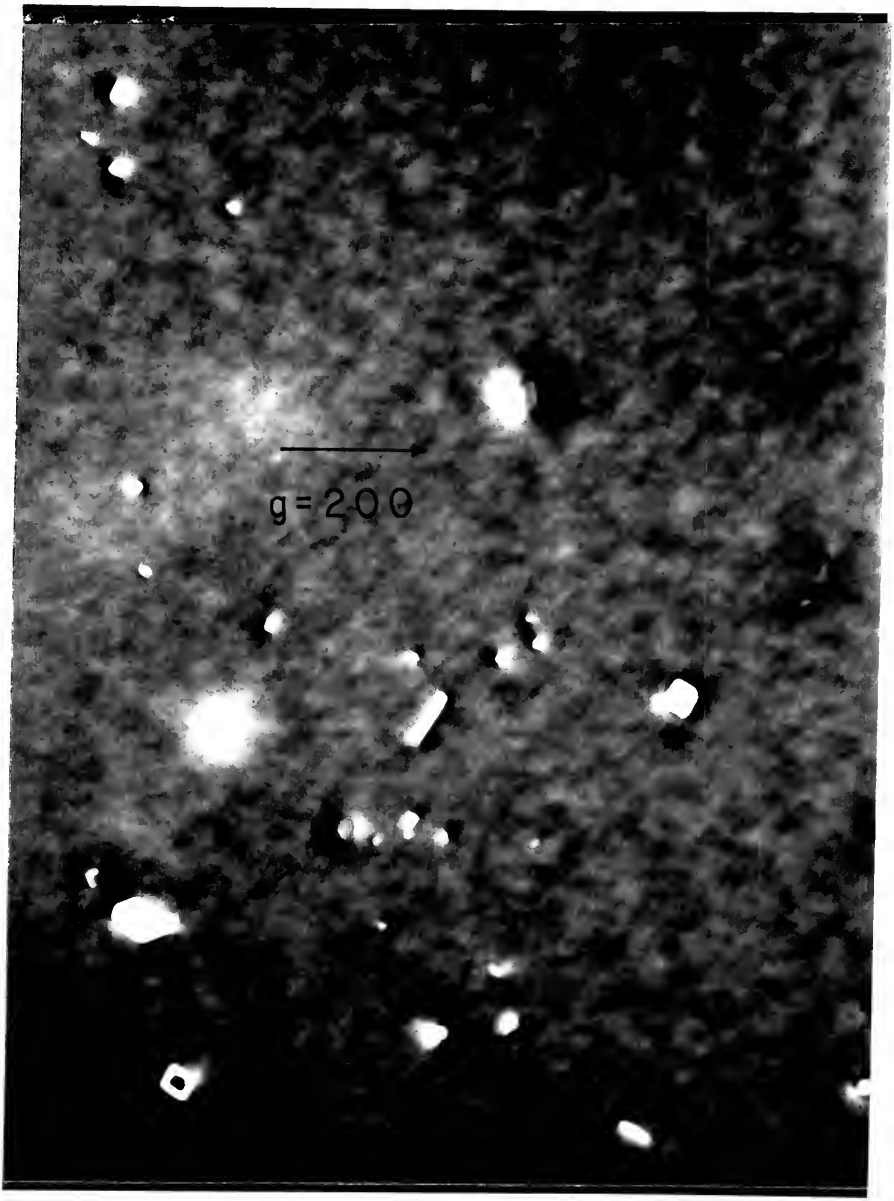

Fig. 32. Microstructure of the pure aluminum sample irradiated to the third neutron dose of 2×10^{24} n/m^2 (0.26 dpa). Magnification is 250,000.

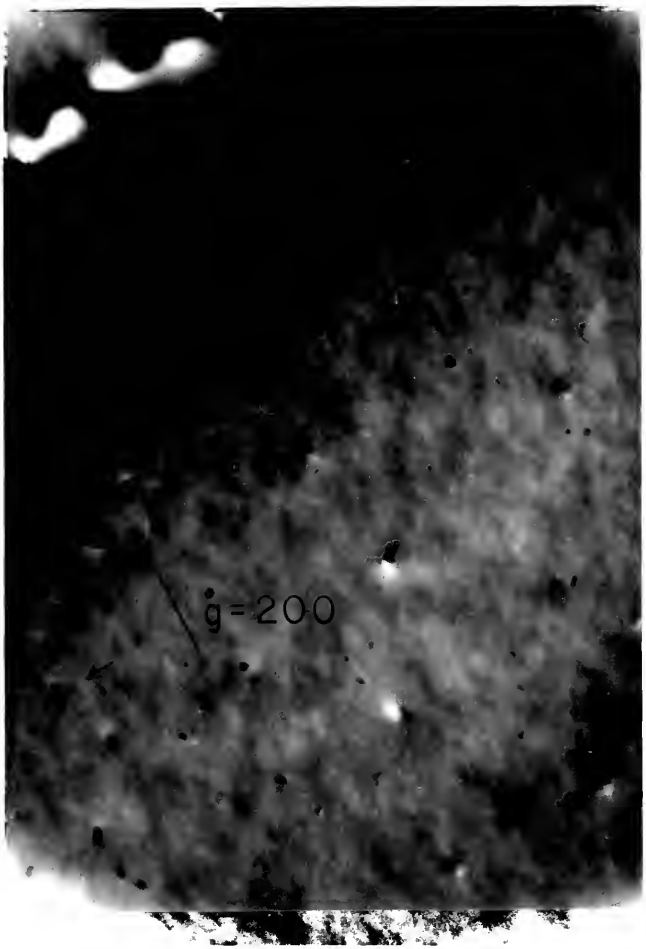

Fig. 33. Microstructure of the Al+100 ppma Si alloy irradiated to the third neutron dose of 2×10^{24} n/m^2 (0.26 dpa). Magnification is 200,000.

this sample. In Fig. 33 there is one plate precipitate exhibiting a 4.5 nm moiré fringe spacing.

The Al+100 ppma Cu alloy is shown in Fig. 34. The defect density is comparable to the Al+100 ppma Si alloy but almost all the defects (plates on (100)) exhibit strong strain contrast. Using a diffraction vector perpendicular to the plate normal (Fig. 35), the plates exhibit an image of butterfly symmetry as expected, but the details of the image are not as predicted by the computer calculations for a Frank loop. This will be discussed at greater length later but the results of the analysis add great support to the conclusion that these precipitates are Θ'. A plate exhibiting the kinematic moiré fringe spacing of 4.5 nm is seen in Fig. 36. The number of such defects was the greatest in the Al+100 ppma Cu alloy. No voids were observed in this alloy at this dose. Another significant feature of this alloy was the presence of large dislocation loops (see Fig. 37). These were found only in the thicker regions of the foils and so presumably they either slipped out of the foils in thinner regions or were cut by the surfaces and so appeared as straight dislocations. From geometry, the habit planes were determined to be (110), thus having a burgers vector of $a_o/2[110]$, and by the inside/outside contrast method of Edmondson and Williamson (1964) they were determined to be interstitial loops. A search of even the thickest regions of the pure aluminum and Al+100 ppma Si samples failed to reveal any large dislocation loops.

Fig. 34. Microstructrue of the Al+100 ppm Cu alloy irradiated to the third neutron dose of 2×10^{24} n/m^2 (0.25 dpa). Magnification is 200,000.

Fig. 35. Same area as Fig. 33 imaged using the diffracting vector $02\bar{2}$ which yields $|\bar{g}\cdot\bar{b}| = 0$ for many of the defect images. Insert magnifies the circled image. Magnifications are 200,000 and 2,000,000.

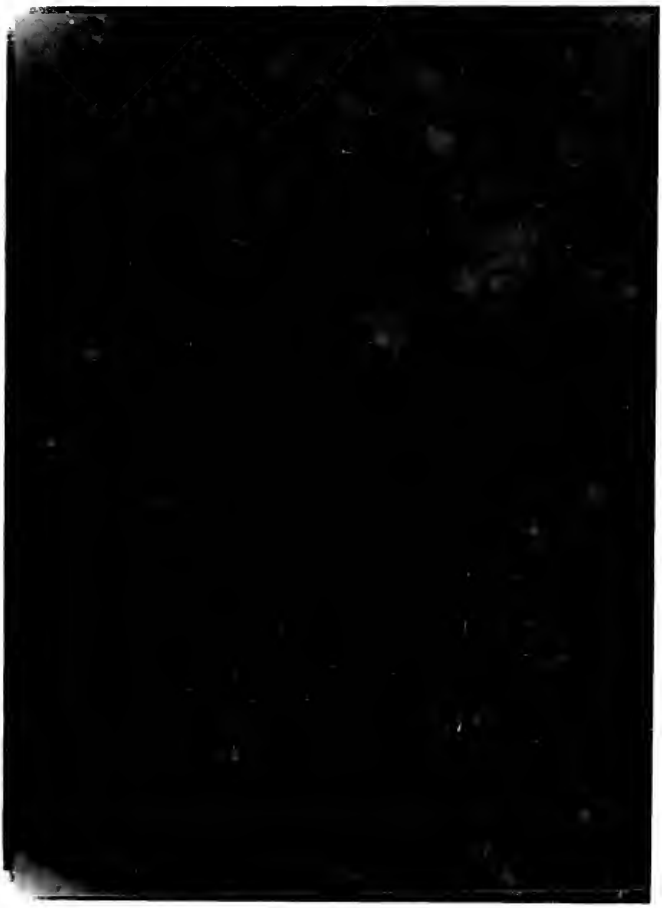

Fig. 36. A kinematic image of the same area as in Fig. 33 and Fig. 34. Magnification is 200,000.

Fig. 37. Large dislocation loops observed in the thicker regions of the Al+100 ppma Cu sample (third dose). Analysis determined that these are interstitial loops of type $\bar{n}$ = (011), $\bar{b}$ = $a_o/2[0111]$. Magnification is 17,000.

Figure 38 is presented because of this work's interest in the details of small defect images. This shows the black-white images of the precipitates in the Al+100 ppma Cu sample, imaged by the use of $\bar{g}$ = (200). In some of these images is seen structure similar to that predicted for the case $|\bar{g}\cdot\bar{b}| > 1$. The white area in the black lobe, however, is not complimented by a black area in the white lobe. This structure is very dependent on s and is suspected to be the psuedo-interface structure predicted by Eyre et al. (1977) for a defect in the boundary between L-layers. Because of the possibility of misinterpreting this structure, more theoretical work should be done to determine the conditions for which it can occur.

Table 4 summarizes the microstructures, giving estimates for the number density and/or the volume fraction of the various defects found in the three alloys. There is great uncertainty in these values because the foil thickness and the average particle size is difficult to determine. The absolute magnification is known to $\pm$10% and this error is cubed in these estimates. The estimates of volume fraction cannot be trusted to better than a factor of two. Nevertheless, the value for the void volume fraction for the pure aluminum sample is in good agreement with Farrell and Houston (1979). They report 1% swelling at the forth dose which would yield 0.1% at the third dose, assuming a linear dependence on dose. The values in table 4 listed as "Maximum Theoretical V_V of Precipitate" are the volume fraction expected from the complete precipitation of the

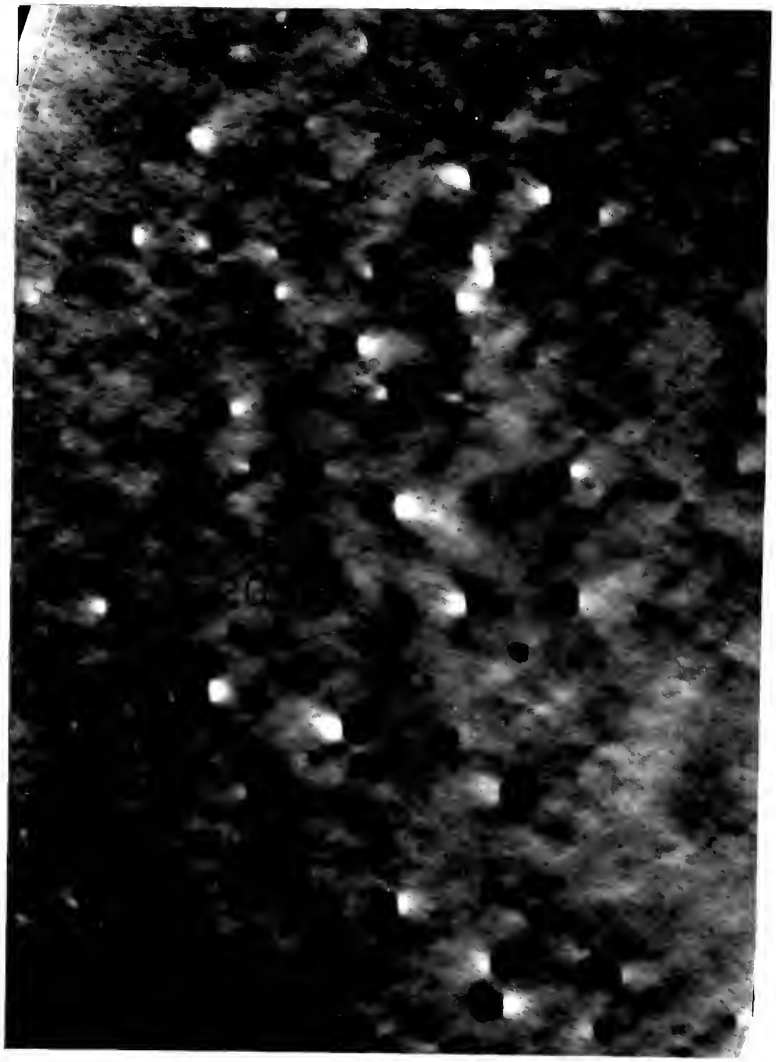

Fig. 38. Black-white images of precipitates in the Al+100 ppma Cu sample. Note many images show a reversal in contrast near the black-white interface. See text for discussion of this pseudo-interface structure. Magnification is 250,000.

Table 4. Microstructural Summary of Alloys Irradiated to a Dose of 2×10^{24} n/m^2

	Pure Aluminum	Al+100 ppma Si	Al+100 ppma Cu
V_V of Voids	1000 ppmv (0.1%)	none seen	none seen
N_V of Precipitates	0.1×10^{15} cm^{-3}	1.4×10^{15} cm^{-3}	2.7×10^{15} cm^{-3}
V_V of Precipitates	5 ppmv	136 ppmv	276 ppmv
Theoretical Maximum V_V of precipitate	121 ppmv as Si	242 ppmv as Si	121 ppmv as Si 290 ppmv as θ'
Dislocation Density	-	-	27×10^{8} cm^{-2}
Comments	Large precipitates seen on most voids	No voids seen	No voids seen
	Precipitates are in the form of disks, triangular plates, and rodlike plates	Precipitates are mostly disks; some triangular plates; some rods	Precipitates are θ'
	Few morié fringed precipitates	Few morié fringed precipitates	Many morié fringed precipitates
	Low dislocation density	Low dislocation density	20% of dislocations were in the form of large loops

solute elements (100 ppma Si, 200 ppma Si, and 100 ppma Cu plus 100 ppma Si) assuming zero solubility. The silicon in the Al+100 ppma Cu sample may be partially incorporated in the θ' or, if present as Si precipitates, is too difficult to distinguish from the θ' to allow separate determination of the Si precipitate volume fraction. The copper is assumed to precipitate as θ'. The theoretical and experimental values are in reasonable agreement, considering the uncertainty involved, except for the Si in the pure aluminum and the Al+100 ppma Cu samples. For the pure aluminum sample, a 1.0 nm thick Si coating on the voids of size and number seen can account for 60 ppma Si. Also the voids appear associated with large precipitates whose volume is ignored in the estimate of V_V. It was qualitatively obvious that the moiré fringed precipitates were most abundant in the Al+100 ppma Cu alloy. Because they also occur in the pure aluminum and Al+100 ppma Si samples, it is concluded that these are a form of Si precipitate. The presence of Cu in the aluminum apparently makes this a more preferred morphology for Si precipitation.

On the whole these observations are consistent with those of Farrell and Houston (1979). As here, they report little damage at the two lowest doses. Their statement that precipitates at the fourth dose appear on the same distribution as earlier loops may reflect their mistaking the θ' images (as in Fig. 34) for dislocation loops. They report a dislocation structure always accompanied the presence of voids, but here no particular structure was seen

in the pure aluminum sample (third dose), which contained voids. If dislocation loops were initially present in this sample, they may have slipped out of the foil before the present observations were made. Copper alloying makes glide more difficult and so the loops remained to be seen in the Al+100 ppma Cu alloy.

Another experiment carried out was the electron irradiation of these alloys. Such an experiment, being done in situ, can demonstrate kinetic differences in the alloys. The experimental proceedure was quite simple. Samples of the unirradiated alloys were thinned as described above to electron transparency. They were then observed in a JEOL 200CX electron microscope. This microscope is equipped with a variable accelerating voltage, ranging to a maximum of 200 kV. Two hundred keV electrons have sufficient energy to create displacement damage in aluminum in the form of Frenkel pairs. The samples were observed using a voltage of 120 kV (which is below the damage threshold) and a suitable area was micrographed to document the initial lack of defects. The accelerating voltage was then raised to 200 kV and the condenser lenses of the microscope adjusted to concentrate the electron beam on a small area ($\sim$1 μm). Irradiation proceeded until damage was visible using the binoculars of the microscope. The beam was then decondensed and the accelerating voltage reduced to 120 kV for imaging and micrographing the damage. Figure 39 shows the resulting damage of the three alloys. The variation in the irradiation time must be kept in mind: 4 to 5 minutes for

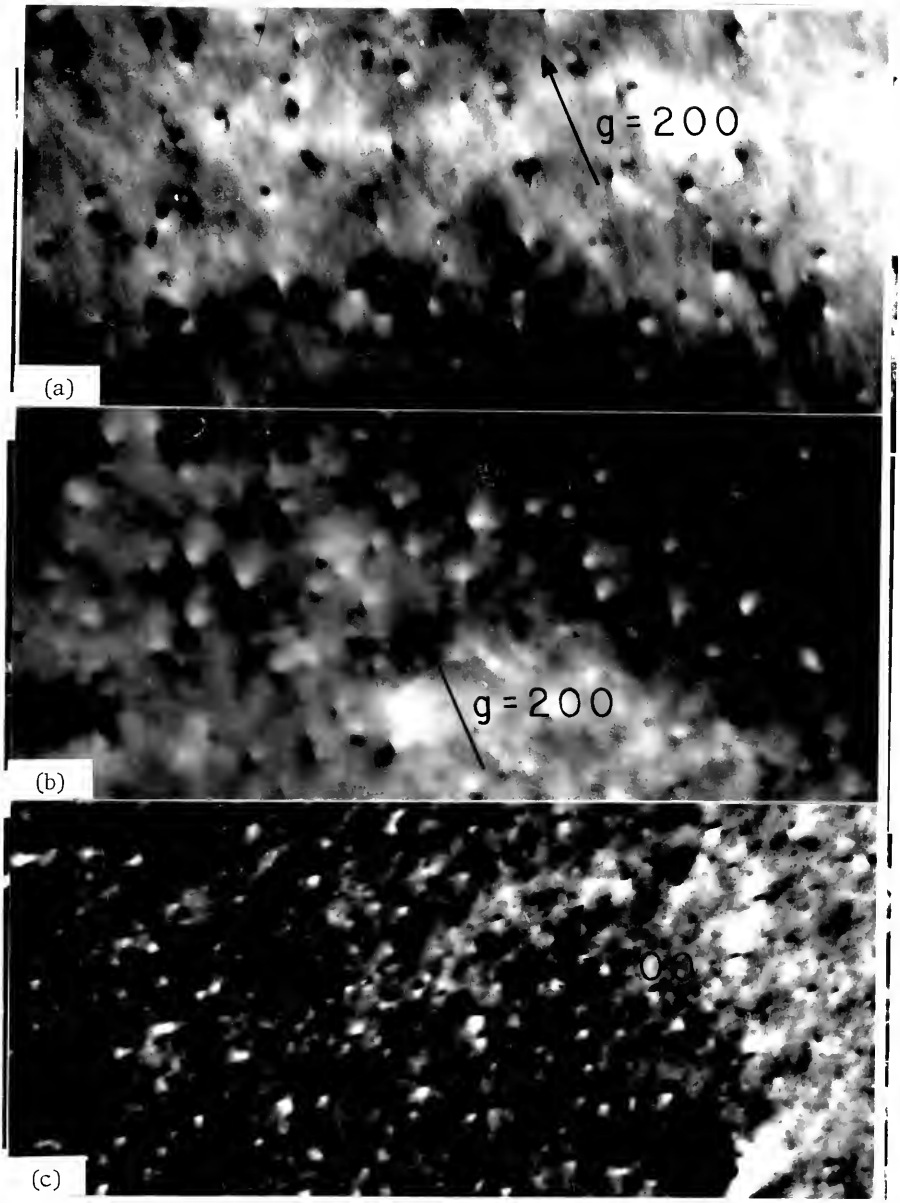

Fig. 39. Microstructures of the three alloys irradiated with 200 keV electrons in a JEOL 200CX TEM: (a) pure aluminum irradiated for 4 to 5 minutes, (b) Al+100 ppma Si irradiated for 5 to 6 minutes, (c) Al+100 ppma Cu irradiated for 20 minutes. All magnifications are 280,000.

the pure aluminum, 5 to 6 minutes for the Al+100 ppma Si alloy and 20 minutes for the Al+100 ppma Cu alloy.

Although a large qualitative effect of alloying is obvious from Fig. 39, greater differences in behavior become known upon more detailed analysis. The pure aluminum displays ℓ-vectors both acute and obtuse with $\bar{g}$, indicating the contrast oscillations expected from defects distributed at various depths in the foil. The alloys containing Si and Cu, however, display ℓ-vectors only acute with $\bar{g}$. This indicates the defects are all at one depth (unlikely) or are very near the surface of the foil. Rühle et al. (1965) have reported a similar phenomenon, the formation of defects near the electron entrance surface of an irradiated Cu sample. Figure 27b (Chapter IV) shows in the pure aluminum sample, as predicted by the fcc catalog for this beam and $\bar{g}$, the presence of a butterfly image, thus confirming that the defects present are loops on (111) planes. For the same imaging conditions, the Cu and Si alloys failed to display such butterfly images.

No conclusions have been drawn from these results other than to note a strong but undefined effect of alloying on the electron irradiation behavior of aluminum. That the defects lay at one surface in the Cu and Si samples is puzzling. Without further experiments the mechanisms can only be speculated. If alloying suppressed the condensation of the point defects created and the electron beam ionized stray gases in the column of the microscope, the surface damage could be due to ion bombardment. The existence of a

thermal gradient from one surface to the other (this is not expected) may induce a drift of point defects to one surface. The lack of butterfly images indicates that the defects are not dislocation loops and they may be point defect clusters trapped between the matrix and the surface oxide. The strong qualitative effect that Cu and Si have in this experiment support Farrell and Houston's conclusion that the radiation damage resistance was imparted by solute in solution rather than by point defect interactions with precipitates and other defects.

In summary, all observations in this work are in general agreement with those of Farrell and Houston (1979). Little damage is seen at the lower doses; voids and prolific Si precipitation is seen at the highest dose. Si and Cu suppressed void formation at the third dose. Silicon precipitates are seen in both the pure aluminum and the Al+100 ppma Si samples while θ' precipitates are seen in the Al+100 ppma Cu sample. Although the electron irradiation experiments certainly support the conclusion that dissolved solute is important in the radiation damage behavior of these alloys, analysis of the strain around the θ' precipitates developed in the next chapters suggest the θ' precipitate may serve as important sinks and thus also influence the behavior of the Al+100 ppma Cu alloy.

CHAPTER VII
THE $|\bar{g}\cdot\bar{b}| = 0$ IMAGE

The $|\bar{g}\cdot\bar{b}| = 0$ (butterfly) image of the (100) precipitate plates found in the Al+100 ppma Cu alloy irradiated to a dose of 0.26 dpa are not quite what is expected and observed for pure edge loops in aluminum. Figure 40 shows the $|\bar{g}\cdot\bar{b}| = 0$ image of a (111) Frank loop in Al, both theoretical and experimental, and compares these to an image of a precipitate plate. The most striking difference is the greater contrast and intensity in the body of the precipitate image (i.e., the lobes aligned with $\bar{g}$). The wings of the image are also somewhat less intense than expected. Figure 20 of Chapter IV showed that the butterfly image is very sensitive to the orientation of a dislocation loop. The images of a dislocation loop and one of these precipitates are virtually identical if imaged by a diffracting vector perpendicular to the habit plane. But the $|\bar{g}\cdot\bar{b}| = 0$ images are quite distinct. The difference must be related to some structural differences between a pure edge loop and one of these precipitates. This chapter will explore various models to account for this image and simultaneously investigate the sensitivity of this imaging condition to minor structural changes of a defect.

The similarity of the precipitate to a loop is seen in its kinematic platelike shape (Chapter VI, Fig. 36), its

Fig. 40. Comparison of several $|\bar{g}\cdot\bar{b}| = 0$ images: (a) simulated image of (111) Frank loop, (b) experimental image of a (111) Frank loop, (c) experimental image of a precipitate in the Al+100 ppma Cu alloy (third dose). Magnification of (a) and (b) is 2,000,000.

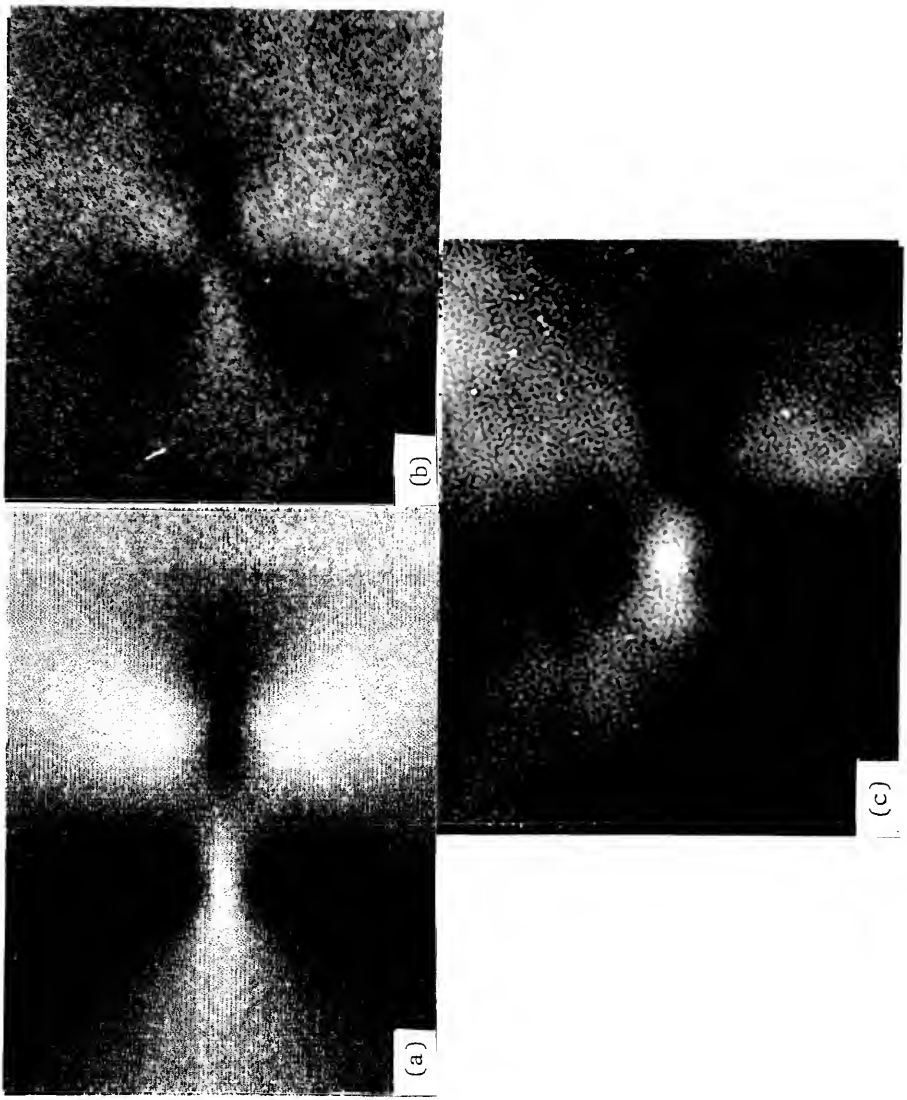
(a)
(b)
(c)

simple black-white image when $\bar{g}$ is parallel to the normal and its (altered) butterfly image. The differences can be surmised by recalling the polar displacement plots presented in Chapter III (Fig. 16). It was noted then that the body of the image results from the inward displacement of atoms about the circumference of an interstitial loop. The wings derive from the resolved outward components of the displacements. In the case of a vacancy loop the displacements invert, the circumferential displacements being outward and the major components being inward. This reverses the contrast but does not affect its symmetry. All theoretical considerations done here will assume an interstitial defect unless stated otherwise. The increased contrast of the body of the image indicates greater inward displacements about the circumference. The weakness of the wings indicates the major outward displacements are diminished. All atoms, therefore, are displaced inwards relative to their expected positions if the defect were an interstitial edge loop. In the infinitesimal approximation this would be modeled by superimposing the displacement field of a small vacancy cluster onto that of an interstital loop. The focus of this chapter is the development of models which accomplish this effect.

The difference between a precipitate and an edge loop can be simulated by the infinitesimal approximation but the detail being interpreted comes from regions very near the defect. Finite displacement calculations are therefore required. The simulation in Fig. 40 used the finite

displacement field used by Bullough et al. (1971). This displacement field is found in Appendix I, as are others which will be used.

A model of considerable theoretical interest, the segregation of solute to a dislocation loop, is developed first. Copper atoms are smaller than aluminum atoms and as such they act as point defects of vacancy nature. The segregation of the smaller copper atoms to an interstitial loop will reduce the strain energy of this defect and such segregation is expected. The substitution of copper atoms for the aluminum atoms of the loop is modeled by superimposing the displacement field of the copper atoms onto the field of the loop. This model is not being proposed to account the precipitate image but is pursued out of theoretical interest. The displacement field from a circular monolayer of copper atoms could be obtained by superimposing the strain fields of the atoms in the monolayer, but a continuum approach is taken rather than superimposing so many discrete strain centers. The array of atoms is replaced with a circular sheet, each infinitesimal surface element of which acts as a center of contraction. The mathematics and resulting field are analogous to the force on a point charge induced by a circular sheet of charge. This derivation is presented by Gray (1919). His results and their adaptation to the present problem are found in Appendix I. It is interesting to note that a circular plane of copper atoms lying on a (100) plane in aluminum is a GP(1) zone. The image of this is shown is

Fig. 41a; the normal of the plane of atoms is (100), perpendicular to the $\bar{g} = (02\bar{2})$. The image of copper solute segregated to an interstitial loop (i.e., the superposition of the above field onto that of a loop) is shown in Fig. 41b. The similarity of this image to that of the precipitates is good and verifies the general correctness of the displacement field modification.

The effect is strong and indicates segregation may be detectable if only half (or perhaps only a quarter) of the Al atoms of the loop are replaced by copper. Quantitative assessment of the sensitivity of this image is difficult for several reasons. The magnitude of the displacements from the array of copper atoms is determined by the parameter b* which represents the effective radius mismatch between copper and aluminum. For the sake of simplicity, this was assumed to be

$$b^* = (r_{Cu} - r_{Al})$$

which is probably more extreme than is appropriate. The grey scale used in plotting the theoretical images is ideal and its contrast is set by user input. It is difficult to match exactly the contrast response ultimately obtained on a positive print. Finally, experimental images contain considerable noise which will obscure detail predicted theoretically.

The solute model is not applicable to the precipitates. Eshelby (1959) has obtained the displacement field about a transformed inclusion of ellipsoidal shape. This is appropriate for a precipitate and the displacements are

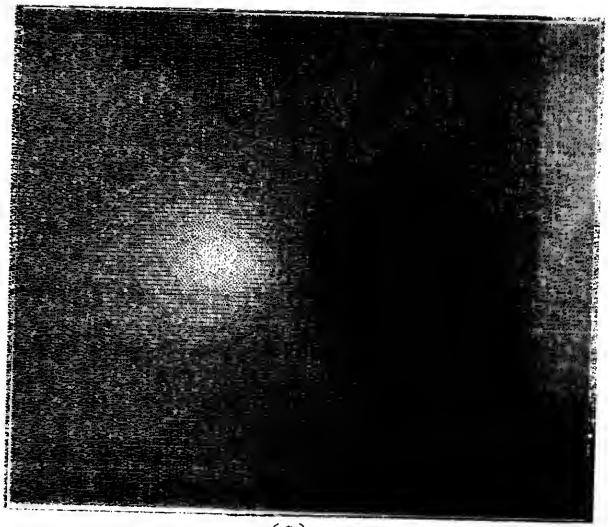

(a)

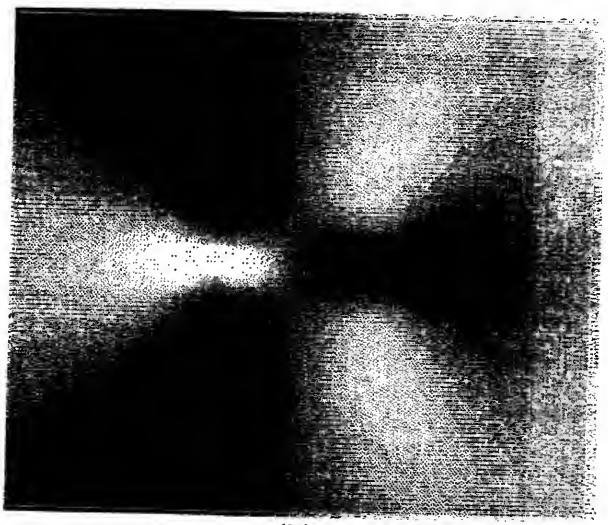

(b)

Fig. 41. (a) Simulation of a plane of copper atoms on the (100) plane of Al (i.e., a GP(1) zone). (b) Simulation of copper atoms segregated to an interstital $a_o/2[100]$ Frank loop in Al (this is not a realistic loop). $\vec{g} = [011]$, $\vec{z} = (02\bar{2})$. The length of the simulation plot corresponds to 20.0 nm.

imagined to arise as follows. An oblate spheroid of diameter much greater than its thickness (i.e., major axis >> minor axis) is imagined in an infinite elastic medium. The volume within the spheroid transforms to a misfitting shape; in the case at hand, the thickness increases and the diameter decreases. This misfit results in elastic strains inside and outside the volume which adjust to maintain force equilibrium. The elastic constants within the ellipsoid are assumed to be the same as those of the matrix. A more complete description of the model and its adaptation to the present case are given in Appendix I.

For this theoretical study the size and strains, e_{ij}, of the ellipsoid were chosen to yield a 0.1 nm outward misfit perpendicular to the face and a 0.03 nm inward misfit around the circumference. The 0.1 nm is less than the 0.23 nm misfit of an $a_o/3[111]$ edge loop and this value will reduce the intensity of the image wings. The 0.03 nm radial misfit is comparable to the previous value used for the vacancy misfit of copper. Figure 42b shows the image this model produces. To demonstrate the importance of the radial misfit Fig. 42a is the ellipsoidal model using $e_{11} = e_{22} = 0$ (i.e., no radial misfit).

This model yields a convincing image match but the effect of the composition within the precipitate was also considered. Copper atoms scatter electrons more strongly than do aluminum atoms. Assuming coherence and continuity of the diffracting planes through the precipitate, the structure factor for the operating reflection will change

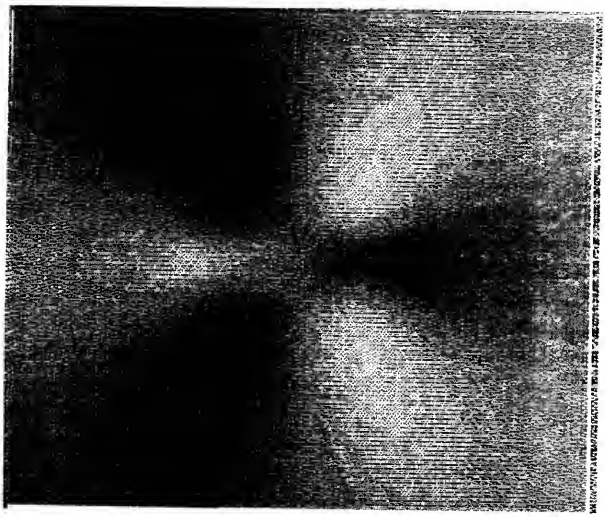

(a)

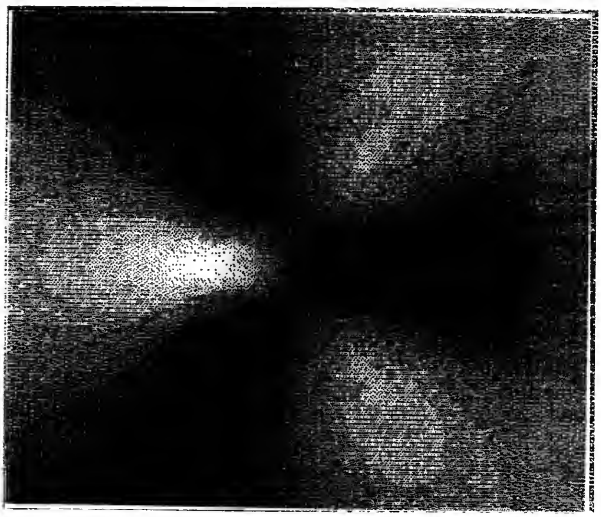

(b)

Fig. 42. Image simulation of an ellipsoidal inclussion: (a) strained outwardly normal to face but no radial strains, (b) strained outwardly normal to face and contracted radially. $\bar{z} = [011]$, $\bar{g} = (02\bar{2})$. The length of the simulation plots corresponds to 20.0 nm.

within the volume of the precipitate if copper is present. The structure factor is used in calculation of ξ_g and this parameter in turn affects $w = s\xi_g$. At $s = 0$, the parameter w proves not to change within the precipitate and the presence of copper can be modeled by decreasing the effective ξ_g' when integrating the waves inside the ellipsoid. See Appendix II for details of this model. Figure 43 shows the ellipsoid model with a radial misfit of 0.03 nm assuming the ξ_g' within the ellipsoid is 2.0 $\xi_{g=022}$, $\xi_{g=022}$, and 0.5 $\xi_{g=022}$ in a, b and c respectively. The value 2.0 $\xi_{g=022}$ models the presence of lighter atoms while 0.5 $\xi_{g=022}$ models the presence of heavier atoms. The effect is not large and considering that the changes in ξ_g' used are somewhat extreme (but not unrealistic), this effect may not be experimentally noticeable for small precipitates. Nevertheless, to demonstrate that this effect cannot account for the increased body contrast, Fig. 43d was calculated using $\xi_g' = 0.5\ \xi_{g=022}$ (i.e., heavier atoms) for the ellipsoid with no radial mismatch.

The ellipsoid model is quite adequate but simulations were also done using a strain field whose geometry is an exact disk. A thin section of a cylinder is imagined as the surface across which the radial displacements are made. The appropriate array of force dipoles is constructed on this surface and the isotropic Green's function integrated to obtain the displacements. This was carried out numerically as described in Appendix I. The misfit perpendicular to the face was obtained by superimposing displacements from two

Fig. 43. Simulations allowing for changes in density within the ellipsoid: (a) normal and radial strains, material in the ellipsoid less dense than the matrix, (b) normal and radial strains, no density change, (c) normal and radial strains, material in the ellipsoid more dense than the matrix, (d) normal strains but no radial strain, material in the ellipsoid more dense than the matrix. $\bar{Z} = [011]$, $\bar{g} = (02\bar{2})$. The length of the simulation plots corresponds to 20.0 nm.

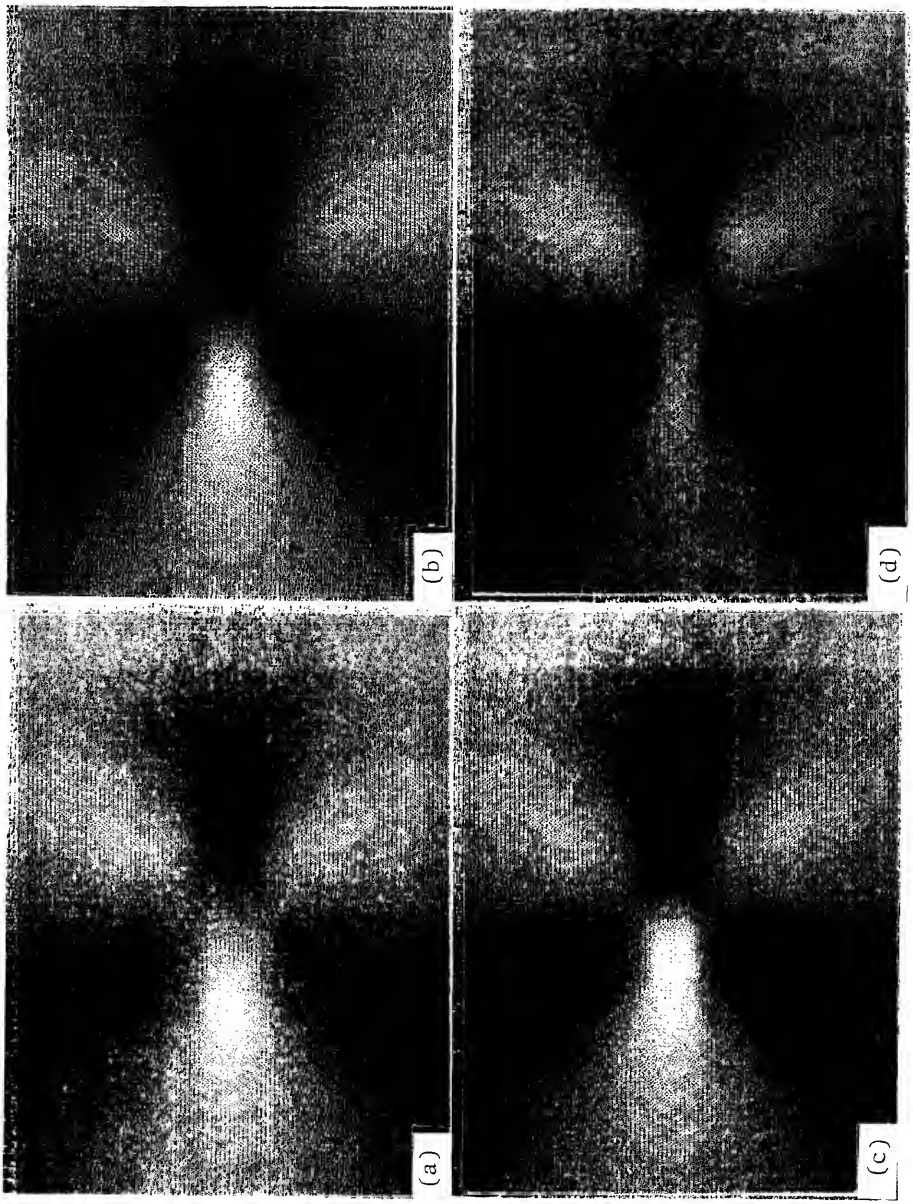
(a)
(b)
(c)
(d)

finite loops, coinciding with the two faces of the disk and of burgers vector magnitude 0.05 nm each. The radial misfit is again assumed to be 0.03 nm. This model yields Fig. 44 ($\xi_g' = 1.0\ \xi_{g=022}$). Because the radial misfit is induced directly inwards by the cylindrical surface, the contrast of the body is greater than for the ellipsoid. The radial strains from the ellipsoid were less directed due to the curved edge. Although a disk seems a better model for the precipitate's true shape, the ellipsoid yields a more convincing image. This implies the edge of the precipitate disk is rounded.

As impressive as the results of these calculations are, they are at or beyond the limits of the approximations used. For example, the columns are spaced 0.4 nm apart rather than 2.0 nm and so cross-talk between waves in neighboring columns would actually occur. The integraion step size, dz, is about 1.0 nm. This means a chunk of the column contains only 10 atoms but is nevertheless being modeled as a diffracting continuum. The displacements are calculated at distances from the defect as small as 0.5 nm, too close to expect the assumptions of continuum mechanics to apply. These criticisms invalidate only the finest details of the image. The greatest abuse is the close spacing of the columns. Proper account of the interaction of waves in neighboring columns is expected to produce an image slightly blurred in the direction of $\bar{g}$.

Aluminum is nearly isotropic but the lesser components of the displacement field are being resolved in these images

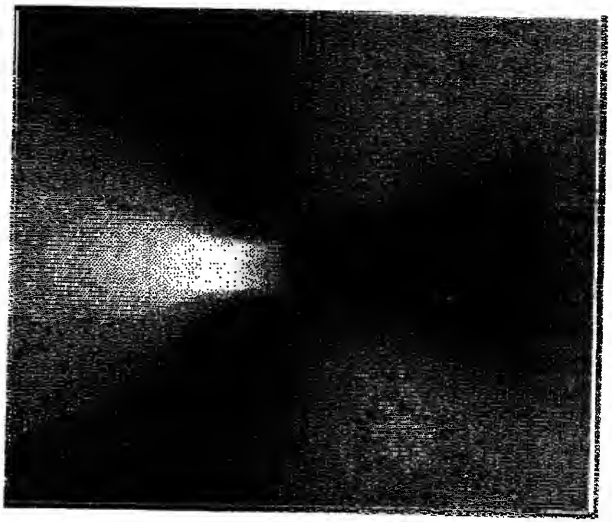

Fig. 44. Image simulation assuming displacements around a disk shaped precipitate strained outwardly normal to the face and contracted radially. Density of material in the disk is assumed the same as the matrix, $\bar{z} = [011]$, $\bar{g} = (02\bar{2})$. The length of the simulation plot corresponds to 20.0 nm.

and the effect of aluminum's anisotropy must be considered. Ohr (1979) has developed a computer program to produce both the displacements and the images of a loop in an anisotropic material but has not carried out calculations comparable to the present case. The application of anisotropic continuum mechanics to the other finite models presented has not been worked out. An estimate of the effect can be obtained by using the approximation developed by Yoffe (1970). This method is similar to the polar displacement plots presented before; it is more exact but less intuitive. The Fourier transforms of the displacements along the beam direction,

$$U_i(x,y,\Delta k) = \int_{\infty}^{\infty} u_i(x,y,z)\exp(2\pi i \Delta k z)dz$$

are resolved into $\bar{g}$ and contours of the value $\bar{g}\cdot\bar{U}(x,y,\Delta k)$ are used to represent the image. The transform $\bar{g}\cdot\bar{U}(x,y,0)$ represents the total displacement of material in the column at (x,y) and so is a measure of that columns ability to cause deviations of the electron intensity from background. This method was carried out for several cases (see Appendix I). The matrix of image contours in Fig. 45 were calculated assuming a beam direction of [011], the direction used in all the preceeding simulations. Shown are the isotropic and anisotropic calculations for both an infinitesimal loop on (100) and an infinitesimal loop onto which is superimposed a vacancy strain of spherical symmetry. The vacancy strain is equivalent to that assumed above for the copper solute on the dislocation loop. For this direction anisotropy does increase the contrast of the body, the effect being on the order of that produced by the superimposed vacancy strain.

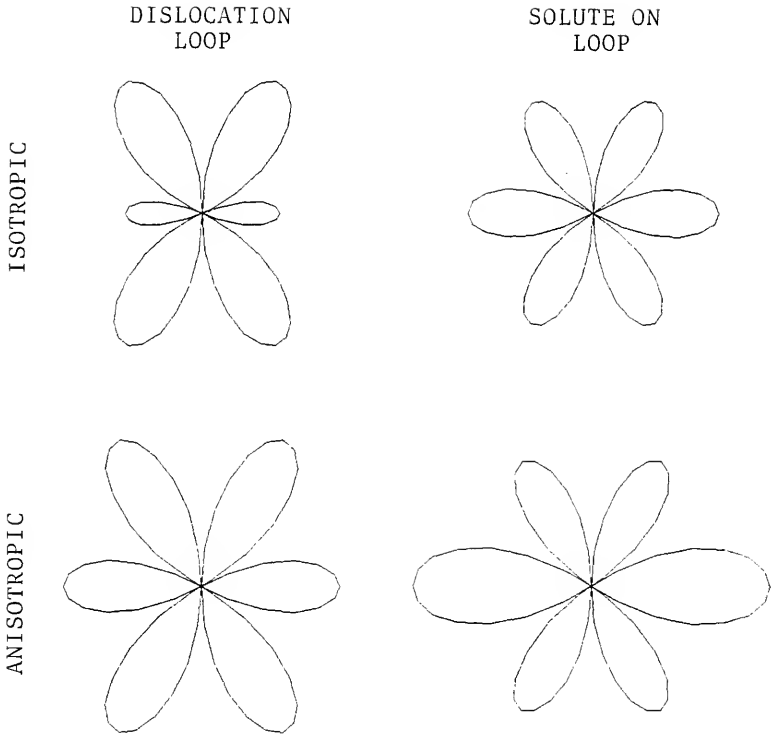

Fig. 45. Isointensity contours of a (100) Frank loop, with and without segregated solute, from the beam direction [011], assuming isotropy and anisotropy.

From this it seems aluminum's anisotropy alone can account for the contrast effect seen. Using the [001] beam direction, however, Fig. 46 is obtained. For this beam direction, anisotropy has only a minor effect and the effect is opposite that seen for the precipitates. The experimental images of the precipitates from this direction (Fig. 47) display strong contrast in the body of their images. It is concluded that the contrast does arise from the radial mismatch but that the anisotropy of aluminum is sufficient to enhance the body of $|\bar{g}\cdot\bar{b}| = 0$ images veiwed from the [011] beam direction.

The structure of the metastable Al-Cu phase θ' is consistent with the models used to explain the $|\bar{g}\cdot\bar{b}| = 0$ images. Farrell and Houston (1979) point out that 100 ppma is near the solubility limit of copper in aluminum at the irradiation temperature. This and the proven enhancement of θ' precipitation under irradiation (e.g., Katz et al., 1968) make θ' the most likely identification of the precipitates. The unit cell of θ' is given by Silcock et al. (1953-54) to be $a_o = b_o = 0.404$ nm, $c_o = 0.58$ nm. A disk of fcc material 4 unit cells thick and of composition $CuAl_2$ will transform to a disk of θ' 2 unit cells thick, thus creating a large vacancy misfit perpendicular to the faces. The misfit is so large that an $a_o(100)$ dislocation will nucleate around the circumference of the disk, as observed by Weatherly and Nicholson (1968). A disk of θ' 3 unit cells thick (1.74 nm) will require one such dislocation and so be compared to 5 unit cells of the fcc matrix. This yields a net vacancy

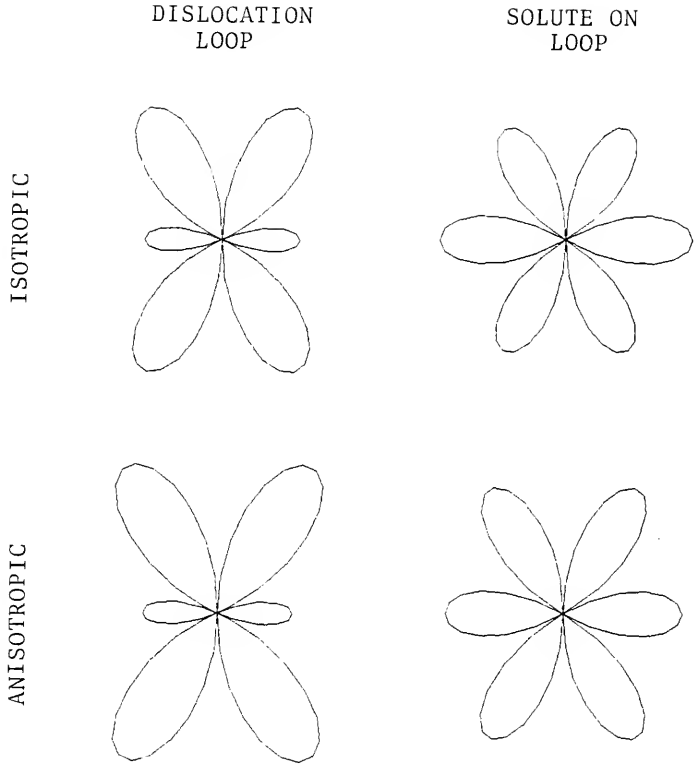

Fig. 46. Isointensity contours of a (100) Frank loop, with and without segregated solute, from the beam direction [011], assuming isotropy and anisotropy.

Fig. 47. The $|\bar{g}\cdot\bar{b}| = 0$ image of a precipitate using the beam direction [001]. Magnification is 2,000,000.

mismatch of 0.283 nm. Similarly a disk of θ' 4 unit cells thick (2.32 nm) requires 2 dislocations, producing a net mismatch of 0.107 nm.

The work of Weatherly and Nicholson (1968) produced another relevant fact about θ'. Using TEM, they observed a (100) dislocations in the broad interfaces of coarse θ' precipitates. Whereas the values of a_o and b_o of θ' determined by x-ray measurements indicate complete coherence of θ' with the aluminum matrix (on the broad faces), these dislocations are proposed to exist to take up an actual difference in the lattice parameter between θ' and Al. From the spacing of the dislocations the true a_o and b_o of θ' was determined to be either 0.4024 nm or 0.4070 nm, depending on the sign of the dislocations. The sign could not be determined directly but the dislocations were observed to nucleate within the volume of the θ' and based on the work of Silcock and Heal (1956) who proposed the true composition of θ' to be $CuAl_{1.8}$, Weatherly and Nicholson concluded the dislocations were of vacancy type. Therefore, the a_o and b_o values for θ' are 0.4070 nm. This is greater than the lattice parameter of Al. Thus, the displacements perpendicular to the broad faces of θ' are inwards and the radial mismatch is outwards, a simple change in sign from the theoretical cases considered above. The magnitude of the radial strains for θ' is $e_{11} = e_{22} = 0.0057$, comparable to the value of -0.0092 used above. The value -0.0092 was chosen to yield a net mismatch of -0.03 nm for the diameter

modeled; the value 0.0057 will yield a similar net mismatch for larger precipitates.

Figure 48 shows simulations assuming the parameters appropriate for θ', including $\xi_g' = 80.8$ nm $= 0.73\ \xi_{g=022}$. Figure 48a assumes a disk of θ' three unit cells thick, the effective burgers vector perpendicular to the face being 0.283 nm and Fig. 48b assumes a disk of θ' four unit cells thick, the effective burgers vector being 0.107 nm. The ellipsoidal model of Eshelby (1959) was used and the diameter of the precipitate was increased to 8.0 nm, compared to the previously used value of 6.5 nm.

The above images for θ' (particularly those for a 4 unit cell thick precipitate) match well the experimental images. An obvious experiment is to obtain $|\bar{g}\cdot\bar{b}| = 0$ images of precipitates known to be θ' and confirm that these images (and the radial mismatch) actually exist. Unfortunately, θ' precipitates in aged Al-Cu alloys are usually in the form of very large plates, hundreds of nanometers in diameter. Headley (1974), however, determined heat treatments by which only small precipitates of θ' formed. Figure 49 shows small θ' precipitates in an Al+4%Cu alloy quenched from 550C into 221C oil for 3 seconds, quenched to room temperature and subsequently upquenched to 221C for 5 minutes then requenched to room temperature. The wings of the images are not apparent, due to the closeness of the precipitates, but the radial strain is clear. The greater diameter of these θ' precipitates relative to those seen in the irradiated alloy (∿30 nm as opposed to ∿8 nm) results in a greater

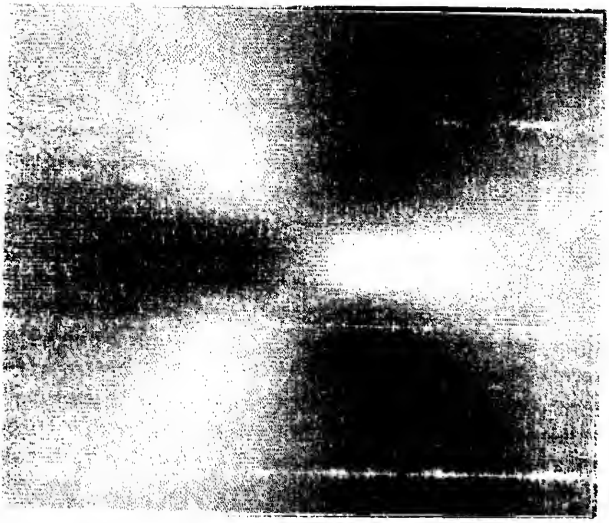

(a)

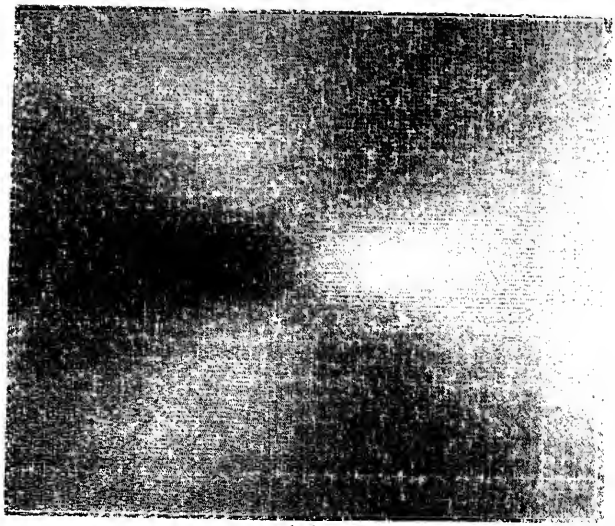

(b)

Fig. 43. Simulations assuming the parameters appropriate for θ' (a) a three unit cell thick disk of θ', (b) a four unit cell thick disk of θ'. $\bar{z} = [0111]$, $\bar{g} = (02\bar{2})$. The length of the simulation plots corresponds to 20.0 nm.

(a)

(b)

Fig. 49. Micrographs of small θ' precipitates in properly heat treated Al+4%Cu: (a) $\bar{Z} = [011]$, $\bar{g} = (200)$, so $|\bar{g}\cdot\bar{b}| \neq 0$, (b) $\bar{Z} = [011]$, $\bar{g} = (02\bar{2})$, so $|\bar{g}\cdot\bar{b}| = 0$. Magnification is 500,000.

radial strain and so a more pronounced body of the image. This result both confirms the sign of the lattice parameter misfit chosen by Weatherly and Nicholson and gives great support to the hypothesis that the precipitates in the irradiated alloy are θ'.

The theory developed in Chapters III and IV, particularly the polar displacement plots, allowed the subtle difference between a precipitate and a dislocation loop to be quickly deduced. This difference is apparent only in the $|\bar{g}\cdot\bar{b}| = 0$ image, which theoretically proved sensitive to small changes in the structure of a platelike defect. The polar displacement plot indicates that the experimental $|\bar{g}\cdot\bar{b}| = 0$ images obtained in the Al+100 ppma Cu alloy are formed by a defect having greater displacements about its circumference than are expected for a dislocation loop. The three finite models (solute on a loop, the strained ellipsoid and the strained disk) all increased these displacements and their simulated images are similar to the experimental images. The effect of increased electron scattering by heavier atoms within the precipitate is too small to account for the contrast of these images. Nor is the anisotropy of aluminum responsible for the contrast, although it does contribute for the beam direction [011].

The structure of θ', particularly the a_o and b_o lattice mismatch proposed by Weatherly and Nicholson (1968), is consistent with the models studied. The parameters for θ' produce a good image match and lead to the conclusion that

the precipitates are θ'. Moreover, the better match resulting from the parameters of four unit cell thick θ' provides an indirect measure of the thickness of the precipitates. Microscopy of precipitates known to be θ' produced the expected $|\bar{g}\cdot\bar{b}| = 0$ images and the hypotheses of this chapter rest on the foundation these data provide.

CHAPTER VIII
DISCUSSION

The results of the last chapter lead to three topics for consideration. First among these is the additional data produced for the Al-Cu system. These include information on both the structure of Θ' and the solubility of copper in aluminum. Secondly, the $|\bar{g}\cdot\bar{b}| = 0$ imaging mode has proven sensitive to minor structural changes of a defect. This allowed the identification of Θ' in the irradiated alloy. The application of this technique to other areas is worth considering. Finally, the strain field of the defect is known from the image regardless of the defect's identity. Considered in the light of other work, this strain field is expected to improve the radiation damage behavior of this alloy.

The aluminum-copper system is well studied, particularly with regard to precipitation phenomena. Any additional data for this system helps complete a classic data base against which precipitation theories can be tested. The strain assumed to obtain the Θ' image match confirms the 0.4070 nm choice of Weatherly and Nicholson (1968) for the a_o and b_o lattice parameter of Θ'. This in turn supports the hypothesis of Silock and Heal (1956) that Θ' contains vacancies on its aluminum sites and so has a composition of $CuAl_{1.8}$. That the Θ' particles have not

dissolved in the three years since their formation suggest that the alloy is indeed supersaturated at room temperature. A careful step annealing of the samples can allow the determination of the θ' solvus at low temperatures. Moreover, the transformation of θ' to θ may occur and so provide data for this phase as well. This low temperature data is especially valuable for the testing of thermodynamic theories of phase diagrams.

The $|\bar{g}\cdot\bar{b}| = 0$ image was used to identify the precipitates in the Al+100 ppma Cu alloy. This identification may seem trivial, it being the natural conclusion. Farrell and Houston (1979) point out that both Cu and Si appear to have solubilities in aluminum near or below 100 ppma at the irradiation temperature; precipitation is therefore not surprising. In addition to the composition of the alloy, other evidence suggesting the precipitates are θ' are the apparent thickness of the precipitates (GP(1) and θ" are 1 and 2 atom layers thick, respectively), and the strain seen when $\bar{g}$ is aligned with the plate normal (i.e., the black-white contrast observed by Nicholson and Nutting, 1958). In the absence of the $|\bar{g}\cdot\bar{b}| = 0$ image, the conclusion that the precipitates are θ' must rest on this circumstantial evidence alone. The volume fraction of precipitate is so low that other techniques failed to give data about the precipitate's identity. No extra diffraction spots appeared in any of the electron diffraction patterns taken from this sample. The sensitive technique of small angle x-ray scattering (SAXS) also failed

to indicate copper particles in the alloy. Hendricks (private communication, 1979) has stated that the concentration of the alloy in question is an order of magnitude below the demonstrated sensitivity of this technique. In a pure Al-Cu alloy, identifying the precipitates as θ' based on the above evidence would be reasonable but the case at hand is complicated by the presence of 100 ppma Si. The ternary phase diagram work of Phillips (1953-54) indicates that Cu and Si have little effect on the solubility of each other in aluminum. On the other hand, Carpenter and Yoo (1978) have detected transmuted silicon in the interface of large θ' plates. In view of the highly nonequilibrium and often metastable nature of precipitation during irradiation, the possibility of a complex structure formed by the co-deposition of the Cu and Si cannot be dismissed. In any event, the $|\bar{g}\cdot\bar{b}| = 0$ images are the most convincing evidence that these precipitates are simply θ'.

The sensitivity of the $|\bar{g}\cdot\bar{b}| = 0$ image has been referred to many times and the demonstrated abilities are enumerated below.

1) Sheared and unsheared small dislocation loops are most easily distinguished by this image.

2) This image displays the slight anisotropy of aluminum.

3) The segregation of undersized solute to an intersitial dislocation loop may be detected.

4) Detection of small radial strains of plate-like precipitates is possible.

5) The image responds to the rounding of the edge of a disk shaped precipitate.

Other structures this image may observe can be considered. Figure 50 shows the atomic arrangement at the edge of a four unit cell thick disk of Θ'. The view is looking down on the (100) plane. The displacements perpendicular to the face necessary for fit with the Al matrix are accounted for by simply expanding the c axis of the Θ' from 0.58 nm to 0.6 nm and contracting the Al matrix from 0.404 nm to 0.4 nm. This model assumed the a_o and b_o of Θ' to be identical to that of Al, so the misfitting atoms at the edge are the result of the incoherence at the edge and are not the result of theta prime's actual a_o and b_o mismatch. The atomic arrangement shown will outwardly strain the matrix, affecting the image. The magnitude of this strain is independent of the radius of the Θ' disk, unlike the strain resulting from the lattice parameter mismatch. The substitution of copper, silicon or vacancies for some of the atoms at the edge will relieve this strain, an such substitutions will affect the image.

This idea of solute substitution can be pursued further. The solubility of Si in aluminum is lower than that of Cu and so the presence of many Si precipitates is also expected in the Al+100 ppma Cu alloy. The number of moiré fringed precipitates, suspected of being Si, appears too low to account for all the Si expected. Silicon may have been incorporated into the Θ'. There is no direct evidence for this. The presence of Si in the precipitate would be expected to alter the structure in some slight way

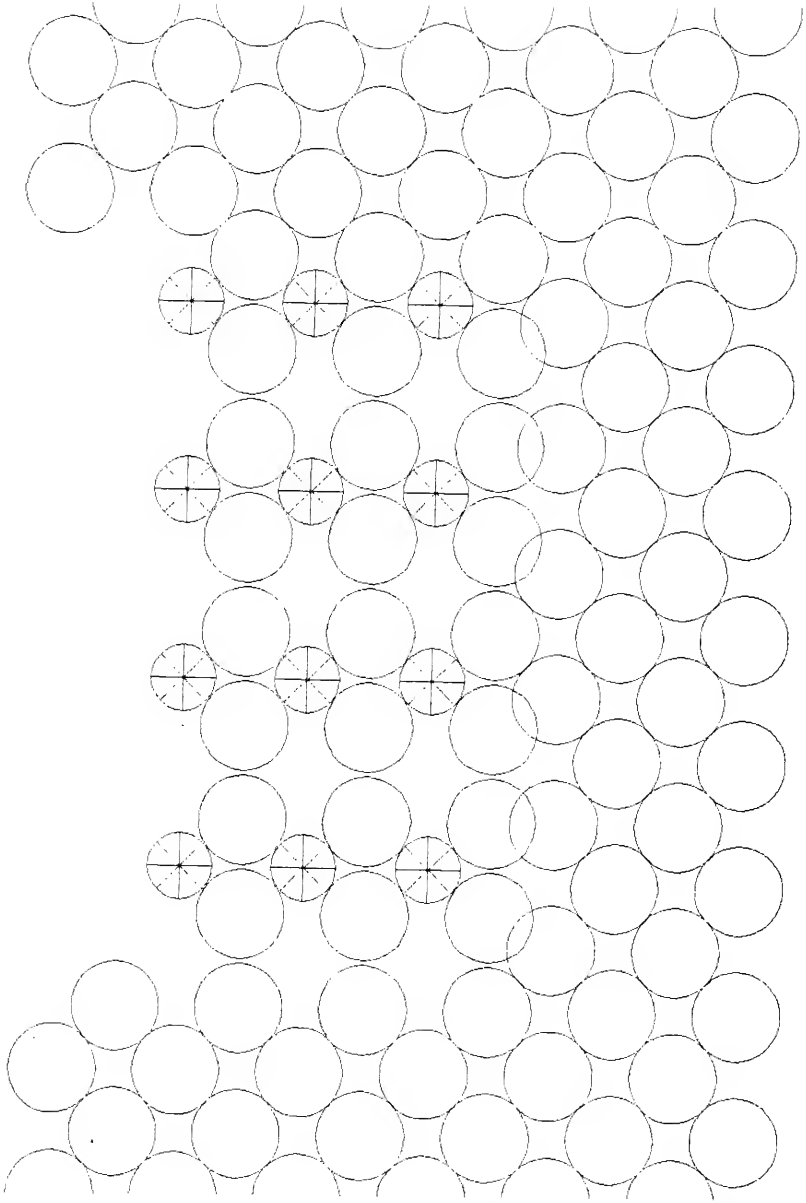

Fig. 50. Cross-sectional view of a four unit cell thick θ′ precipitate in the Al matrix. The view shows the a_o/c_o plane of the θ′.

and this alteration will in turn affect the displacement field and the image. The results presented in the last chapter are not sufficiently quantitative to allow a conclusion to be drawn, but the experimental images seem to have greater contrast in their bodies than do the simulated images, and this may be the result of Si.

The ellipsoid model, as adapted for this work, assumes the precipitate has the same elastic constants as aluminum. If elastically stiffer, the precipitate would induce greater strains to the matrix by yielding less itself, in this way increasing the body contrast. Similarly, the contrast of the image body will decrease if the θ' is less stiff than aluminum. Account of the difference in elastic constants is easily incorporated into the model, as described by Eshelby (1959). Eshelby's model assumes isotropic elasticity in the matrix and precipitate, but the image will respond not only to the matrix anisotropy, as demonstrated in the last chapter, but also the anisotropy of the precipitate. That is, an anisotropic precipitate in an isotropic matrix will, by deforming anisotropically, induce anisotropic strains in the matrix.

The speculations above and the five effects first given form an impressive list. Unfortunately, several of these effects could be convoluted in the image at once. In the case of the θ', the anisotropy of aluminum is seen to contribute to the image. Some of these other effects may be present as well. The important point, however, is that these structures and effects are detected. Computer

simulation allows account to be made of all effects suspected of contributing to the image of a particular defect. This discussion has focused mainly on Θ', but platelike precipitates in other alloy systems can also be studied in this way.

The general form of the strain field around the precipitate is known from the image, regardless of the defect's actual identity or the structure responsible for the strain. It is of interest to know if this strain field affects the radiation damage behavior of the alloy. The strain field of Θ' is similar to the strain field of a vacancy dislocation loop. By considering previous work on the interaction of point defects with dislocation loops, the effectiveness of these precipitates as point defect traps can be assessed. Sines and Kikuchi (1958) evaluated the interaction of vacancies with a small disk shaped cluster of vacancies. They modeled the cluster as an array of force dipoles distributed perpendicularly over a circular area; the model for a dislocation loop differs from this in that it also contains smaller force dipoles within the plane of the loop, acting to minimize the radial displacements induced by the perpendicular dipoles. The redistribution of vacancies about the cluster was determined by solving for the diffusion of vacancies down the gradient of the elastic interaction energy,

$$E = k(\sigma_{11} + \sigma_{22} + \sigma_{33})$$

where k is a constant dependent on the effective strain misfit of a vacancy. They found that vacancies were

repelled from the face of the disk shaped cluster and attracted to its edge. These results were later used by Grupens and Sines (1964,1965) to explain the apparent anomalous retention of vacancies in quenched Al-Cu alloys. Vacancies in quenched Al-Zn alloys (containing spherical GP zones) anneal out in several hours at room temperature, but the same process takes days in Al-Cu alloys. Grupens and Sines explained this by proposing vacancy attraction to and entrapment at GP(1) zones in Al-Cu alloys.

The majority of the strain around a Θ' precipitate is due to the mismatch of the c axis of Θ' with the aluminum matrix. This strain is very similar to that of a vacancy dislocation loop and is responsible for most of the ability of Θ' to attract point defects. The strains induced by the a_o and b_o mismatch do contribute, and the effectiveness of this strain can be assessed by the use of the infinitesimal approximation. The elastic interacion energy of a point defect depends, to first order, on the local hydrostatic pressure, $P = \sigma_{11} + \sigma_{22} + \sigma_{33}$. In the infinitesimal approximation a vacancy Frank loop is modeled by three orthogonal double forces, one along the loop normal of strength proportional to $-b_\ell C_{11}$, the other two in the habit plane proportional to $-b_\ell C_{12}$. The loop can be viewed as the superposition of a spherical strain center of strength proportional to $-b_\ell C_{12}$ and a dipole of strength proportional to $-b_\ell(C_{11} - C_{12})$. It is easy to show that the term P is zero everywhere in a spherical strain field (this proof and the rest of this development are documented in Appendix I).

Therefore the interaction energy and the loop's effectiveness as a sink depends on $-b_\ell(C_{11}-C_{12})$, the nonspherical component of the strain field. The GP(1) zone, as modeled in the last chapter, has a spherical strain field in the infinitesimal approximation and so does not interact with point defects. Its superposition onto a loop (solute segregation) does not change the loops sink strength. Since this does not agree with the observed retention of vacancies in Al-Cu, the model in the previous chapter may be inappropriate. That is, copper atoms in aluminum may have a slightly polar strain field rather than a spherical one, especially if arrayed as a circular cluster.

The θ' precipitate is modeled by adding a radial strain to the strain of a loop. The result is that the nonspherical component is proportional to

$$(b_\ell \pi r^2 - b_r \pi \Delta t r)(C_{11} - C_{12})$$

where b_ℓ is the effective burgers vector of the precipitate (i.e., the net mismatch between the thickness of the precipitate and the thickness of matrix material it replaces), b_r is the displacement at the edge of the precipitate caused by the radial strain and Δt is the thickness of the precipitate. A four unit cell thick plate of θ' has an effective burgers vector of -0.107 nm ($=b_\ell$). If its radius is 5.0 nm, b_r = 0.028 nm. Four unit cells corresponds to Δt = 2.4 nm. In this case the radial strain increases the nonspherical component of the strain field by 13% relative to the case of no radial misfit and so increases the precipitate's power as a sink.

An increase of 13% does not seem significant but it is the ratio of sink efficiencies, expressed as the bias term $(Z_i^j \times Z_v^v - Z_v^j \times Z_i^v)$, that is important to the void swelling behavior of the alloy. Moreover, the above development is a first order approximation; other effects could prove important. For example, Willis and Bullough (1969) have shown an attractive force between voids arises because of surface image forces. Wolfer and Askin (1975) calculated bias factors for spherical sinks but obtained a non zero result only by including higher order terms dependent on $(\varepsilon_{ii})^2$ and $\acute{\varepsilon}_{ij}\acute{\varepsilon}_{ij}$, where $\acute{\varepsilon}_{ij}$ is the deviatoric component of the strain field.

The strain field of these small Θ' precipitates is not the only possible source of their effectiveness as point defect sinks. Bullough and Perrin (1972) suggest that point defects migrating to coherent precipitates (such as Θ') will retain their identity as point defects when trapped in the interface and are "sitting ducks" for recombination by the arrival of an opposite defect. Carpenter and Yoo (1978) explained the improved swelling resistance of Al+4%Cu alloys containing Θ' by modeling the entrapment of point defects at the coherent Θ' interface.

The full evaluation of the sink strength of Θ', including all relevant effects, is not within the scope of this work. This discussion is intended simply to point out that the radial mismatch of Θ' will improve its effectiveness as a point defect trap. The radiation damage behavior of an alloy is sensitive to the bias terms, which

in turn are dependent on the structure of the sinks. Proper modeling and assesment of the radiation damage behavior of Al-Cu alloys should account for the radial misfit of θ', a previously ignored phenomenon.

The strain field around the θ' precipitate is predominately that of a vacancy dislocation loop and as such a θ' precipitate will act as a point defect trap. Whether or not the contribution of the radial strain proves important to the radiation damage resistance of this alloy will require more precise calculations, but the primary interest of this work has been that the $|\bar{g}\cdot\bar{b}| = 0$ image is capable of detecting this strain. This image promises to allow evaluation of radial strains arising from many effects, such as anisotropy, precipitate incoherence or differences in elastic constants. This image provided the most convincing evidence that the precipitates in the irradiated Al+100 ppma Cu alloy are θ'. This in turn adds to the knowledge of the Al-Cu system by supporting the conclusions of Weatherly and Nicholson (1968) and Silcock and Heal (1956). Solubility data is also available from this irradiated alloy.

CHAPTER IX
CONCLUSIONS AND FUTURE WORK

This work grew from interest in heterogeneous precipitation phenomena and has concentrated on the application of TEM to the analysis of small defects. The most common TEM imaging mode (dynamical two beam imaging) produces indirect images of a defect and the relationship between a defect and its image was examined by the use of computer simulations. Small dislocation loop images were studied most extensively, but an investigation of radiation damage in aluminum alloys expanded consideration to the images of small platelike precipitates.

Conclusions

A computer study of the transmission electron microscope images of small defects has dissected the theory into a few components which determine the main features of the image. The oscillations of the black-white vector of small loop images has been qualitatively described (Rühle et al., 1965) but this study explains the above or below background nature of an image point induced by displaced atoms in terms of the wave interference responsible for diffraction. The shape of the image is shown to arise from the resolved displacements of the defect. A simple and

intuitively manageable graphical method (the polar displacement plot) is presented for predicting the image. These results and other trends (such as the effect of foil tilt or loop orientation) are displayed in pictorial formats by the use of computer simulated images to reinforce and augment this theory.

Two exhaustive catalogs of simulated images of small dislocation loops expected in fcc and bcc materials were compiled. These and the above results were made accessible to the practicing microscopist in the report of Sykes et al. (1981). These catalogs complement the simulations presented by Holmes et al. (1979) by being a much larger and complete data base. Moreover, the results of Sykes et al. (1981) are displayed in a format which is more useful both theoretically and experimentally.

The catalogs were applied in a study of the radiation damage behavior of several dilute aluminum alloys. This produced a more detailed and quantitative microstructural evaluation of the alloys which proved important in the work of Farrell and Houston (1979). The results presented here are in qualitative agreement with those of Farrell and Houston. In addition, the results of the electron irradiations done in this work support Farrell and Houston's conclusion that point defect trapping at solute atoms is an important mechanism by which these alloys resist void swelling.

The origin of the $|\bar{g}\cdot\bar{b}| = 0$ image of platelike defects was known from the polar displacement plot and the

peculiarities of the $|\bar{g}\cdot\bar{b}| = 0$ images of θ' led to an investigation of the sensitivity of these images. These images detected strains largely ignored previously, and promise to be able to detect minor structural variations of a defect. Theoretical calculations showed these images respond to shearing of a dislocation loop, to segregation of solute to a dislocation loop, to the slight anisotropy of aluminum, to the radial strain of a platelike precipitate, and to the rounding of the edge of a disk shaped precipitate.

In experimental application, this image was the primary evidence identifying as θ' the precipitates observed in a neutron irradiated Al+100 ppma Cu alloy. Microscopy of precipitates known to be θ' confirm this identification and establish unambiguously that the a_o and b_o lattice parameters of θ' are greater than those of aluminum, confirming the hypothesis of Weatherly and Nicholson (1968).

The strain created by θ', being similar to a vacancy dislocation loop, is expected to contribute to the void swelling resistance of the Al+100 ppma Cu alloy. First order calculations show the radial strain of θ' increases by 13% the effectiveness of these precipitates as sinks for point defects. Accurate modeling will be required to assess the full impact of this strain on the void swelling behavior of aluminum.

Suggestions for Future Work

Theta prime is probably below its solvus at room temperature in a 100 ppma Cu aluminum alloy and the formation of θ' in these samples is irradiation assisted rather than induced. The Al-Cu system is well studied but low termperature data is naturally missing because of slow kinetics. The determination of low temperature solubilities provides important data for the testing of thermodynmic theories used to calculate phase diagrams. Careful step annealing experinents can be done to determine the solvus of θ' at this low concentration. Heating stages equipped with thermocouples are available for most electon microscopes and these experiments can be carried out in situ.

It was pointed out that the elastic model used by Grupens and Sines (1964,1965) for a GP(1) zone differed significantly from that used in the present work. Which of these two models, if either, is appropriate can be determined by the $|\bar{g}\cdot\bar{b}| = 0$ image of a GP(1) zone, since the two models will yield entirely different images; the model used in this work gave a simple black-white image but the model of Grupens and Sines will produce a butterfly image. The major experimental difficulty will be obtaining a low enough density of GP(1) zones so that the images of the zones do not overlap and interfere. These models also differ significantly in their interaction with point defects. Determining the correct model has relevance to

both the effect of GP(1) zones on radiation damage behavior and to the ability of GP(1) zones to attract Cu solute to themselves to enhance their growth (the problem studied by Grupens and Sines, 1964).

Some of the shortcomings of the present calculations have been pointed out and discussed. The full exploitation of the information avaialable in $|\bar{g}\cdot\bar{b}| = 0$ images will require more precise calculations. The inclusion of anisotropy is obvious. The early work with simulated images proved the human eye and brain superior to densitometer scans, but advances in computer technology and software will reverse this. Equipment for the digitizing of micrographs is available and quantitative use of this equipment must be developed. Ultimately, the location of every atom and its composition will be hypothesized and the continuum approaches to calculating images will be inappropriate. Multislice computing techniques (Krakow, 1980) should be employed to calculate these images. Also, the position of atoms near defects such as dislocations or precipitates must be determined not by continuum mechanics but by models for interatomic forces. Needless to say, the full development of this type of image analysis is a formidable task, but the needed theories and tools are already developing.

An image simulation program using the theories as exact as suggested above will necessarily require precise input of the experimental paramaters. In analyzing the data obtained in this work, a major difficulty encounterd was the determination of the defect's depth in the foil.

Stereomicroscopy can be used for moderate angles to resolve this, but this method is too laborious to allow routine application. The use of a computer to digitize an image and combine data from several beam directions to geometrically reconstruct the sample was briefly developed. An outline of this work and suggestions for its future development are given in Appendix III. Given proper data, the computer would return the three dimensional location of the defects in the sample. From this the depth of a defect is known, as is its projected position onto any micrograph. Knowledge of the three dimensional positions, rather than merely the depths, allows the determination of average interparticle distances, the detection of the ordering of particles into an array or the evaluation of other geometric configurations. A program such as this will not only make three dimensional analysis routine but also makes it possible to sort out defects present in high concentrations. Modifications of this program could be readily applied to many other areas.

The catalogs are quite extensive as they are, but in many applications the infinitesimal approximation will prove limiting. Figure 20 of Chapter IV displays the limited number of image types expected. A useful addition to the catalogs is the assembly of an array as in Fig. 20 using finite strain field calculations. Two arrays are suggested: one using a burgers vector magnitude such that the maximum value of $|\bar{g}\cdot\bar{b}|$ in the array is 1, the other so this maximum value is 2. Tables can be assembled which relate any image

of the infinitesimal catalogs to its nearest geometric equivalent in this new array. The inclusion of shear burgers vectors into such an array posses a problem because of the great number of possible permutations. This proliferation can be avoided by considering only three habits viewed on edge, one normal to $\bar{g}$, one 45^{o} from $\bar{g}$ and one 90^{o} from $\bar{g}$.

Finally, the appearence of the psuedo-interface structure in many of the θ' images points out the need for greater understanding of this detail if it is to be interpreted confidently and correctly. Theoretical studies with defects of modulus $|\bar{g}\cdot\bar{b}| = 1$ must be done to determine the dependence of this structure on defect depth, foil thickness, and deviation from the Bragg condition.

APPENDIX I
DOCUMENTATION OF MATHEMATICS

Displacements About a Disk of Solute Atoms

Displacements around a disk of solute atoms greater or smaller than the matrix atoms are found by integrating the displacements from a circular area, each differential element of which is assumed to be a point source having a spherical displacement field. The mathematics are analogous to the determination of the electrostatic force on a point charge located near a circular sheet of charge. This problem has been solved by Gray (1919) whose solution translates to

$$u_1(r,z) = 2\pi b^* a\int_0^\infty \exp(-\lambda z)J_1(\lambda a)J_0(\lambda r)d\lambda$$

$$u_3(r,z) = 2\pi b^* a\int_0^\infty \exp(-\lambda z)J_1(\lambda a)J_0(\lambda r)d\lambda$$

where a is the radius of the circular sheet, b^* is the effective misfit of the solute and J_0 and J_1 are Bessel functions of the first and second kind, respectively. By letting $\lambda = t/a$, these convert to

$$u_\rho(\rho,\zeta) = 2\pi b^*\int_0^\infty \exp(-\zeta t)J_1(t)J_1(\rho t)dt$$

$$u_\zeta(\rho,\zeta) = 2\pi b^*\int_0^\infty \exp(-\zeta t)J_1(t)J_0(\rho t)dt$$

where $\rho = r/a$ and $\zeta = z/a$. The integrals are Hankel-Lipshchitz integrals, which are defined as

$$I_m^n(\rho,|\zeta|) = \int_0^\infty t^n J_1(t)J_m(\rho t)\exp(-|\zeta|t)dt$$

The Hankel-Lipschitz integrals can be expressed in terms of the more numerically tractable elliptic integrals (see Eason et al., 1955)

$$I_0^0(\rho,|\zeta|) = -k\zeta F_0(k)/(2\pi\sqrt{\rho}) \begin{cases} - \Lambda(\beta,k)/2 + 1 & \text{if } \rho < 1 \\ + 1/2 & \text{if } \rho = 1 \\ + \Lambda(\beta,k)/2 & \text{if } \rho > 1 \end{cases}$$

$$I_1^0(\rho,|\zeta|) = ((2-k^2)F_0(k) - 2E_0(k))/(\pi k\sqrt{\rho})$$

where

$$k^2 = 4\rho/(\zeta^2 + (1 + \rho)^2)$$

$$\Lambda(\beta,k) = 2(F_0(k)E(\beta,k') + (E_0(k) - F_0(k))F(\beta,k'))/\pi$$

$$\cos^2\beta = \zeta^2/(\zeta^2 + (1 + \rho)^2)$$

$$k'^2 = 1 - k^2$$

$F(\beta,k)$ and $E(\beta,k)$ are elliptic integrals of the first and second kind, respectively (see Byrd and Friedmann, 1954)

$$F(\beta,k) = \int_0^\beta d\theta/\sqrt{1 - k^2\sin^2\theta}$$

$$E(\beta,k) = \int_0^\beta \sqrt{1 - k^2\sin^2\theta}\, d\theta$$

These are referred to as "complete" if $\beta = \pi/2$ and are written as $F_0(k)$ and $E_0(k)$. Making the substitutions yields

$$u_\rho(\rho,|\zeta|) = 2\pi b^* I_1^0(\rho,|\zeta|)$$

$$u_\zeta(\rho,|\zeta|) = 2\pi b^* I_0^0(\rho,|\zeta|)$$

Finally b^* must be chosen. Since the displacements in the Z direction at $\rho = 0$ and $\zeta = 0$ should equal half the misfit, $\Delta r = (a_{Cu} - a_{Al})$, and using $I_0^0(0,0) = 1$

$$\Delta r/2 = 2\pi b^*(1)$$

and so

$$u_\rho(\rho,|\zeta|) = \Delta r \Gamma_1^0(\rho,|\zeta|)/2$$

$$u_\zeta(\rho,|\zeta|) = \Delta r \Gamma_0^0(\rho,|\zeta|)/2$$

To obtain three dimensional displacements

$$u_1(x,y,z) = (x/r)u_r(\rho,|\zeta|)$$

$$u_2(x,y,z) = (y/r)u_r(\rho,|\zeta|)$$

$$u_3(x,y,z) = u_\zeta(\rho,|\zeta|)$$

where $r^2 = x^2 + y^2$.

Displacements About a Finite Dislocation Loop

Displacements of a finite dislocation loop are derived using the mathematical machinery just presented. The results below are presented by Bullough et al. (1971):

$$u_1 = \frac{xb}{r^2\rho}\left[I_1^0(\rho,\zeta) - 3|\zeta| I_1^1(\rho,\zeta)\right]$$

$$u_2 = \frac{yb}{r^2\rho}\left[I_1^0(\rho,\zeta) - 3|\zeta| I_1^1(\rho,\zeta)\right]$$

$$u_3 = -\frac{b}{2}\left[4I_0^0(\rho,\zeta) + 3|\zeta| I_0^1(\rho,\zeta)\right]\frac{\zeta}{|\zeta|}$$

where

$$\rho^2 = (x^2 + y^2)/r^2$$

$$\zeta = z/r$$

r = the loop radius.

$I_m^n(\rho,\zeta)$ are the Hankel-Lipschitz integral given before and using the same notation

$$I_1^1(\rho,\zeta) = \frac{k\zeta}{2\pi\rho\sqrt{\rho}}\left[\frac{(1 + k^2/2)}{1 + k^2}E_0(k) - F_0(k)\right]$$

$$I_0^1(\rho,\zeta) = \frac{k^3(1 - \rho^2 - \zeta^2)}{8\pi(1 - k^2)}E_0(k) + \frac{k}{2\pi\sqrt{\rho}}F_0(k)$$

Displacements About an Ellipsoidal Inclusion

Eshelby (1959) has given expressions for the displacements about an ellipsoidal inclusion arbitrarily strained relative to the matrix. The model proceeds as follows:

1) A volume of material bound by the ellipsoidal surface $x^2/a^2 + y^2/b^2 + z^2/c^2 = 1$ is removed from an infinite continuous elastic medium.

2) The removed material undergoes a transformation resulting in strains e_{ij}.

3) Forces are applied to the new shape to elastically return it to the original shape.

4) The material is inserted into the cavity and the surfaces "welded".

5) The constraining forces are removed and the ellipsoid and continuum allowed to reach equilibrium.

6) The elastic constants of the transformed ellipsoid are assumed the same as the medium.

The resulting displacements are

$$u_1 = \frac{e_{22} - e_{11}}{a^2 - b^2} \frac{\partial}{\partial x_2}(a^2 x_2 \Phi_{,1} - b^2 x_1 \Phi_{,2})$$

$$+ \frac{e_{33} - e_{11}}{c^2 - a^2} \frac{\partial}{\partial x_3}(c^2 x_1 \Phi_{,3} - a^2 x_3 \Phi_{,1})$$

$$-2((1 - \nu)e_{11} + \nu(e_{22} + e_{33}))\Phi_{,1} + S(e_{ij})$$

where $S(e_{ij})$ is a function of shear strains and has a value of zero in the present development. The expressions for u_2 and u_3 are obtained by cyclic permutation of (1,2,3) and (a,b,c). In the above, $\Phi_{,1}$ means the first derivative with respect to x_1 and Φ is defined

$$\Phi = D[(\ell^2 - x^2/k^2 + y^2/k^2)F(\theta,k)$$
$$+(x^2/k^2 - y^2/(k^2k'^2) + z^2/k'^2)E(\theta,k)$$
$$+\ell(y^2C/(AB) - z^2B/(AC))/k'^2]$$

where $a > b > c$ and

$$A^2 = a^2 + \lambda$$
$$B^2 = b^2 + \lambda$$
$$C^2 = c^2 + \lambda$$
$$\ell^2 = a^2 - c^2$$
$$k^2 = (a^2 - b^2)/(a^2 - c^2)$$
$$k'^2 = (b^2 - c^2)/(a^2 - c^2)$$
$$\theta = \arcsin(\ell/A)$$
$$D = abc/(4\ell^3(1 - \nu))$$

$F(\theta,k)$ and $E(\theta,k)$ are elliptic integrals as before and λ is the greatest root of

$$x^2/(a^2 + \lambda) + y^2/(b^2 + \lambda) + z^2/(c^2 + \lambda) = 1$$

The present work requires the less general case $a = b > c$, $e_{11} = e_{22}$, e_{33}, and all shear strains equal to zero. Also, we can take advantage of the cylindrical symmetry and concern ourselves with only the x-z plane. With $y = 0$, the above equation for λ becomes quadratic and

$$\lambda = (-a^2 + c^2 + x^2 + z^2 + R^*)/2$$

where

$$R^* = [((a^2 + c^2) - (x^2 + z^2))^2$$
$$- 4a^2c^2(1 - x^2/a^2 - z^2/c^2)]^{1/2}$$

With $a = b$ it is seen that $k = 0$ and the expression for Φ contains division by zero. The proper conceptual path would be to completely evaluate the above expressions for

the general case and take the limit as b approaches a. It is more convenient, however, to take the limit of Φ first, before obtaining the needed derivatives. Using

$$\lim_{k\to 0} F(\theta,k) = \theta$$

$$\lim_{k\to 0} E(\theta,k) = \theta$$

$$\lim_{k\to 0} (E(\theta,k) - F(\theta,k))/k^2 = ((\ell/A)\cos\theta - \theta)/2$$

$$\cos\theta = C/A$$

results in

$$\Phi = Q[(\ell^2 + z^2)\theta + (x^2 - y^2)(\ell C/A^2 - \theta)/2 + \ell y^2 C/A^2 - \ell z^2/C]$$

This result is not cylindrically symmetric, (i.e., $\Phi(\rho,0,z) = \Phi(0,\rho,z) = \Phi(x^*,y^*,z)$; $(x^*)^2 + (y^*)^2 = \rho^2$). The function

$$\Phi = Q[(\ell^2 + z^2) + (x^2 + y^2)(\ell C/A^2 - \theta)/2 - \ell z^2/C$$

is cylindrically symmetric and proves to give the expected displacements. The typographical error in Eshelby's paper responsible for this discrepancy was not identified. With the shear strains defined as zero and $e_{11} = e_{22}$, the displacements reduce to

$$u_1 = \frac{e_{11}-e_{33}}{c^2 - a^2}(c^2 x_1 \Phi_{,33} - a^2 \Phi_{,1} - a^2 x_3 \Phi_{,13}) - 2((1-\nu)e_{11} + \nu(e_{11} + e_{33}))\Phi_{,1}$$

$$u_3 = \frac{e_{33}-e_{11}}{c^2 - a^2}(-2c^2 \Phi_{,3} - c^2 x_1 \Phi_{,31} + a^2 x_3 \Phi_{,11} + b^2 x_3 \Phi_{,22}) - 2((1-\nu)e_{33} + 2\nu e_{11})\Phi_{,3}$$

Although λ is a function of x, y, and z, Eshelby points out that λ can be treated as a constant in taking the first

derivatives of Φ. Thus

$$\Phi_{,1} = \partial x(\ell C/A^2 - \theta)$$

$$\Phi_{,2} = \partial y(\ell C/A^2 - \theta)$$

$$\Phi_{,3} = \partial z(\theta - \ell/C)$$

The derivatives of λ needed in obtaining the second derivatives are

$$\partial\lambda/\partial x = 2x/Ah$$

$$\partial\lambda/\partial y = 2y/Ah$$

$$\partial\lambda/\partial z = 2z/Ch$$

where

$$h^2 = x^2/A^4 + y^2/A^4 + z^2/C^4$$

These leads to

$$\partial A/\partial x = x/(A^2h)$$

$$\partial C/\partial x = x/(ACh)$$

$$\partial\theta/\partial x = -\ell x/(A^3Ch)$$

$$\partial A/\partial z = z/(ACh)$$

$$\partial C/\partial z = z/(C^2h)$$

$$\partial\theta/\partial z = -\ell z/(A^2C^2h)$$

The derivatives with respect to y contain y, which, being set to zero, fall out in the case at hand. Using the above

$$\Phi_{,11} = \partial[\ell C/A^2 - \theta + x^2(2\ell/(A^3Ch) - 2\ell C/(A^5h))]$$

$$= \partial[\ell C/A^2 - \theta + 2x^2\ell^3/(A^5Ch)]$$

$$\Phi_{,22} = -\partial[\ell C/A^2 - \theta]$$

$$\Phi_{,33} = \partial[2(\theta - \ell/C) + 2z^2\ell(1/C^2 - 1/A^2)/C^2h]$$

$$\Phi_{,13} = \Phi_{,31} = \partial[2\ell xz(1/C^2 - 1/A^2)/A^2h]$$

Inside the ellipsoid, $\lambda = 0$ everywhere and so the terms involving the derivatives of λ fall out, giving

$$\Phi_{,11} = \partial[\ell C/A^2 - \theta]$$

$$\Phi_{,22} = 0[\ell C/A^2 - \theta]$$

$$\Phi_{,33} = 0[2(\theta - \ell/C)]$$

$$\Phi_{,13} = \Phi_{,31} = 0$$

To apply this model to the case proposed

ae_{11} = misfit at the edge of the precipitate

ce_{33} = misfit perpendicular to the disk

It is important to note that these displacements are referenced to material positions before the transformation of the ellipsoid. As before, x in the above equations is replaced by

$$r^2 = x^2 + v^2$$

and

$$u_1 = (x/r)u_r$$

$$u_2 = (v/r)u_r$$

to obtain three dimensional displacements.

Displacements About a Disk Shaped Precipitate

The displacements around a disk shaped precipitate were obtained by adding to the displacement field of two finite dislocation loops located at the top and bottom faces of the disk, the integral of displacements resulting from force dipoles in the edge surface of the disk. At any point on the edge surface is imagined a differential force dipole as in Fig. 51. The displacements are

$$u_i(\bar{X}) = \int_{-\frac{T}{2}}^{\frac{T}{2}} \int_0^{2\pi} du_i'(\bar{X}'(\theta,t))$$

The coordinates of the dipole are considered to rotate along the edge such that the $\bar{x}'$ axis is always directed outwards parallel to $\bar{r}$ and the $\bar{z}'$ axis is held parallel to the disk normal. Again concerning ourselves with only points in the x-z plane, the point $\bar{X} = (X,0,Z)$ defined in the major coordinate system (X_1,X_2,X_3) is the point $\bar{X}'(\theta,t) = (X\cos\theta - r, -X\sin\theta, Z - t)$ in the system associated with the dipole at $(r\cos\theta, r\sin\theta, t)$.

The differential displacements at $\bar{X}$ due to the dipole at $(r\cos\theta, r\sin\theta, t)$ are

$$du_m'(\bar{X}'(\theta,t)) = P_{kl}U_{km,l}(\bar{X}'(\theta,t))$$

where the prime indicates reference to the local coordinates of the dipole. The force dipole tensor P_{kl} is also referenced to the local coordinates:

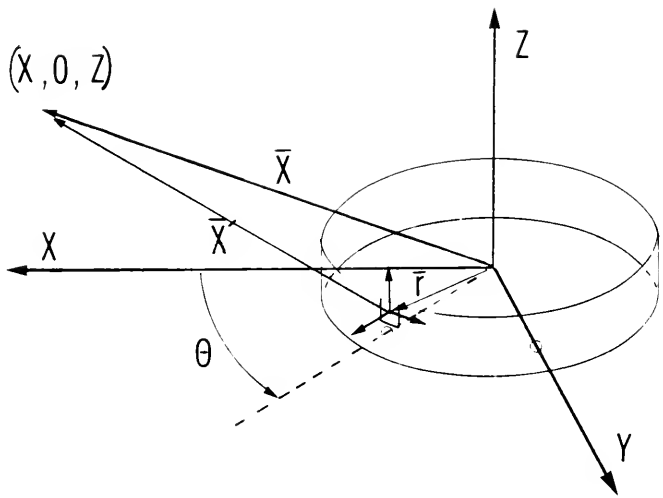

Fig. 51. The geometry and coordinates of the surface integral at the edge of the disk.

$$\bar{A} = dt\ r\ d\theta(0,\ 0,\ 1)$$

$$\bar{b} = b(0,\ 0,\ 1)$$

$$P_{kl} = b_i A_j C_{ijkl} = \begin{vmatrix} pC_{12} & 0 & 0 \\ 0 & pC_{12} & 0 \\ 0 & 0 & pC_{11} \end{vmatrix}$$

$$p = dt\ r\ d\theta$$

Transforming back to the main coordinates gives

$$du_1 = du_1' \cos\theta - du_2' \sin\theta$$

Only u_1 is needed for the $|\bar{g}\cdot\bar{b}| = 0$ image but u_2 was determined for the sake of completeness. Expanding by the use of

$$(8\ C_{11}C_{44})U_{km,l} = ((C_{12} + 3C_{44})\delta_{km}X_l$$
$$- (C_{12} + C_{44})(\delta_{kl}X_m + \delta_{ml}X_k - 3X_kX_mX_l/R^2))/R^3,$$

where R is the distance from the dipole to the point of interest, yields the cumbersome integral given in Fig. 52. Integration with respect to t is to be done last and obtaining the inner line integral with respect to θ will be done considering t = 0. Analytic integration of this line integral is foiled by the factor P in the denominator. If a segment of the loop extending from θ_1 to θ_2 is chosen such that R does not vary significantly over the segment, then R can be taken as constant. Doing this, the numerator integrates easily to give the results listed in Fig. 53.

Far away from the disk the infinitesimal approximation can be used; that is, R is considered constant for the entire loop and the results given are evaluated for $\theta_1 = 0$ and $\theta_2 = 2$. The appropriate displacement tensor to be entered into the infinitesimal point defect subroutine is

$$U_1(\bar{\chi}) = \frac{br}{8\pi C_{11}C_{44}} \int_{-T/2}^{T/2} \int_{0}^{2\pi} \left[\frac{\cos\theta}{R^3} \{(C_{11}A + 2C_{12}B)(x\cos\theta - r)\} - \frac{\sin\theta}{R^3} \{(C_{11}B + C_{12}A + C_{12}B)(-x\sin\theta)\} \right.$$

$$+ \frac{C\cos\theta(x\cos\theta - r)}{R^5} \{C_{11}(x^2\cos^2\theta - 2xr\cos\theta + r^2) + C_{12}(x^2\sin^2\theta + z^2)\}$$

$$\left. - \frac{C\sin\theta(-x\sin\theta)}{R^5} \{C_{11}(x^2\cos^2\theta - 2xr\cos\theta + r^2) + C_{12}(x^2\sin^2\theta + z^2)\} \right] d\theta dt$$

$$U_3(\bar{\chi}) = \frac{br}{8\pi C_{11}C_{44}} \int_{-T/2}^{T/2} \int_{0}^{2\pi} \left[\frac{z}{R^3} \{C_{11}B + C_{12}B + C_{12}A\} + \frac{Cz}{R^5} \{C_{11}(x^2\cos^2\theta - 2xr\cos\theta + r^2) \right.$$

$$\left. + C_{12}x^2\sin^2\theta + C_{12}\} \right] d\theta dt$$

where $A = -C_{12} + C_{44}$

$B = -C_{12} - C_{44}$

$C = 3(C_{12} + C_{44})$

b = effective radial displacement at edge

r = radius of disk

T = thickness of disk

$R = \sqrt{x^2 - 2xr\cos\theta + r^2 + z^2}$

$x = x_1$

$z = x_3$

Fig. 52. The integrals for the displacements from radial strain of the disk.

$$U_1(\chi;\ \theta_1,\ \theta_2) = \frac{br(\Delta t)}{8\pi C_{11}C_{44}R^3}\ \Big[\theta\ \frac{x}{2}(C_{11}(A+B) + 2C_{12}(B - C_{12}))$$

$$- r\sin\theta\ (C_{11}A + 2C_{12}B) + \frac{x}{4}\sin 2\theta\ (C_{11}(A - B) + 2C_{12}(B + C_{12}))$$

$$+ \frac{C}{R^2}\ \{\theta x(\frac{1}{2}\ C_{11}x^2 + 2C_{11}r^2 + C_{12}z^2 + \frac{1}{2}C_{12}x^2) - r\sin\theta\ (\frac{8}{3}C_{11}x^2 + C_{11}r^2 + \frac{1}{3}C_{12}x^2 + C_{12}z^2)$$

$$+ x\sin 2\theta\ (\frac{1}{4}C_{11}x^2 - \frac{1}{4}C_{12}x^2 + \frac{1}{2}C_{11}r^2) + \frac{x^2 r}{3}\sin\theta\cos^2\theta\ (C_{12} - C_{11})\}\Big]_{\theta_1}^{\theta_2}$$

$$U_3(\chi;\ \theta_1,\ \theta_2) = \frac{br(\Delta t)}{8\pi C_{11}C_{44}R^3}\ \Big[\theta(C_{11}B + C_{12}(A+B)) + \frac{C}{R^2}\ \{\theta(\frac{x^2}{2}(C_{11}+C_{12}) + C_{11}r^2 + C_{12}z^2)$$

$$- 2C_{11}xr\sin\theta + \frac{x^2}{4}\sin 2\theta\ (C_{11}-C_{12})\}\Big]_{\theta_1}^{\theta_2}$$

where (Δt) indicates the area associated with this line integral.

Fig. 53. Reduction of the integrals to a form suitable for numeric integration.

DELV1 = $\pi r \Delta tb$

DELV2 = $\pi r \Delta tb$

DELV3 = 0

DELV4 = DELV5 = DELV6 = 0.

The program used to calculate the image of this disk (described in the Appendix II) used pretabluated values for the inner line integral. The surface integral was completed by summing 5 of the line integrals, each assumed equally spaced along the cylindrical edge of the disk.

Calculation of Isointensity Contours for Anisotropic Aluminum

Yoffe (1970) has presented an approximate method for determining the isointensity contours of a small defect image. The methods is developed here for a small dislocation loop on a (100) habit viewed from the directions (001) and (110). The intensity is assumed proportional to the Fourier transform of the displacements along the beam direction

$$U_i(x,y,\Delta k) = \int_{-\infty}^{\infty} u_i(x,y,z)\exp(2\pi i \Delta k z)dz$$

where $\Delta k = 1/\xi_g$ and will be set to zero (thus representing $\xi_g = \infty$, the kinematical approximation). A dislocation loop is modeled by a force dipole normal to the loop of strength proportional to C_{11} and by two orthogonal dipoles in the plane of the loop of strength proportional to C_{12}. Starting with the equations for elastic force equilibrium in a continuum, the function $U_i(x,y,0)$ is sought which satisfies the equilibrium in the presence of the point forces representing the defect

$$(C\frac{\partial^2}{\partial x^2} + \frac{\partial^2}{\partial y^2})U_1 + D\frac{\partial^2}{\partial x \partial y}U_2 = -C_{11}A\frac{\partial \delta}{\partial x}$$

$$D\frac{\partial^2}{\partial x \partial y}U_1 + (\frac{\partial^2}{\partial x^2} + \frac{\partial^2}{\partial y^2})U_2 = -C_{12}A\frac{\partial \delta}{\partial y}$$

where

$$C = C_{11}/C_{44}$$

$$D = (C_{12} + C_{44})/C_{44}$$

δ = the two dimensional delta function

U_1 and U_2 are found by means of the transforms

$$U_1 = \int\int_{-\infty}^{+\infty} \Phi_1(p,q) \exp(i(px + qy))\, dpdq$$

$$U_2 = \int\int_{-\infty}^{+\infty} \Phi_2(p,q) \exp(i(px + qy))\, dpdq$$

Putting the latter into the former yields

$$(Cp^2 + q^2)\Phi_1 + Dpq\Phi_2 = iAC_{11}p/(2\pi)^2$$

$$Dpq\Phi_1 + (p^2 + Cq^2)\Phi_2 = iAC_{12}q/(2\pi)^2$$

Because the solution U(x,y,0) g with g=(010) is desired, only Φ_2 and from it U_2 need be solved. Solving for Φ_2

$$\Phi_2 = \frac{iAq}{(2\pi)^2 C}\left[\frac{A_2}{p^2 + \alpha q^2} + \frac{A_2^*}{p^2 + \alpha^* q^2}\right]$$

where

$$\alpha = ((C^2 + 1 + D^2) + \sqrt{(C^2 + 1 + D^2)^2 - 4C^2})/2C$$

$$A_2 = C_{12}\,(C - C_{11}D/C_{12}) - 1)/(\alpha - \alpha^*)$$

and the (*) denotes the complex conjugate. The inverse transform gives

$$U_2 = \frac{A}{2\pi}\,\mathrm{Re}\,\frac{2A_2 y}{C\sqrt{\alpha}(\alpha x^2 + y^2)}$$

where Re means "the real part of". The image is plotted as the locus of (x,y) points giving the same value of U_2, say $U_2 = 1$.

Obtaining results for the beam direction $\bar{Z}$ = [110] are similarly derived except the elastic constants appropriate for the coordintae system (110), (110), (001) must be used

$$C'_{11} = (C_{11} + C_{12} + 2C_{44})/2$$

$$C'_{12} = (C_{11} + C_{12} - 2C_{44})/2$$

Proceeding as before for a Frank loop with its normal aligned along (001), the force equilibrium is

$$(C'\frac{\partial^2}{\partial x^2} + \frac{\partial^2}{\partial z^2})U_1 + D\frac{\partial^2}{\partial x \partial z}U_3 = -AC'_{12}\frac{\partial \delta}{\partial x}$$

$$D\frac{\partial^2}{\partial x \partial z}U_1 + (\frac{\partial^2}{\partial x^2} + C\frac{\partial^2}{\partial z^2})U_3 = -AC'_{11}\frac{\partial \delta}{\partial z}$$

where $C' = C'_{11}/C_{44}$ and C and D are as before. This transforms to

$$(Cp^2 + q^2)\Phi_1 + Dpq\Phi_3 = iAC_{12}p/(2\pi)^2$$

$$Dpq\Phi_1 + (p^2 + Cq^2)\Phi_3 = iAC_{11}q/(2\pi)^2$$

from which

$$\Phi_1 = \frac{ipA}{(2\pi)^2 C'}[\frac{B_1}{p^2 + \beta q^2} + \frac{B_1^*}{p^2 + \beta^* q^2}]$$

where

$$\beta = (CC' + 1 + D^2 + \sqrt{(CC' + 1 - D^2)^2 - 4C'C})/2C$$

$$B_1 = C'_{12}(\beta + C'_{11}D/C_{12} - C)/(\beta - \beta^*)$$

This transforms back to the desired solution

$$U_1 = \frac{A}{2\pi C'} \text{Re} \frac{2xB_1\sqrt{\beta}}{\beta x^2 + z^2}$$

These equations were used with the following elastic constants:

isotropic:	C_{11}	= 11.8
	C_{12}	= 6.2
	C_{44}	= 2.8
anisotropic:	C_{11}	= 10.8
	C_{12}	= 6.2
	C_{44}	= 2.8

The contours for the case approximating the precipitate were obtained by superimposing the solutions for a spherical

strain center given by Yoffe:

$$U_2 = \frac{PC_{11}}{2\pi} \mathrm{Re} \frac{2A_2' y}{C\sqrt{\alpha}(\alpha x^2 + y^2)}$$

$$A_2' = ((C - D)\alpha - 1)/(\alpha - \alpha^*)$$

for $Z = [001]$ and:

$$U_1 = \frac{PC_{11}}{2\pi C'} \mathrm{Re} \frac{2B_1'\sqrt{\beta}}{\beta x^2 + z^2}$$

$$B_1' = (\beta + D - C)/(\beta - \beta^*)$$

for $\bar{Z} = [110]$. The strength of the loop was set by A=1 and the strength of the spherical strain was set by P=-0.3.

The Elastic Interaction Energy Between Point Defects and Infinitesimal Defects

The random walk diffusion of point defects is biased by their interaction with the local stress field (Bullough et al., 1969). That is, interstitials drift towards regions in tension and vacancies drift towards regions in compression. The elastic interaction energy is proportional to the local hydrostatic pressure,

$$P = \sigma_{11} + \sigma_{22} + \sigma_{33}$$

To minimize this energy, the point defects drift down the gradient of P.

The sum P has a value of zero everywhere in a spherically symmetric displacement field, as is proven below. A spherical displacement field is of the form

$$u(\bar{X}) = b\bar{X}/|\bar{X}|^3$$

where b is a constant describing the magnitude of the displacements. The stress is defined by

$$\sigma_{ij} = \varepsilon_{kl} C_{ijkl}$$

with

$$\varepsilon_{kl} = (du_k/dx_l + du_l/dx_k)/2$$

This leads to

$$P = C_{11}(du_1/dx_1 + du_2/dx_2 + du_3/dx_3)$$

Using

$$d(|X|^{-3})/dx_i = -(3/2)(x_1^2 + x_2^2 + x_3^2)^{-5/2}(2X_i)$$

gives

$$P/C_{11} = \frac{3b}{|X|^3} - \frac{3b}{|X|^5}(x_1^2 + x_2^2 + x_3^2) \equiv 0$$

The ability of a defect to influence the diffusion of point defects can be evaluated by separating the defect's strain field into spherical and nonspherical components. Since the spherical component has P = 0 everywhere, there is no gradient to influence the diffusing point defects. The point defects interact with only the nonspherical component of the strain field.

In the infinitesimal approximation, a dislocation loop of burger vector b_ℓ is described by the force dipole tensor

$$P_{kl} = b_i A_j C_{ijkl} = \begin{vmatrix} b_\ell C_{12} & 0 & 0 \\ 0 & b_\ell C_{12} & 0 \\ 0 & 0 & b_\ell C_{11} \end{vmatrix}$$

where $\bar{b} = b_\ell(0, 0, 1)$, $\bar{A} = (0, 0, 1)$ and C_{ijkl} are the elastic constants. This can be separated into spherical and nonspherical components:

$$P_{kl} = \pi r^2 b_\ell C_{12} \begin{vmatrix} 1 & 0 & 0 \\ 0 & 1 & 0 \\ 0 & 0 & 1 \end{vmatrix} + \pi r^2 b_\ell (C_{11} - C_{12}) \begin{vmatrix} 0 & 0 & 0 \\ 0 & 0 & 0 \\ 0 & 0 & 1 \end{vmatrix}$$

The magnitude of a dislocation loop's interaction with point defects is proportional to $b_\ell (C_{11} - C_{12})$.

In the infinitesimal approximation, the θ' precipitate can be modeled by adding to the strain field of a

dislocation loop the radial strain from the edge of the disk shaped precipitate (derived elsewhere in this appendix). The radial strain is

$$P_{kl} = \pi\Delta t r b_r \begin{vmatrix} (C_{11} + C_{12}) & 0 & 0 \\ 0 & (C_{11} + C_{12}) & 0 \\ 0 & 0 & 2C_{12} \end{vmatrix}$$

which separates to

$$P = \pi\Delta t r b_r (C_{11} + C_{12}) \begin{vmatrix} 1 & 0 & 0 \\ 0 & 1 & 0 \\ 0 & 0 & 1 \end{vmatrix}$$

$$+ \pi\Delta t r b_r (C_{12} - C_{11}) \begin{vmatrix} 0 & 0 & 0 \\ 0 & 0 & 0 \\ 0 & 0 & 1 \end{vmatrix}$$

where b_r is the displacement at the edge of the disk caused by the radial misfit of the disk with the matrix ($b_r = e_{11} r$). Superimposing this field with the dislocation loop yields for the nonspherical component

$$(\pi r^2 b_\ell - \pi\Delta t r b_r)(C_{11} - C_{12}) \begin{vmatrix} 0 & 0 & 0 \\ 0 & 0 & 0 \\ 0 & 0 & 1 \end{vmatrix}$$

For a four unit cell thick precipitate of θ', the misfit normal to the disk is -0.107 nm ($= b_\ell$). The radial strain is 0.0057. For a 5.0 nm radius, this gives b_r = 0.0285 nm. The thickness of four unit cells of θ' is 2.4 nm ($= \Delta t$). Thus the change in the precipitate's nonspherical strain component relative to the case of no radial strain is

$$\frac{(5.0 \times (-0.107) - 2.4 \times 5.0 \times 0.0285)}{5.0 \times (-0.107)} = 1.13$$

The precipitate's effectiveness as a point defect sink depends on the nonspherical component and so increases by 13%.

APPENDIX II
LISTINGS OF THE COMPUTER PROGRAMS

The computer programs used is this work have been discussed and documented in the work of Sykes et al. (1981). Contained in this appendix are the descriptions and listings of the main program and those subroutines used to simulate the θ' precipitate and the finite dislocation loop.

The Main Program

The main program was modified to account for a change in the scattering factor of the diffracting planes within the precipitate. This changes the parameter ξ_g (CONV). The program integrated in steps of 0.01 ξ_g. This step represents (0.01 ξ_g) angstroms. The change in scattering power means the same physical length is equivalent to a greater or lesser step in units of extinction distances. To the data reading section of the main program was added the lines below which establish a step $\Delta Z'$ (STEP2) to be used when integrating the waves within the precipitate:

```
      STEP1=ZSTEP
      READ(5,9001) CONV2
      WRITE(6,1212) CONV2
 9001 FORMAT(8F8.2)
 1212 FORMAT(1x,F10.3)
      STEP2=ZSTEP*CONV/CONV2
```

The precipitate subroutine returned a flag, NFLAG, set to 1 if the present location of the beam was in the precipitate:

```
      CALL N3D3(UD,NFLAG)
```

The substitution of the effective $\Delta Z'$ value was accomplished by the lines:

```
  301 CONTINUE
      IF(NFLAG.NE.1) GO TO 555
      IV=702
      ZSTEP=STEP2
```

```
      CALL SET1(WEFF)
      ZSTEP=STEP1
  555 T=A11(IW)*TO+A12(IW)*SO
      SO=A12(IW)*TO+A22(IW)*SO
```

```
      COMPLEX A11,A12,A22,T,TO,SO,IMAG
      COMPLEX A211,A212,A221,A222,TA1,SA1
      COMPLEX B11,B12,B21,B22
      COMPLEX TA,SOA
      COMMON A11(702),A12(702),A22(702),T,TO,SO
      COMMON IMAG,PI,ZSTEP
      COMMON X1P(3),X2P(3),X3P(3),GG1(3)
      COMMON F11,F12,F13,F21,F22,F23,F31,F32,ASTEP
      COMMON ALAT,CONV,C11,C12,C44,ANU
      COMMON ALEN,THICK,DTHICK,SLTHM,ANOB,ANOM
      COMMON DEV,GP1,GP2
      COMMON IHALF,ISIZE,JHALF,JSIZE,NDIS,N3D,NSF
CCCCCCC
C     THIS PROGRAM EXPECTS INTERPOLATION BETWEEN IMAGE
C     POINTS:  (I/J)SIZE IS THE NUMBER OF POINTS PRINTED,
C     (I/J)HALF IS THE NUMBER OF POINTS CALCULATED...
C     IN CALCULATING POINTS, THE DIFFERENCE IN SPACING
C     BETWEEN SYMBOLS IN A LINE AND SPACING BETWEEN LINES
C     MUST BE ACCOUNTED FOR.  CPRINT=(SPACING BETWEEN
C      LINES)/(SPACING BETWEEN CHARACTERS IN A LINE)
C     WINCR AND VINCR ARE THE SPACING BETWEEN IMAGE POINTS,
C     ADJUSTED TO PROPERLY ACCOUNT FOR THE PRINTER USED
C     AND TO HAVE THE (X) DIMENSION OF THE PICTURE CORRESPOND
C     TO THE LENGTH INPUT (ALEN).
CCCCCC
      DATA HLIN/10.0/,VLIN/8.0/
      CPRINT=HLIN/VLIN
      IMAG=(0.0,1.0)
      ASTEP=0.010
      ZSTEP=ASTEP
      PI=3.14159
C
C     ENTER NUMBER OF PICTURE POINTS FOR THE X(JSIZE) AND
C           Y(ISIZE) OF THE PICTURE
 1984 READ(5,7001,END=9888)JSIZE,ISIZE
      WRITE(6,7003) JSIZE,ISIZE
 7003 FORMAT('1','   PICTURE TO BE ',I5,'(X) BY ',I5,' (Y)')
      JHALF=JSIZE/2
      JSIZE=2*JHALF-1
      IHALF=ISIZE/2
      ISIZE=2*IHALF-1
C
C     ENTER NTHICK, THE NUMBER OF THICKNESSES TO BE CALCULATED
C     ENTER THE TYPE OF PICTURE DESIRED: BRIGHT FIELD (1),
C           DARK FIELD (2),  OR BOTH (3)
      READ(5,7001,END=9888) NTHICK,NTYPE
      WRITE(6,7004) NTHICK,NTYPE
 7004 FORMAT(1X,I3,' THICKNESSES, BRIGHT/DARK CODE:',I2)
C
C     ENTER THE THICKNESS INCREMENT BETWEEN PICTURES
      READ(5,9001) DTHICK
 9001 FORMAT(8F8.2)
      WRITE(6,9002) DTHICK
 9002 FORMAT(1X,'THICKNESS INCREMENTS (ANGSTROMS): ',F10.3)
C
C     MOST VALUES ARE ENTERED IN THE READ SUBROUTINE BELOW
      CALL READ(CNTX,CNTY)
      IF(JSIZE.LE.1.OR.ISIZE.LE.1) GO TO 111
      WINCR=ALEN/(JSIZE-1)
      VINCR=WINCR*CPRINT
      GO TO 112
  111 JAHLF=1
      IHALF=1
      JSIZE=1
      ISIZE=1
      VINCR=0.0
      WINCR=0.0
  112 CONTINUE
      DTHICK=DTHICK/CONV
C
C     NUMBER OF STACKING FAULTS (5 MAX), DISLOCATIONS (10 MAX),
```

```
C     AND POINT DEFECTS (10 MAX)
      READ(5,7001) NSF,NDIS,N3D
 7001 FORMAT(6I10)
      WRITE(6,7002) NSF,NDIS,N3D
 7002 FORMAT(10X,4I10,4X,A4)
C
C    CALL ROUTINES TO READ AND ESTABLISH GEOMETRY FOR DEFECTS
      IF(N3D.NE.0) CALL N3D1
C
C    DETERMINE STEPS BETWEEN THICKNESS INCREMENT AND REDEFINE
C    DTHICK TO CORRESPOND TO THE DESCRETE INCREMNETS ALLOWED
C    SLTHM IS EFFECTIVE THICKNESS AT CENTER OF PICTURE
      CALL READ2(CNTX,CNTY,ZTOP,SLTHM)
      NDZ=DTHICK*(SLTHM/THICK)/ZSTEP+0.5
      DTHICK=ZSTEP*NDZ/(SLTHM/THICK)
C
C    THIS CALL TO SETUP PRECALCULATES SCATTERING MATRICIES
      CALL SETUP
      STEP1=ZSTEP
      READ(5,9001)CONV2
      WRITE(6,1212) CONV2
 1212 FORMAT(1X,4F10.3)
      STEP2=ZSTEP*CONV/CONV2
C
C   THE START OF THE OUTPUT FILE IS PADDED TO ALLOW
C       SIMPLER LOGIC IN THE PRINT ROUTINE
      DO 106 NDEEP=1, NTHICK
  106 WRITE(10) DMMY1,DMMY2
C
C
C
C    BEGIN DOUBLE DO LOOPS TO SELECT IMAGE POINTS
C
      DO 404 I=1,IHALF
      IVAL=2*I-1
      YVAL=(IHALF-0.5-IVAL)*YINCR+CNTY
      DO 403 J=1,JHALF
      JVAL=2*J-1
      XVAL=(JVAL-JHALF+0.5)*XINCR+CNTX
C
C DETERMINE TOP OF COLUMN AND THICKNESS; NRT=STEPS TO
C  FIRST THICKNESS INCREMENT,
C  NRZ=STEPS TO BOTTOM OF THE LAST INCREMENT.
C THE (+1.5) ROUNDS AND ALLOWS FOR THE FIRST DUMMY STEP
C  NEEDED TO ESTABLISH UDO
      CALL READ2(XVAL,YVAL,ZTOP,SLTH)
      NRT=(SLTH/ZSTEP)+1.5
      NRZ=NRT+(NTHICK-1)*NDZ
C
C   INFORM DEFECT ROUTINE OF THE LOCATION OF
C   THE TOP OF THE COLUMN
      IF(N3D.NE.0) CALL N3D2(XVAL,YVAL,ZTOP)
C
C   BEGIN INTEGRATION DOWN THE COLUMN
C
      T=(1.0,0.0)
      SO=(0.0,0.0)
      UDO=0.0
      DO 302 K=1,NRZ
C   INITIALIZE DISPLACEMENT TERM TO ZERO SO
C   PROPER SUPERPOSITION SUMS RESULT
C     (TO) IS TRANS. WAVE AT TOP OF STEP, (T) AT BOTTOM
      TO=T
      UD=0.0
      DIFF=0.0
C   CALL DEFECT ROUTINE TO GET UD AND DETERMINE SCATTERING
C   MATRIX TO BE USED:  FIRST STEP OF COLUMN IS TO
C   INITIALIZE  UDO, NO INTEGRATION TAKES PLACE DUE
C   TO IF STATEMENT.
      IF(N3D.NE.0) CALL N3D3(UD,NFLAG,RC)
  434 DUDZ=(UD-UDO)/ZSTEP
      BETA=DIFF+DUDZ
```

```
      WEFF=DEV+BETA
      UDO=UD
      IF(K.EQ.1) GO TO 302
      IW=(WEFF+3.505)*100+1
      IF(IW.GE.1.AND.IW.LE.701) GO TO 301
      IW=702
      CALL SET1(WEFF)
  301 CONTINUE
  554 IF(NPLAG.NE.1) GO TO 555
      IW=702
      ZSTEP=STEP2
      CALL SET1(WEFF)
      ZSTEP=STEP1
  555 T=A11(IW)*TO+A12(IW)*SO
      SO=A12(IW)*TO+A22(IW)*SO
C
C   OUTPUT INTENSITIES IF BOTTOM OF A THICKNESS INCREMENT
C     HAS BEEN REACHED
  666 IF(K.LT.NRT) GO TO 302
      BINT=CABS(T)**2
      DINT=CABS(SO)**2
      WRITE(10) BINT, DINT
      NRT=NRT+NDZ
  302 CONTINUE
  403 CONTINUE
  404 CONTINUE
C
CCCCCC
C     FOR EACH THICKNESS, CALL PRINT ONCE OR TWICE TO GET A
C       BRIGHT FIELD OR DARK FIELD PICTURE OR BOTH
C
      DO 104 NDEEP=1,NTHICK
      IF(NTYPE.EQ.2) GO TO 105
      NPIC=0
      CALL PRINT(NDEEP,NTHICK,NPIC)
      IF(NTYPE.EQ.1) GO TO 104
  105 NPIC=1
      CALL PRINT(NDEEP,NTHICK,NPIC)
  104 CONTINUE
C
C   RESET FILE AND GO FOR DATA FOR ANOTHER PICTURE
C
      REWIND 10
      GO TO 1984
 9888 STOP
      END
```

The Ellipsoidal Precipitate Subroutine

Due to the analytic equations available for these displacements, this subroutine could be straightforwardly written. This subroutine is infact the subroutine previously used to obtain displacements about an infinitesimal defect (see Sykes et al., 1981). Modifications simply replaced the equations for the displacements; the geometry remained the same.

```
      SUBROUTINE N3D1
      COMPLEX ALPHA1,ALPHA2
      COMPLEX A11,A12,A22,T,S,SO,IMAG
       REAL H,H2,L,LAM,L2,L3
      DIMENSION PV1(3),PV2(3),PV3(3)
      COMMON A11(702),A12(702),A22(702),T,S,SO
      COMMON IMAG,PI,ZSTEP
      COMMON X1P(3),X2P(3),X3P(3),GG1(3)
      COMMON P11,P12,P13,P21,P22,P23,P31,P32,P33
      COMMON ALAT,CONV,C11,C12,C44,ANU
      COMMON ALEN,THICK,DTICK,SLTHM,ANOR,ANOM
      COMMON DEV,GP1,GP2
      COMMON IHALF,ISIZE,JHALF,JSIZE,NDIS,N3D,NSF
      READ(5,2000) PV1,PV2,PV3
CC
CC   READ IN AND NORMALIZE THE DEFECT COORDINATES
      WRITE(6,9002) PV1,PV2,PV3
      CALL NORM(PV1)
      CALL NORM(PV2)
      CALL NORM(PV3)
CC
CC     READ IN MAJOR AND MINOR AXIS OF ELLIPSOID,
CC           THE STRAINS ALONG THESE AXIES AND
CC           POISSONS RATIO
      READ(5,2000) AS,CS,E11,E33,SIG
 2000 FORMAT(10F8.4)
      WRITE(6,3002) AS,CS,E11,E33,SIG
 3002 FORMAT(1X,10F8.4)
CC
CC    ESTABLISH CONSTANTS NEEDED LATER
      ABC=AS*AS*CS
       AS=AS*AS
       CS=CS*CS
      SIG1=2*((1.0-SIG)*E11+SIG*(E11+E33))
      SIG3=2*((1.0-SIG)*E33+SIG*(E11+E11))
      DELTE=(E33-E11)/(CS-AS)
       RR2=AS+CS
      L2=AS-CS
      L=SQRT(L2)
      L3=L**3
      CNN=AS*CS
      ABC=ABC/(4*L2*L*(1.0-SIG))
      WRITE(6,3004) SIG1,SIG3,DELTE,ABC
 3004 FORMAT(1X,5E20.5)
CC
CC    DETERMINE TRANSFORM MATRIX BETWEEN PICTURE AND
CC       DEFECT COORD.S
      AP11=PV1(1)*X1P(1)+PV1(2)*X1P(2)+PV1(3)*X1P(3)
      AP12=PV1(1)*X2P(1)+PV1(2)*X2P(2)+PV1(3)*X2P(3)
      AP13=PV1(1)*X3P(1)+PV1(2)*X3P(2)+PV1(3)*X3P(3)
      AP21=PV2(1)*X1P(1)+PV2(2)*X1P(2)+PV2(3)*X1P(3)
      AP22=PV2(1)*X2P(1)+PV2(2)*X2P(2)+PV2(3)*X2P(3)
      AP23=PV2(1)*X3P(1)+PV2(2)*X3P(2)+PV2(3)*X3P(3)
      AP31=PV3(1)*X1P(1)+PV3(2)*X1P(2)+PV3(3)*X1P(3)
      AP32=PV3(1)*X2P(1)+PV3(2)*X2P(2)+PV3(3)*X2P(3)
      AP33=PV3(1)*X3P(1)+PV3(2)*X3P(2)+PV3(3)*X3P(3)
CC
CC    ESTABLISH ONE STEP OF THE BEAM THROUGH THE FOIL
      XINCR=-ZSTEP*CONV*AP13
      YINCR=-ZSTEP*CONV*AP23
      ZINCR=-ZSTEP*CONV*AP33
      READ(5,2000) PX,PY,PZ
 9002 FORMAT(1X,3F8.3,4X,3F8.3,4X,3F8.3)
CC
CC    READ AND TRANSFORM DEFECT LOCATION TO PICTURE COORD.S
      WRITE(6,9003) PX,PY,PZ
 9003 FORMAT(' LOC',3F10.3)
       PX1=(PX*X1P(1)+PY*X1P(2)+PZ*X1P(3))/CONV
      PX2=(PX*X2P(1)+PY*X2P(2)+PZ*X2P(3))/CONV
      PX3=(PX*X3P(1)+PY*X3P(2)+PZ*X3P(3))/CONV
      RETURN
```

```
      ENTRY N3D2(WVAL,VVAL,ZTOP)
C
C     TRANSFORM TOP OF COLUMN TO DEFECT COORDINATES
      XV=(WVAL-PX1)*CONV
      YV=(VVAL-PX2)*CONV
      ZV=(ZTOP-PX3)*CONV
      XP=AP11*XV+AP12*YV+AP13*ZV
      YP=AP21*XV+AP22*YV+AP23*ZV
  102 ZP=AP31*XV+AP32*YV+AP33*ZV
      RETURN
      ENTRY N3D3(UD,NFLAG,RO)
C
C     NFLAG WILL BE SET TO 1 IF BEAM IS IN THE ELLIPSOID
      NFLAG=0
      X2=XP**2+YP**2
      Z2=ZP**2
      X=SQRT(X2)
      Z=SQRT(Z2)
C
C DETERMINE IF (X,Z) IS IN THE ELLIPSOID
      TEST=X2/AS+Z2/CS
      IF(TEST.GT.1.0) GO TO 222
C
C  INSIDE ELLIPSIOD LAMBA IS ZERO EVERYWHERE
C  THE DERIVATIVES SIMPLIFY TO:
C
      C=SQRT(CS)
      TH=ARSIN(L/SQRT(AS))
      PHI11=L*C/AS-TH
      PHI1=X*PHI11
      PHI13=0.0
      PHI31=0.0
      PHI22=PHI11
      PHI33=2*(TH-L/C)
      PHI3=Z*PHI33
      NFLAG=1
      GO TO 333
  222 CONTINUE
C
C    DETERMINE  LAMBA
C
      R2=X2+Z2
      BQ=RR2-R2
      LAM=(SQRT(BQ*BQ-4.0*CNN*(1.0-TEST))-BQ)/2.0
C
C     DEFINE A, C, H, THEIR POWERS AND RECIPROCALS AND THETA
C
      A2=AS+LAM
      RA2=1.0/A2
      A=SQRT(A2)
      RA=1.0/A
      C2=CS+LAM
      RC2=1.0/C2
      C=SQRT(C2)
      RC=1.0/C
      TH=ARSIN(L*RA)
      H2=X2*RA2*RA2+Z2*RC2*RC2
      H=SQRT(H2)
      RH=1.0/H
C
C
C     DEFINE AN OFTEN OCCURRING GROUP
C
      DCA=RC2-RA2
C
C     EVALUATE THE NEEDED DERIVATIVES
C
      PHI1=X*(L*C*RA2-TH)
C
      PHI11=L*C*RA2-TH+2*X2*L3*RA2*RA2*RA*RC*RH
```

```
C
      PHI13=2*X*Z*L*RA2*RH*DCA
      PHI31=PHI13
C
      PHI22=L*C*RA2-TH
C
      PHI3=2*Z*(TH-L*RC)
C
      PHI33=2*(TH-L*RC+Z2*L*RC2*RH*DCA)
C
C
  333 CONTINUE
CC
CC    DETERMINE DISPLACEMENTS
      U1C=CS*X*PHI33-AS*PHI1-AS*Z*PHI13
      U1C=ABC*(DELTE*U1C-SIG1*PHI1)
      U3C=-2*CS*PHI3-CS*X*PHI31+AS*Z*PHI11+AS*Z*PHI22
      U3=ABC*(DELTE*U3C-SIG3*PHI3)
      IF(ZP.LT.0.0) U3=-U3
CC
CC    DETERMINE RESOLVED COMPONENTS
      U1=U1C*XP/X
      U2=U1C*YP/X
      UP1=AP11*U1+AP21*U2+AP31*U3
      UP2=AP12*U1+AP22*U2+AP32*U3
      UD=UD+(UP1*GP1+UP2*GP2)/CONV
CC    INCREMENT THE BEAM
CC
      XP=XP+XINCR
      YP=YP+YINCR
  103 ZP=ZP+ZINCR
      RETURN
      END
```

The Disk Precipitate Subroutine

This subroutine was used to obtain displacements about the disk shaped precipitate and a finite dislocation loop. This is a modification of the infinitesimal point defect subroutine documented by Sykes et al. (1981). The subroutine used values interpolated from a matrix of displacements in the x-z plane (these were precalculated and stored on disk by another program, described later in this appendix). The geometry is very restrictive; only a disk viewed on edge can be simulated. The matrix of displacements, being precalculated for a specific radius, can only be used to simulate that size defect, although the thickness and displacement magnitudes (set by BL and BE) can be varied. The geometry assumed a finite dislocation loop at the top and bottom surface of the disk and five line integrals for the radial strain spaced evenly along the edge surface (summing the displacements from these five completed the surface integral). By putting the radial misfit BE to zero and letting the disk thickness become very small (say 1 Angstrom), the displacement field of a dislocation loop is produced. When the beam was beyond the range of the matrix the infinitesismal approximation was used.

Within the volume of the precipitate, the displacements resulting from this model are incorrect, there being a discontinuity at the surface of the disk. The displacements within the precipitate were assumed to linearly increase

with r and be continuous at the surface of the disk. This is what is found for the ellipsoidal model. The net result of this is that for s = 0, w = 0 everywhere within the disk. Rather than correct the displacements, the main program was modified to set w = 0 when the beam was in the disk (i.e., when NFLAG=1).

As it turned out, the numerical integration of the radial strains was not sufficiently precise near the edge of the precipitate and the displacements produced were too large. A "band-aid" was placed in the program to force the displacements to vary smoothly from BE/2 at the edge to those values calculated at some distance from the edge (at 1.2r).

```
      SUBROUTINE N3D1
      COMPLEX ALPHA1,ALPHA2
      COMPLEX A11,A12,A22,T,S,SO,IMAG
      DIMENSION PV1(3),PV2(3),PV3(3)
      COMMON A11(702),A12(702),A22(702),T,S,SO
      COMMON IMAG,PI,ZSTEP
      COMMON X1P(3),X2P(3),X3P(3),GG1(3)
      COMMON F11,F12,F13,F21,F22,F23,F31,F32,F33
      COMMON ALAT,CONV,C11,C12,C44,ANU
      COMMON ALEN,THICK,DTICK,SLTHM,ANOR,ANOM
      COMMON DEV,GP1,GP2
      COMMON IHALF,ISIZE,JHALF,JSIZE,NDIS,N3D,NSF
      DIMENSION UE1(30,20),UE3(30,20),UL1(30,20),UL3(30,20)
C
C     THIS SUBROUTINE READS FROM DISK DISPLACEMENTS OF
C     A LOOP (UL1&UL3) AND OF THE EDGE OF A PPT (UE2&UE3)
C     THESE ARE PRECALCULATED BY ANOTHER PROGRAM AND ARE
C     FOR A SPECIFIC RADIUS (32.5)
C     THE THICKNESS USED HERE IS VARIABLE AND BY SETTING
C     THE THICKNESS VERY SMALL (1.0 ANGSTOM) AND BE=0.0
C     A DISLOCATION LOOP IS SIMULATED
C
C     READ IN DEFECT COORDINATES.
      READ(5,9001) PV1,PV2,PV3
      WRITE(6,9002) PV1,PV2,PV3
C
C     READ IN THE THICKNESS AND RADIUS
      READ(5,9001) TICK,RAD
 9001 FORMAT(10F8.2)
      WRITE(6,8006) TICK,RAD
 8006 FORMAT(' THICKNESS AND RADIUS:  ',2F20.5)
      THICK2=TICK/2.0
      THICK5=TICK/5.0
      RAD2=RAD**2
C
C     NORMALIZE DEFECT COORD.S AND DETERMINE TRANSFORM TO
C      PICTURE COORDINATES
      CALL NORM(PV1)
      CALL NORM(PV2)
      CALL NORM(PV3)
      AP11=PV1(1)*X1P(1)+PV1(2)*X1P(2)+PV1(3)*X1P(3)
      AP12=PV1(1)*X2P(1)+PV1(2)*X2P(2)+PV1(3)*X2P(3)
      AP13=PV1(1)*X3P(1)+PV1(2)*X3P(2)+PV1(3)*X3P(3)
      AP21=PV2(1)*X1P(1)+PV2(2)*X1P(2)+PV2(3)*X1P(3)
      AP22=PV2(1)*X2P(1)+PV2(2)*X2P(2)+PV2(3)*X2P(3)
      AP23=PV2(1)*X3P(1)+PV2(2)*X3P(2)+PV2(3)*X3P(3)
      AP31=PV3(1)*X1P(1)+PV3(2)*X1P(2)+PV3(3)*X1P(3)
      AP32=PV3(1)*X2P(1)+PV3(2)*X2P(2)+PV3(3)*X2P(3)
      AP33=PV3(1)*X3P(1)+PV3(2)*X3P(2)+PV3(3)*X3P(3)
C
C     DEFINE ONE STEP OF THE BEAM
      XINCR=-ZSTEP*CONV*AP13
      YINCR=-ZSTEP*CONV*AP23
      ZINCR=-ZSTEP*CONV*AP33
C
C     READ BURGERS VECTOR MAGNITUDE OF THE LOOP (BL)
C      AND AT THE EDGE (BE) AND ADJUST FOR THE USE
C      OF 2 AND 5 LOOPS.
      READ(5,9001)BL,BE
      WRITE(6,8007) BL,BE
 8007 FORMAT(1X,'LOOP AND EDGE BURG:  ',2F10.4)
      ALOOP=BL/2.0
      AEDGE=THICK5*BE
      WRITE(6,1010) AEDGE,THICK5
 1010 FORMAT(1X,2F20.5,E20.5)
C
C     READ DISPLACEMENT MATRICES FROM DISK.
      READ(11) UE1,UE3,UL1,UL3
C
C     READ DEFECT POSITION AND CONVERT TO PICTURE COORD.S
      READ(5,9001) PX,PY,PZ
```

```
 9002 FORMAT(1X,3F8.3,4X,3F8.3,4X,3F8.3)
      WRITE(6,9003) PX,PY,PZ
 9003 FORMAT(' LCC',3F10.3)
       PX1=(PX*X1P(1)+PY*X1P(2)+PZ*X1P(3))/CONV
      PX2=(PX*X2P(1)+PY*X2P(2)+PZ*X2P(3))/CONV
      PX3=(PX*X3P(1)+PY*X3P(2)+PZ*X3P(3))/CONV
CC
CC   DEFINE TERMS NEEDED FOR USING THE INFINITESIMAL APPROX.
      DELV1=PI*RAD*TICK*BE
      DELV2=DELV1
      DELV3=PI*RAD2*BL
      PM1=(DELV1*C11+DELV2*C12+DELV3*C12)
      PM2=(DELV1*C12+DELV2*C11+DELV3*C12)
      PM3=(DELV1*C12+DELV2*C12+DELV3*C11)
      BVAL=1.0/(8.0*PI*C11*C44)
      RETURN
CC
CC
CC
      ENTRY N3D2(WVAL,VVAL,ZTOP)
CC
CC   DETERMINE TOP OF COLUMN IN DEFECT COORD.S
      XV=(WVAL-PX1)*CONV
      YV=(VVAL-PX2)*CONV
      ZV=(ZTOP-PX3)*CONV
      XP=AP11*XV+AP12*YV+AP13*ZV
      YP=AP21*YV+AP22*YV+AP23*ZV
  102 ZP=AP31*XV+AP32*YV+AP33*ZV
      RETURN
CC
CC
CC
      ENTRY N3D3(UD,NFLAG)
CC
CCC   NFLAG IS SET TO 1 IF BEAM IS IN THE PPT.
      NFLAG=0
      RO=XP**2+YP**2
      IF(ABS(ZP).LE.THICK2.AND.RO.LE.RAD2) NFLAG=1
  883 RO=SQRT(RO)
CC
CCC IF FAR AWAY, USE THE INFINITESIMAL APPROX.
      IF(RO.GT.145.0) GO TO 235
      IX=(RO/5.0)+1
      ULP1=0.0
      ULP3=0.0
      UEP1=0.0
      UEP3=0.0
      JX=IX+1
      GX=(5.0*IX-RO)/5.0
      FX=1.0-GX
CC
CCC FOR LOOP AT TOP AND BOTTOM OF CYLANDER,
CCC SUM DISPLACEMENTS
CCC USING INTERPOLATED VALUES.
      ZL=ZP-THICK2
      DO 991 LOOP=1,2
      KZ=1
      IF(ZL.LT.0.0) KZ=-1
      IZ=(ABS(ZL)/5.0)+1.0
      JZ=IZ+1
      GZ=(5.0*IZ-ABS(ZL))/5.0
      FZ=1.0-GZ
      ULP1=ULP1+GX*(GZ*UL1(IX,IZ)+FZ*UL1(IX,JZ))+
     & FX*(GZ*UL1(JX,IZ)+FZ*UL1(JX,JZ))
      ULP3=ULP3+KZ*(GX*(GZ*UL3(IX,IZ)+FZ*UL3(IX,JZ))+
     & FX*(GZ*UL3(JX,IZ)+FZ*UL3(JX,JZ)))
      ZL=ZL+TICK
  991 CONTINUE
CC
CCC FOR 5 EDGE LINE INTEGRALS DISTRIBUTED EVENLY ON THE
CCC CYLINDRICAL SURFACE, SUM DISPLACEMENTS USING
CCC  INTERPOLATED VALUES.
```

```
      ZL=ZP-3*THICK5
      DO 992 NEDGE=1,5
      ZL=ZL+THICK5
      KZ=1
      IF(ZL.LT.0.0) KZ=-1
      IZ=(ABS(ZL)/5.0)+1
      JZ=IZ+1
      GZ=(5.0*IZ-ABS(ZL))/5.0
      FZ=1.0-GZ
      U1=GX*(GZ*UE1(IX,IZ)+FZ*UE1(IX,JZ))+
     & FX*(GZ*UE1(JX,IZ)+FZ*UE1(JX,JZ))
      UEP1=UEP1+U1
      UEP3=UEP3+KZ*(GX*(GZ*UE3(IX,IZ)+FZ*UE3(IX,JZ))+
     & FX*(GZ*UE3(JX,IZ)+FZ*UE3(JX,JZ)))
  992 CONTINUE
CC
CCC   MULTIPLY DISPLACEMENTS BY BURGERS VECTOR MAGNITUDES
CCC   TO OBTAIN THE FINAL VALUES.
      ULP1=ULP1*ALOOP
      ULP3=ULP3*ALOOP
      UEP1=UEP1*AEDGE
      UEP3=UEP3*AEDGE
CC
CCC   VERY CLOSE TO THE EDGE THE NUMERICAL INTEGRATION
CCC    WAS NOT ACCURATE AND GAVE LARGE VALUES;  THE
CCC    FOLLOWING ARBITRARY FUNCTION PRODUCES A SMOOTH
CCC    VARIATION OF DISPLACEMENTS UP TO THE EDGE AND
CCC    MAINTAINED THEM BELOW BE/2.
      IF(RO.GE.45.0.OR.ABS(ZP).GT.THICK2) GO TO 712
  711 IF(RO.LT.32.5) GO TO 713
      D=(RO-32.5)/12.5
      DD=1.0-D
      UEP1=(BE/2.0)*(.526667+D*DD*.30666+DD*DD*.47333)
      GO TO 712
  713 CONTINUE
CC
CC    WITHIN THE PPT, THE EQUATIONS GIVE UNREALISTIC VALUES
CC      THE MAIN PROGRAM IGNORES U.G IF NFLAG=1, SO
CC      THE DISPLACEMENTS ARE ARBITRATILY SET TO ZERO HERE.
      U3=0.0
      U1=0.0
      U2=0.0
      GO TO 236
  712 CONTINUE
      U1=(ULP1+UEP1)*XP/RO
      U2=(ULP1+UEP1)*YP/RO
      U3=ULP3+UEP3
      GO TO 236
CC
CC    THE FOLLOWING IS THE INFINITESIMAL APPROX.
  235 RVAL=RO
      XPR=XP/RVAL**3
      YPR=YP/RVAL**3
      ZPR=ZP/RVAL**3
      C2=3.0*(C12+C44)/RVAL**2
      XC2=C2*XP**2
      YC2=C2*YP**2
      ZC2=C2*ZP**2
      T1=(XPR*(-C12+C44+XC2))*PM1
      T2=(XPR*(-C12-C44+YC2))*PM2
      T3=(XPR*(-C12-C44+ZC2))*PM3
      U1=BVAL*(T1+T2+T3)
      T1=(YPR*(-C12-C44+XC2))*PM1
      T2=(YPR*(-C12+C44+YC2))*PM2
      T3=(YPR*(-C12-C44+ZC2))*PM3
      U2=BVAL*(T1+T2+T3)
      T1=(ZPR*(-C12-C44+XC2))*PM1
      T2=(ZPR*(-C12-C44+YC2))*PM2
      T3=(ZPR*(-C12+C44+ZC2))*PM3
      U3=BVAL*(T1+T2+T3)
  236 CONTINUE
CC
```

```
CC  RESOWE DISPLACEMENTS INTO G;  INCREMENT THE BEAM
      UP1=AP11*U1+AP21*U2+AP31*U3
      UP2=AP12*U1+AP22*U2+AP32*U3
      UD=UD+(UP1*GP1+UP2*GP2)/CONV
      XP=XP+XINCR
      YP=YP+YINCR
  103 ZP=ZP+ZINCR
      RETURN
      END
```

The Program to Calculate the Displacement Matrices

This program, run before the use of the preceding subroutine for simulating a disk shaped precipitate, calculates and stores on disk a matrix of values for displacements about a finite dislocation loop and integrates the equations given in Appendix I for the radial strain. Calculated here are not the actual displacements, u_i, but the normalized displacements, (u_i/b), so the preceding subroutine can freely alter the burgers vector magnitude.

The program has a nested DO-loop to select the (X,Z) values at which displacements will be calculated. In this loop is an adaptation of the equations given by Bullough et al. (1971) for a finite dislocation loop. Following this is another loop which integrates the equations for the radial strains. Rather than divide the loop (loop here refers to the inner line integral) into uniform segments, it was divided into arc lengths chosen such that the distance R from the point (X,Z) to the points along the segement varied less than some prescribed amount. The algorithm used to do this follows. The loop is the loci of points

$$r^2 = x^2 + y^2; \quad z = 0$$

The distance squared from the point (X,0,Z) to the near edge of the loop is

$$RE^2 = (X - r)^2 + Z^2$$

Starting with $\theta_1 = 0$, it is desired that the distance squared, R^2 (initially equal to RE^2), to points on the loop

not exceed aR^2 in going to the point defined by θ_2. If a is set to 1.02, then R^2 varies less than 2% on the arc from θ_1 to θ_2. The intersection of the sphere centered on (X,0,Z)

$$aR^2 = (x - X)^2 + (y - 0)^2 + (z - Z)^2$$

with the loop defines the point desired. This yields

$$x = (aR^2 - (r^2 + X^2 + Z^2))/2X$$

and

$$\theta_2 = \arccos(x/r)$$

After a number of iterations, the sphere defined by aR^2 will not intercept the loop, and a value of $x < -r$ results. At this point the program branches out of the integration DO-loop and completes integration to $\theta_2 = \pi$. Because of symmetry

$$u = \int_0^{2\pi} du(\theta) = 2\int_0^{\pi} du(\theta)$$

and using this the integration is completed.

```
CCC
CCC   THIS PROGRAM WAS USED TO COMPILE AND STORE ON DISK
CCC   A MATRIX OF DISPLACEMENTS ABOUT A FINITE DISLOCATION
CCC   LOOP AND ABOUT AN INFINITESIMALLY THIN HOOP (CYLANDER)
CCC   INDUCING RADIAL STRAINS.  THIS PROGRAM MUST BE RUN
CCC   BEFORE THE SIMULATION PROGRAM IF A DISK IS TO BE
CCC   SIMULATED.
CC
CCC
      DIMENSION UEDG1(30,20),UEDG3(30,20),ULP1(30,20),ULP3(3
      READ(5,1000)C11,C12,C44
      READ(5,1000)RAD
      READ(5,1000) ACONST
 1000 FORMAT(8F8.2)
CC   ACONST IS THE INCREASE IN DISTANCE SQUARED FROM THE
CC    NEAR END OF THE ARC TO THE FAR END (1.02 IS A
CC    REASONABLE VALUE TO USE);  ACON2 IS USED TO GET AN
CC    AVERAGE VALUE FOR THE DISTANCE SQUARED TO THE ARC.
      ACON2=0.5*(1+ACONST)/ACONST
      WRITE(6,3000) RAD,ACONST,C11,C12,C44
 3000 FORMAT(1X,5E20.5)
CC
CC   DEFINE NEEDED CONSTANTS
      PI=3.14159265 36
      RAD2=RAD**2
      ANU=C12/(2.0*(C12+C44))
      A=C44-C12
      B=-C44-C12
      CC=3*(C12+C44)
      BVAL=1/(8*PI*C11*C44)
      C1=(C11*(A+B)+2*C12*(B-C12))/2.0
      C2=RAD*(C11*A+2*C12*B)
      C3=(C11*(A-B)+2*C12*(B+C12))/4.0
      C41=(C11+C12)/2.0
      C42=2*C11*RAD2
      C51=(8*C11+C12)*RAD/3.0
      C52=C11*RAD**3
      C53=C12*RAD
      C61=(C11-C12)/4.0
      C62=0.5*C11*RAD2
      C7=RAD*(C12-C11)/3.0
      D1=(C11*B+C12*(A+B))
      D21=0.5*(C11+C12)
      D22=C11*RAD2
      D3=2*RAD*C11
      D4=0.25*(C11-C12)
      WRITE(6,3000)  ANU,BVAL,A,B,CC
      WRITE(6,3000)  C1,C2,C3
      WRITE(6,3000)  C41,C42,C51,C52,C53
      WRITE(6,3000)  C61,C62,C7
      WRITE(6,3000)  D1,D21,D22,D3,D4
CC
CC   SELECT POINTS (XO,ZO)  IN THE X-Z PLANE
      DO 11 IZ=1,20
      ZO=5.0*(IZ-1)
      DO 22 IX=1,30
      XO=5.0*(IX-1)
CC   INITIALIZE VARIABLES
      U1=0.0
      U3=0.0
      UL1=0.0
      UL3=0.0
CC   THE FOLLOWING ARE "OLD" VALUES
      THO=0.0
      SINO=0.0
      SIN2O=0.0
      SNCSO=0.0
CC
      X2=XO**2
      Z2=ZO**2
```

```
CC   RE2 IS DISTANCE SQUARED TO NEAR EDGE OF LOOP (THETA=0)
CC   RCONT2 IS NEEDED IN DO-LOOP BELOW
       RE2=X2+RAD2-2*RAD*XO+Z2
       RCONT2=RAD2+X2+Z2
       ARE2=RE2
CC
CC
CC   CALCULATE FINITE LOOP DISPLACEMENTS
CC    HARWELL ELLIPTIC SUBROUTINES ARE USED
       ROL=XO/RAD
       ZETA=ZO/RAD
       IF(XO.EQ.0.0)GO TO 91
       IF(XO.EQ.RAD.AND.ZO.EQ.0.0) GO TO 92
       AK=4.0*ROL/(ZETA**2+(1.0+ROL)**2)
       CALL FR01A(AK,3.0,RELC1,RELC2)
       P=4.0*ROL/(1.0+ROL)**2
       RAK=SQRT(AK)
       AI00=-RAK*ZETA*RELC1/(2.0*PI*SQRT(ROL))
       AKP=1.0-AK
       SINB=SQRT((P-AK)/(P*AKP))
       COSB=SQRT(1.0-SINB**2)
       CALL FR02A(AKP,SINB,COSB,E,F)
       CLAM=(RELC2*F+(E-F)*RELC1)/PI
       IF(ROL.LT.1.0)  AI00=AI00-CLAM+1
       IF(ROL.GE.1.0)AI00=AI00+CLAM
       AI10=RAK*AK*(1.0-ROL**2-ZETA**2)*RELC2/
     & ((1-AK)*8.0*PI*SQRT(ROL**3))
       AI10=AI10+RAK*RELC1/(2.0*PI*SQRT(RCL))
       AI01=2.0*((1.0-AK/2.0)*RELC1-RELC2)/
     &  (2I*RAK*SQRT(POL))
       AI11=RAK*ZETA*((1.0-AK/2.0)*RELC2/(1.0-AK)-
     &  RELC1)/(2.0*PI*SQRT(POL**3))
       UL1=-((1.0-2.0*ANU)*AI01-ZETA*AI11)/
     &  (4.0*(1.0-ANU))
       UL3=(2.0*(1.0-ANU)*AI00+ZETA*AI10)/
     &  (4.0*(1.0-ANU))
CC
CC
CC   FOR A MAX OF 200 ARC SEGMENTS, INTEGRATE THE LINE
CC    INTEGRAL FOR THE RADIAL STRAIN.
       DO 33 NTH=1,200
CC   INCREASE R**2
       ARE2=ARE2*ACONST
CC   FIND X OF POINT ON LOOP WHICH IS ARE**2 AWAY FROM
CC   (XC,ZO) AND USE THIS X TO DETERMINE THETA OF THE
CC   END OF THIS ARC.  SEE TEXT FOR ALGORITHM USED.
       XTH=-(ARE2-RCONT2)/(2.0*XO)
       IF(XTH.LE.(-RAD))  GO TO 99
       TH=ARCOS(XTH/RAD)
CC     RO2 IS AVERAGE VALUE OF R SQUARED FOR THIS ARC
       RO2=ACON2*ARE2
       RO3=RO2**1.5
       SN=SIN(TH)
       SN2=SIN(2.0*TH)
       SNCS=SN*(COS(TH))**2
       DSIN=SN-SINO
       DTH=TH-THO
       DSIN2=SN2-SIN2O
       DSNCS=SNCS-SNCSO
       THO=TH
       SINO=SN
       SIN2O=SN2
       SNCSO=SNCS
       CR2=CC/RO2
CCC
CCC    GET DISPLACEMENT FROM THIS ARC LENGTH
       T1=XO*DTH*C1-DSIN*C2+XO*DSIN2*C3
       T2=XO*(C41*X2+C12*Z2+C42)*DTH
       T3=-DSIN*(X2*C51+C52+C53*Z2)
       T4=DSIN2*XO*(C61*X2+C62)
       T5=DSNCS*X2*C7
       U1=U1+(T1+CR2*(T2+T3+T4+T5))/RO3
```

```
      TT1=DTH*D1
      TT2=DTH*(D21*X2+C12*Z2+D22)
      TT3=-DSIN*XO*D3
      TT4=DSIN2*X2*D4
      TTT=CR2*(TT2+TT3+TT4)
      DU=ZO*(TT1+TTT)/RO3
      U3=U3+DU
 1010  FORMAT(/,1X,5E20.6)
   33 CONTINUE
CC
CCC    FALLING OUT OF DO-LOOP INDICATES TOO MANY STEPS
CC        NEEDED TO INTEGRATE THE DISPLACEMENTS
      WRITE(6,1100)
 1100 FORMAT(1X,'ITERATION ERROR, INCOMPLETE INTEGRATION')
      GO TO 88
CC
CC   FOLLOWING LINES COMPLETE INTEGRATION TO FAR SIDE OF LOOP
   99 ARE2=ARE2/ACONST
      RO2=0.5*(ARE2+(XO+RAD)**2+Z2)
      RO3=SQRT(RO2)**3
      DTH=PI-THO
      DSIN=-SINO
      DSIN2=-SIN2O
      DSNCS=-SNCSO
      CR2=CC/RO2
      T1=XO*DTH*C1-DSIN*C2+XO*DSIN2*C3
      T2=XO*(C41*X2+C12*Z2+C42)*DTH
      T3=-DSIN*(X2*C51+C52+C53*Z2)
      T4=DSIN2*XO*(C61*X2+C62)
      T5=DSNCS*X2*C7
      U1=U1+(T1+CR2*(T2+T3+T4+T5))/RO3
      TT1=DTH*D1
      TT2=DTH*(D21*X2+C12*Z2+D22)
      TT3=-DSIN*XO*D3
      TT4=DSIN2*X2*D4
      U3=U3+ZO*(TT1+CR2*(TT2+TT3+TT4))/RO3
      GO TO 88
CC
CC    IF (XO,ZO) IS ON LOOP AXIS, USE SIMPLER FORMULAS
   91 RO2=RCONT2
      RO3=SQRT(RO2)**3
      CR2=CC/RO2
      U1=0.0
      U3=ZO*(PI*D1+CR2*PI*(D22+C12*Z2))/RO3
      FAC=SQRT(1.0/(1.0+ZETA**2))
      AI00=1.0-ZETA*FAC
      AI01=FAC**3
      UL3=(2.0*(1.0-ANU)*AI00+ZETA*AI01)/(4.0*(1.0-ANU))
      UL1=0.0
      GO TO 88
CC
CC    IF (XO,ZO) FALLS ON THE LOOP, SET DISPLACEMENTS TO 0
   92 U1=0.0
      U3=0.0
      UL1=0.0
      UL3=0.0
CC
CC LOAD THE DISPLACEMENT MATRICES
   88 UEDG1(IX,IZ)=2.0*BVAL*RAD*U1
      UEDG3(IX,IZ)=2.0*BVAL*RAD*U3
      ULP1(IX,IZ)=UL1
      ULP3(IX,IZ)=UL3
      WRITE(6,2000)ZO,XO,UEDG1(IX,IZ),UEDG3(IX,IZ),UL1,UL3
 2000 FORMAT(1X,7E15.6,/)
   22 CONTINUE
   11 CONTINUE
CC    WRITE THE DISPLACEMENT MATRICIES TO DISK
      WRITE(11) UEDG1,UEDG3,ULP1,ULP3
  101 STOP
      END
```

The Program for Calculation of Displacements About a Disk of Solute Atoms

This program is a modification of the program just listed. The radial strains have been replaced by the equations developed in Appendix I for a disk of solute atoms. These matrices are used by the disk simulation subroutine already discussed. For the GP zone simulation, the thickness of the disk is set to 1 Å, BE is set to -0.3 Å and BL is set to zero. For the solute on a loop simulation, the thickness of the disk is set to 1 Å, BE is set to -0.3 Å and BL is set to 2.02 Å.

```
C
CCC THIS PROGRAM WAS USED TO COMPILE AND STORE ON DISK A
CCC MATRIX OF DISPLACEMENTS ABOUT A FINITE LOOP AND
CCC ABOUT A DISK OF SOLUTE ATOMS.
CCC
      DIMENSION UEDG1(30,20),UEDG3(30,20),ULP1(30,20),ULP3(3
      READ(5,1000)C11,C12,C44
      READ(5,1000)RAD
 1000 FORMAT(8F8.2)
      WRITE(6,3000) RAD,C11,C12,C44
 3000 FORMAT(1X,5E20.5)
      PI=3.14159265 36
      RAD2=RAD**2
      ANU=C12/(2.0*(C12+C44))
C
CC  SELECT THE POINTS (XO,ZO)
      DO 11 IZ=1,20
      ZO=5.0*(IZ-1)
      DO 22 IX=1,30
      XO=5.0*(IX-1)
      UL1=0.0
      UL3=0.0
      X2=XO**2
      Z2=ZO**2
      ROL=XO/RAD
      ZETA=ZO/RAD
      IF(XO.EQ.0.0)GO TO 91
      IF(XO.EQ.RAD.AND.ZO.EQ.0.0) GO TO 92
C
CC DETEMINE HANKEL-LIPSCHITZ INTEGRALS
CC  USING HARWELL ELLIPTIC SUBROUTINES
      AK=4.0*ROL/(ZETA**2+(1.0+ROL)**2)
      CALL FB01A(AK,3.0,RELC1,RELC2)
      P=4.0*ROL/(1.0+ROL)**2
      RAK=SQRT(AK)
      AI00=-RAK*ZETA*RELC1/(2.0*PI*SQRT(ROL))
      AKP=1.0-AK
      SINB=SQRT((P-AK)/(P*AKP))
      COSB=SQRT(1.0-SINB**2)
      CALL FB02A(AKP,SINB,COSB,E,F)
      CLAM=(RELC2*F+(E-F)*RELC1)/PI
      IF(ROL.LT.1.0) AI00=AI00-CLAM+1
      IF(ROL.GE.1.0)AI00=AI00+CLAM
      AI10=RAK*AK*(1.0-ROL**2-ZETA**2)*RELC2/
     & ((1-AK)*8.0*PI*SQRT(ROL**3))
      AI10=AI10+RAK*RELC1/(2.0*PI*SQRT(ROL))
      AI01=2.0*((1.0-AK/2.0)*RELC1-RELC2)/
     &  (PI*RAK*SQRT(ROL))
      AI11=RAK*ZETA*((1.0-AK/2.0)*RELC2/(1.0-AK)-
     &  RELC1)/(2.0*PI*SQRT(ROL**3))
      UL1=-((1.0-2.0*ANU)*AI01-ZETA*AI11)/
     & (4.0*(1.0-ANU))
      UL3=(2.0*(1.0-ANU)*AI00+ZETA*AI10)/
     & (4.0*(1.0-ANU))
CCC  THE FOLLOWING ARE THE SOLUTE DISPLACEMENTS
      UGRAY1=0.5*AI01
      UGRAY3=0.5*AI00
      GO TO 88
C
CC IF (XO,ZO) IS ON THE LOOP AXIS, USE SIMPLER FORMULAS
   91 RO2=RCONT2
      RO3=SQRT(RO2)**3
      CR2=CC/RO2
      U1=0.0
      U3=ZO*(PI*D1+CR2*PI*(D22+C12*Z2))/RO3
      FAC=SQRT(1.0/(1.0+ZETA**2))
      AI00=1.0-ZETA*FAC
      AI10=FAC**3
      AI01=0.0
      UL3=(2.0*(1.0-ANU)*AI00+ZETA*AI10)/(4.0*(1.0-ANU))
      UL1=0.0
```

```
      UGRAY1=0.5*AI01
      UGRAY3=0.5*AI00
      GO TO 88
CC
CC   IF (XO,ZO) FALLS ON THE LOOP, SET DISPLACEMENTS TO ZERO.
   92 UGRAY1=0.0
      UGRAY3=0.0
      UL1=0.0
      UL3=0.0
CC
C   LOAD THE DISPLACEMENT MATRICES
   88 UEDG1(IX,IZ)=UGRAY1
      UEDG3(IX,IZ)=UGRAY3
      ULP1(IX,IZ)=UL1
      ULP3(IX,IZ)=UL3
      WRITE(6,2000)ZO,XO,UEDG1(IX,IZ),UEDG3(IX,IZ),UL1,UL3
 2000 FORMAT(1X,7E15.6,/)
   22 CONTINUE
   11 CONTINUE
CC   WRITE THE DISPLACEMENTS TO DISK
      WRITE(11) UEDG1,UEDG3,ULP1,ULP3
  101 STOP
      END
```

APPENDIX III
COMPUTER STEREO ANALYSIS

Micrographs obtained using two different beam directions can be used to reconstruct the three dimensional sample. Figure 54 illustrates in two dimensions the method to be used. The two micrographs are projections of the two dimensional sample onto the one dimensional image. Working backwards from the images, the sample is straightforwardly reconstructed.

The algorithm to do this for the three dimensional case is as follows. A point in the image is selected to be the origin. On this point is constructed a three dimensional coordinate system related to the crystal: the first axis is $\bar{g}$, the third is the beam $\bar{Z}$, and the second is $(\bar{g}\times\bar{Z})$, all normalized. Measuring the (x,y) value of a point in the image (i.e., a defect) in terms of this system, the image point (a projection) can be expressed as a three dimensional point in crystal coordinates

$$\bar{p} = x(\bar{g}) + y(\bar{g}\times\bar{Z})$$

The true point, $\bar{P}$, responsible for the projected point, $\bar{p}$, must exist on the line

$$\bar{l}_1 = \bar{p}_1 + t_1\bar{Z}_1$$

If corresponding data is obtained from another beam direction $\bar{Z}_2$, the true point $\bar{P}$ is the intersection of the

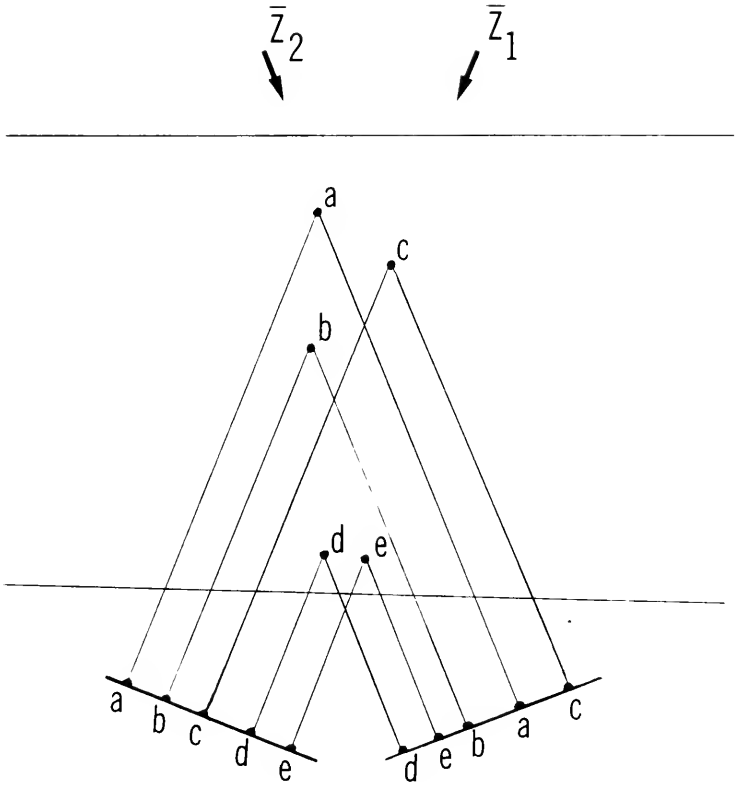

Fig. 54. Working backwards from the images, the three dimensional sample can be reconstructed.

two lines $\bar{l}_1$ and $\bar{l}_2$

$$\bar{p}_1 + t_1\bar{z}_1 = \bar{p}_2 + t_2\bar{z}_2$$

This represents three equations for the two unknowns t_1 and t_2. Due to errors, the lines $\bar{l}_1$ and $\bar{l}_2$ will usually be skew. Sought then is the point bisecting the line of closest approach between the two lines. Let t_1 and t_2 be such that they yield the end points of this segment. The line direction of this segment will obviously be

$$\bar{z}_3 = \bar{z}_1 \times \bar{z}_2$$

The segment is on the line

$$\bar{l}_3 = \bar{p}_3 + t_3\bar{z}_3$$

where $\bar{p}_3$ can be assigned as either end point of the segment

$$\bar{p}_3 = \bar{p}_1 + t_1\bar{z}_1 \quad \text{or} \quad \bar{p}_3 = \bar{p}_2 + t_2\bar{z}_2$$

The midpoint is the best estimate of the point's true position and is

$$\bar{P} = (\bar{p}_1 + t_1\bar{z}_1) + t_3\bar{z}_3 = (\bar{p}_2 + t_2\bar{z}_2) - t_3\bar{z}_3$$

This represents three equations for the three unknowns t_1, t_2 and t_3, which define $\bar{P}$. Rearrangement yields a convenient matrix formulation

$$(\bar{p}_1 - \bar{p}_2) = -t_1\bar{z}_1 + t_2\bar{z}_2 - t_3\bar{z}_3$$

$$(\overline{\Delta p}) = [B]\bar{t}$$

$$\bar{t} = [B]^{-1}(\overline{\Delta p})$$

where

$$\bar{t} = (t_1, t_2, t_3)$$

$$\overline{\Delta p} = (p_{1x} - p_{2x}, p_{1y} - p_{2y}, p_{1z} - p_{2z})$$

and

$$[B] = \begin{vmatrix} -z_{1x} & z_{2x} & -2z_{3x} \\ -z_{1y} & z_{2y} & -2z_{3y} \\ -z_{1z} & z_{2z} & -2z_{3z} \end{vmatrix}$$

[B] is associated with the pair of beam directions and the $(\overline{\Delta p})$ values for the ith defect in the micrographs are used to determine the three dimensional position of the points, $\overline{P}_i$.

The data was collected using a computer graphics device by which the computer can accurately determine where on an electronic pad a stylus is placed. For a particular micrograph, the beam direction and g-vector were entered at the computer keyboard. Then the first touch of the stylus defined the location of the origin (a specific defect or surface flaw identifiable in all micrographs). The next two data points defined the direction, head to tail, of the g-vector draw on the micrograph. Every point thereafter was the location of a defect image.

The most difficult task is properly pairing an image on one micrograph with its counterpart on another. The computer program proceeded as outlined in two dimensions in Fig. 55. The point D in micrograph 1 defines a column along the beam direction in which the defect must lie. The defect also lies within the two surfaces of the foil and using an overestimate of the foil thickness, the defect is restricted to a segment of the column. The end points of this segment map onto the second micrograph and the image of the defect lies between these two points. To allow for error in three dimensions, some width is added in the third dimension not

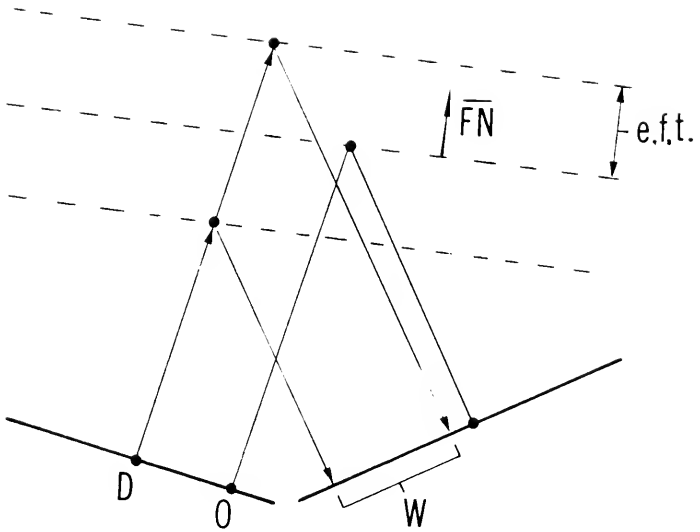

Fig. 55. Using an estimate of the foil thickness (e.f.t) and the foil normal ($\overline{FN}$), a window in which the defect image is expected (W) can be constructed on other micrographs.

shown in the figure to produce a rectangular window to be searched. In sorting the data the alogrithm use simply eliminated any points associated with any ambiguity (i.e., having no corresponding point in any of the other micrographs or having more than one possibility appear in the window). Doing this, the approximately 150 images per micrograph were culled to about 40 defects whose images could be unambiguously identified on all of the four micrographs used. The accuracy of the data was not sufficient to produce meaningful results.

The above briefly describes what has been done. The proper paths to follow in future work became more clear in this exploratory development. Most obvious among these is the need for more accurate data collection. First it must be decided (theoretically) what part of the image as a whole corresponds to the center of the defect. Secondly, this center must be measured with high mechanical precision. For micrographs of beam directions differing by 20^{o}, a total measurement error of 0.1 mm on a micrograph of 100,000 times magnification results in an error in the depth position corresponding to 27 nm. Since the present goal is to determine the depth to better than $0.1\ \xi_g \cong 7.0$ nm, much greater precision is clearly needed.

The greatest accuracy can be obtained by optically scanning the negative of the micrograph with a computerized detector to digitize the entire micrograph. With this data the computer can employ algorithms developed from TEM image theory to locate the center of the image. It also allows

the computer to pair images based on image appearance rather than simply image position.

Once accurate data is obtained, sorting through them to pair the corresponding images is the most difficult problem. This is also the chief advantage of using the computer since it allows great amounts of data to be handled on a more routine basis. Rather than simply eliminate data for which ambiguities arise, the search of other micrographs will often resolve the ambiguity. For example, if for a particular defect in micrograph 1, three images are found in the window mapped onto micrograph 2, it is unlikely that all three will appear in the window mapped onto micrograph 3 (given that the beam directions of all three are not coplanar). The greater the angle of tilt between micrographs, the greater is the parallax shifts. This results ultimately in greater accuracy but also produces more ambiguities. The program should start by pairing images on micrographs involving small tilts, going to greater tilts as ambiguities are resolved. Any sorting algorithm must handle the possibility that a defect may be out of the field of view in some micrographs. More bothersome than this is the possibility that, for one of several reasons, the defect may be effectively invisible in some micrographs.

After an initial sorting of the data produces a number of defects for which ambiguities do not exist, these can be used to detect and correct systematic errors such as slight changes in magnification and small errors in the alignment

of the g-vector drawn on the micrograph. The corrected data can be use to re-evaluate the defect positions. Having precise values for the positions of the unambiguously sorted defects, the computer can remove their projected positions, $\bar{p}_i$, from the lists in memory representing the micrographs. These culled lists, being less cluttered and corrected of systematic errors, can be resorted and many of the previously existing ambiguities will have been removed. The culling and resorting is iterated until no further ambiguities are eliminated.

Some defects will be identified in micrographs for which the tilt angles involved are large. Their positions will be determined with the greatest accuracy and confidence. On the other hand, some defects (such as those near the edge of the area examined) will be identified in fewer micrographs and/or in micrographs between which only small tilts exist. Their positions are less accurately known. The computer should keep separate estimates of the error of each defect. For many applications the great number of statistics this method can provide will offset any lack of accuracy.

BIBLIOGRAPHY

Ashby, M.F., and Brown, L.M., Phil. Mag., 8, 1083 (1963a).

Ashby, M.F., and Brown, L.M., Phil. Mag., 8, 1649 (1963b).

Bell, W.L., and Thomas, G., Phil. Mag., 13, 395 (1966).

Bethe, H.A., Ann. d. Physik, 87, 55 (1928).

Bocquet, J.C., and Martin, G., J. Nucl. Mater., 83, 186 (1979).

Bollmann, W., Phys. Rev., 103, 1588 (1956).

Borries, B. von, and Ruska, E., Naturwiss., 28, 366 (1940).

Bullough, R., Maher, D.M., and Perrin, R.C, Phys. Stat. Sol., 43, 689 (1971).

Bullough, R., and Newman, R.C., Phil. Mag., 5, 921 (1960).

Bullough, R. and Perrin, R.C., Radiation Induced Voids in Metals, CONF-710601 (1972).

Bullough, R., Stanley, J.T., and Williams, J.M., Metal Sci. J., 2, 93 (1968).

Byrd, P.F., and Friedman, M.D., Handbook of Elliptic Integrals for Engineers and Physicists, Lange, Maxwell, and Springer, Ltd., New York (1954).

Carpenter, R.W., and Ogle, J.C., Fundamental Aspects of Radiation Damage in Metals, Proc. Int. Conf., Gatlinburg, TN., 1203, CONF-751006-P2 (1975).

Carpenter, R.W., and Yoo, M.H., Met. Trans. (A), 9a, 1739 (1978).

Cauvin, R., and Martin, G., J. Nucl. Mat., 83, 67 (1979).

Cawthorne, C. and Fulton, E.J., Nature, 216, 575 (1967).

Coghlan, W.A., and Yoo, M.H., Trans. Am. Nucl. Soc., 27, 332 (1977).

Cooper, W.D., Simulation of Transmission Electron Micrographs for Small Dislocation Loops, Ph.D. Dissertation, University of Florida (1977).

Degischer, M.P., Phil. Mag., 26, 1137 (1972).

DeWit, R., Solid State Physics, 10, Academic Press, New York, 249 (1960).

Diepers, H., Phys. Stat. Sol., 24, 623 (1967).

Diepers, H., and Diehl, J., Phys. Stat. Sol., 16, K109 (1966).

Eason, G., Noble, B., and Sneddon, I.N., Phil. Trans. Soc. Lond. A, 247, 529 (1955).

Edington, J.W., Practical Electron Microscopy in Materials Science, N.V. Philips' Gloeilanpenfabrieken, Eindhoven (1975).

Edmondson, B., and Williamson, G.K., Phil. Mag., 9, 277 (1964).

English, C.A., Eyre, B.L., and Holmes, S.M., J. Phys. F: Metal Phys., 10, 1065 (1980).

Eshelby, J.D., Proc. Roy. Soc. A, 252, 561 (1959).

Essman, U., and Wilkens, M., Phys. Stat. Sol., 4, K53 (1964).

Eyre, B.L., Maher, D.M., and Perrin, R.C., J. Phys. F: Metal Phys., 7, 1359 (1977a).

Eyre, B.L., Maher, D.M., and Perrin, R.C., J. Phys. F: Metal Phys., 7, 1371 (1977b).

Farrell, K., and Houston, J.T., J. Nucl. Mater., 83, 57 (1979).

Farrell, K., Stiegler, J.O., and Gehlbach, R.E., Metallography, 3, 275 (1970).

Gray, A., Phil. Mag., 38, 201 (1919).

Grupens, W.B., and Sines, G., J. Appl. Phys., 35, 3001 (1964).

Grupens, W.B., and Sines, G., Acta Met., 13, 527 (1965).

Guinier, A., Nature, 142, 569 (1938).

Head, A.K., Australian J. Phys., 20, 557 (1967).

Head, A.K., Humble, P., Clarebrough, L.M., Morton, A.J., and Forwood, C.T., Computed Electron Micrographs and Defect Identification, North-Holland Publishing Comp., Amsterdam (1973).

Headley, T.J., Repeated Nucleation of Precipitates on Dislocations in Aluminum-Copper, Ph.D. Dissertation, University of Florida (1974).

Heidenreich, R., Fundamentals of Transmission Electron Microscopy, Wiley and Sons, New York (1964).

Hirsch, P.B., Horne, R.W., and Whelan, M.J., Phil. Mag., 1, 677 (1956).

Hirsch, P.B., Howie, A., Nicholson, R.B., Pashley, D.W., and Whelan, M.J., Electron Microscopy of Thin Crystals, Robert E. Krieger Publ. Comp., Huntington, N.Y. (1977).

Hirsch, P.B., Howie, A., and Whelan, M.J., Phil. Trans. A, 252, 499 (1960).

Hirsch, P.B., Silcox, J., Smallmann, R.E., and Westmacott, K.H., Phil. Mag., 3, 897 (1958).

Holmes, S.M., Eyre, B.L., English, C.A., and Perrin, R.C., J. Phys. f: Metal Phys., 9, 2307 (1979).

Howie, A., and Basinski, Z.S., Phil. Mag., 17, 1039 (1968).

Howie, A. and Whelan, M.J., Proc. Roy. Soc. A, 263, 216 (1961).

Hren, J.J., Goldstein, J.I., and Joy, D.C., Introduction to Analytical Electron Microscopy, Plenum Press, New York (1979).

Huebotter, P.R., and Bump, T.R., Radiation Induced Voids in Metals, CONF-710601 USAEC, 84 (1972).

Humble, P., Australian J. Phys., 21, 325 (1968).

Johnson, R.A., and Lam, N.Q., Phys. Rev. B, 13, 4364 (1976).

Katerbau, K-H., Phys. Stat. Sol. (a), 38, 463 (1976).

Katerbau, K-H., Phil. Mag. A, 43, 409 (1981).

Katz, L.E., Herman, H., and Damask, A.C., Acta Met., 16, 939 (1968).

Kestenbach, H-J., Quantitative Interpretation of Dislocation Contrast in Electron Microscopy, Master's Thesis, University of Florida (1971).

Krakow, W., Proc. 38th EMSA Meeting, Reno, Nevada, 178 (1980).

Maher, D.M., and Eyre, B.L., Phil. Mag., 17, 1 (1968).

Maher, D.M., and Eyre, B.L., Phil. Mag., 23, 409 (1971).

Mansur, L.K., Nuclear Tech., 40, 5 (1978).

Mansur, L.K., J. Nucl. Mater., 83, 109 (1979).

Mansur, L.K., and Wolfer, W.G., J. Nucl. Mater., 69&70, 825 (1978).

Martin, G., Phil. Mag., 38, 131 (1978).

Marton, L., Ann. Bull. Soc. Roy. Sci. Med. Nat. Bruxelles, 92, 106 (1934).

Marton, L., and Schiff, L.J., J. Appl. Phys., 12, 759 (1941).

Maydet, S.I., and Russell, K.C., J. Nucl. Mater., 64, 101 (1977).

Mazey, D.J., Barnes, R.S., and Howie, A., Phil. Mag., 7, 1861 (1962).

McIntyre, K.G., and Brown, L.M., J. Phys. Radium, 27, C3 (1966).

Nicholson, R.B., and Nutting, J., Phil. Mag., 3, 531 (1958).

Nicholson, R.B., Thomas, G., and Nutting, J., J. Inst. Met., 87, 429 (1958-59).

Ohr, S.M., Phil. Mag., 26, 1307 (1972).

Ohr, S.M., Phys. Stat. Sol. (a), 38, 553 (1976).

Ohr, S.M., Phys. Stat. Sol. (a), 56, 527 (1979).

Philips, V.A., Acta Met., 21, 219 (1973).

Philips, V.A., Acta Met., 23, 751 (1975).

Phillips, H.W.L., J. Inst. Met., 82, 9 (1953-54).

Preston, G.D., Nature, 142, 570 (1938).

Rühle, M., Phys. Stat. Sol., 19, 263 (1967).

Rühle, M., Wilkens, M., and Essmann, U., Phys. Stat. Sol., 11, 819 (1965).

Saldin, D.K., Stathopoulos, A.Y., and Whelan, M.J., Electron Diffraction 1927-1977, Inst. Phys. Conf. Ser. No. 41, 350 (1977).

Sass, S.L., Mura, T., and Cohen, J.B., Phil. Mag., 16, 749 (1972).

Silcox, J.M., and Heal, T.J., Acta Cryst., 9, 680 (1956).

Silcox, J.M., Heal, T.J., and Hardy, H.K., J. Inst. Met., 82 239 (1953-54).

Silcox, J.M., and Hirsch, P.B., Phil. Mag., 4, 1357 (1959).

Sines, G., and Kikuchi, R., Acta Met., 6, 500 (1958).

Sklad, P.S., and Mitchell, T.E., Acta Met., 23, 1287 (1975).

Sykes, L.J., Cooper, W.D., and Hren, J.J., Catalog of Computer Simulated TEM Images of Small FCC and BCC Dislocation Loops, ORNL/TM-7619 (1981).

Thölen, A.R., Phil. Mag., 22, 175 (1970).

Thomas, G., and Whelan, M.J., Phil. Mag., 6, 1103 (1961).

Weatherly, G.C., and Nicholson, R.B., Phil. Mag., 17, 801 (1968).

Weaver, L., Hudson, B., and Nutting, J., Met. Sci., 12, 257 (1978).

Whelan, M.J., and Hirsch, P.B., Phil. Mag., 2, 1121 (1957).

Wilkens, M., Vacancies and Interstitials in Metals, North-Holland Publ. Comp., Amsterdam, 485 (1970).

Wilkens, M., and Kirchner, H.O.K., Phil. Mag. A, 43, 139 (1981).

Wilkens, M., and Rühle, M., Phys. Stat. Sol., 49, 749 (1972).

Willis, J.R., and Bullough, R., J. Nucl. Mater., 32, 76 (1969).

Wolfer, W.G., and Ashkin, M., J. Appl. Phys., 42, 547 (1975).

Wolfer, W.G., and Mansur, L.K., Phys. Stat. Sol. (a), 37, 211 (1976).

Yoffe, E., Phil. Mag., 21, 833 (1970).

Yoffe, E., Phil. Mag., 25, 935 (1972).

BIOGRAPHICAL SKETCH

Lawrence Joseph Sykes was born in Greenville, South Carolina on June 6, 1955. He lived most of his childhood in Florida and entered the University of Florida as an undergraduate in 1973. He received his Bachelor of Science in Engineering degree in December of 1976. He continued his education in graduate school at the University of Florida. He completed his work for the degree of Doctor of Philosophy in the summer of 1981.

Lawrence Joseph Sykes is unmarried and living in Houston, Texas. He is a member of the American Institute of Mining, Metallurgical and Petroleum Engineers, Alpha Sigma Mu, Keramos and the American Electron Microscopy Society.

I certify that I have read this study and that in my opinion it conforms to acceptable standards of scholarly presentation and is fully adequate, in scope and quality, as a dissertation for the degree of Doctor of Philosophy.

John J. Hren, Chairman
Professor of Materials Science
and Engineering

I certify that I have read this study and that in my opinion it conforms to acceptable standards of scholarly presentation and is fully adequate, in scope and quality, as a dissertation for the degree of Doctor of Philosophy.

Robert T. DeHoff
Professor of Materials Science
and Engineering

I certify that I have read this study and that in my opinion it conforms to acceptable standards of scholarly presentation and is fully adequate, in scope and quality, as a dissertation for the degree of Doctor of Philosophy.

Robert E. Reed-Hill
Professor of Materials Science
and Engineering

I certify that I have read this study and that in my opinion it conforms to acceptable standards of scholarly presentation and is fully adequate, in scope and quality, as a dissertation for the degree of Doctor of Philosophy.

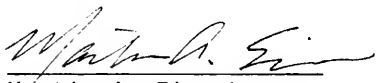

Martin A. Eisenberg
Professor of Engineering Sciences

I certify that I have read this study and that in my opinion it conforms to acceptable standards of scholarly presentation and is fully adequate, in scope and quality, as a dissertation for the degree of Doctor of Philosophy.

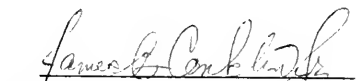

James B. Conklin
Director C.I.R.C.A.

This dissertation was submitted to the Graduate Faculty of the College of Engineering and to the Graduate Council, and was accepted as partial fulfillment of the requirements for the degree of Doctor of Philosophy.

December, 1981

Herbert A. Lewis
Dean, College of Engineering

Dean, Graduate School